Czech Technical University in Prague
Faculty of Nuclear Sciences and Physical
Engineering

**Department of Physics**
**Nuclear and Particle Physics**

# Reconstruction of lambda baryon at the mini-CBM experiment

DIPLOMA THESIS

| | |
|---|---|
| Author: | Bc. Radim Dvořák |
| Supervisor: | RNDr. Petr Chaloupka, Ph.D. |
| Year: | 2023 |

České vysoké učení technické v Praze
Fakulta jaderná a fyzikálně inženýrská

**Katedra fyziky**
**Jaderná a částicová fyzika**



# Rekonstrukce baryonu lambda na experimentu mini-CBM

DIPLOMOVÁ PRÁCE

| | |
|---|---|
| Vypracoval: | Bc. Radim Dvořák |
| Vedoucí práce: | RNDr. Petr Chaloupka, Ph.D. |
| Rok: | 2023 |

FAKULTA JADERNÁ A FYZIKÁLNĚ INŽENÝRSKÁ

KATEDRA FYZIKY

# ZADÁNÍ DIPLOMOVÉ PRÁCE

**Akademický rok:** 2022/2023

| | |
|---|---|
| *Student:* | Bc. Radim Dvořák |
| *Studijní program:* | Jaderná a částicová fyzika |
| *Název práce:*<br>*(česky)* | Rekonstrukce baryonu lambda na experimentu mini-CBM |
| *Název práce:*<br>*(anglicky)* | Reconstruction of lambda baryon at the mini-CBM experiment |
| *Jazyk práce:* | Angličtina |

*Pokyny pro vypracování:*

1) Ultra-relativistické srážky těžkých jader

2) Produkce podivnosti v jaderných srážkách

3) Fyzikální cíle a design experimentu CBM na urychlovači FAIR

    I.   Předpovědi produkce podivných částic na experimetnu CBM

4) Experiment mini-CBM

Praktická část:

5) Simulace rekonstrukce lambda baryonu

    I.   Simulace odezvy detektoru pro primární lambda baryony v geometrii roku 2022

    II.  Získání účinnosti rekonstrukce lambda baryonu

    III. Oprava spekter na účinnost detektoru

    IV. Srovnání s reálnými daty

6) Shrnutí a závěr

*Doporučená literatura:*

[1] T. Ablyazimov et al., Challenges in QCD matter physics —The scientific programme of the Compressed Baryonic Matter experiment at FAIR,Eur. Phys. J. A (2017) 53: 60

[2] B. Friman et al, The CBM Physics Book, ISBN: 978-3-642-13293-3

[3] P. Senger et al., CBM Progress Report 2020, ISBN 978-3-9815227-9-2

[4] CBM collaboration, mCBM@SIS18A CBM full system test-setupfor high-rate nucleus-nucleus collisionsat GSI / FAIR, CBM SVN 7729, https://fair-center.de/fileadmin/fair/experiments/CBM/documents/mcbm-proposal2GPAC-WebVersion0619-SVN7729.pdf

*Jméno a pracoviště vedoucího diplomové práce:*

RNDr. Petr Chaloupka, Ph.D.

Katedra fyziky, Fakulta jaderná a fyzikálně inženýrská ČVUT v Praze

*Datum zadání diplomové práce:*      20.10.2022

*Termín odevzdání diplomové práce:*      03.05.2023

*Doba platnosti zadání je dva roky od data zadání.*

.......................................
*garant studijního programu*
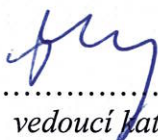
.......................................
*vedoucí katedry*

.......................................
*děkan*

*V Praze dne*    20.10.2022

**ČESKÉ VYSOKÉ UČENÍ TECHNICKÉ V PRAZE**

**Fakulta jaderná a fyzikálně inženýrská**

Břehová 7
115 19 Praha 1

# P R O H L Á Š E N Í

Já, níže podepsaný

*Jméno a příjmení studenta:* Radim Dvořák

*Osobní číslo:* 486634

*Název studijního programu (oboru):* Jaderná a částicová fyzika

prohlašuji, že jsem diplomovou práci s názvem:

**Rekonstrukce baryonu lambda na experimentu mini-CBM**

vypracoval samostatně a uvedl veškeré použité informační zdroje v souladu s Metodickým pokynem o dodržování etických principů při přípravě vysokoškolských závěrečných prací.

V Praze dne 2.5.2023

..................................................................

podpis

**Acknowledgement**

*Abstrakt:*
V letech 2017/18 byl na zařízení SIS18 GSI/FAIR zkonstruován detektor mCBM - demostrační prekurzor experimetnu CBM. mCBM nabírá od roku 2019 data v rámci programu FAIR fáze 0. Hlavním cílem mCBM je zprovoznit a optimalizovat systém sběru dat CBM včetně přenosu dat do vysoce výkonné počítačové farmy. Cílem je také test algoritmů pro online rekonstrukci tracků a eventů, výběr eventů a online analýzy dat, jakož i řídicích softwarových balíčků. mCBM se skládá z prototypů a předsériových komponent všech subsystémů detektoru CBM a jejich vyčítacích systémů. Rekonstrukce lambda hyperonů bude použita jako referenční pozorování, které prověří výkonnost hardwaru a softwaru CBM. Pomocí simulací byly testovány různé konfigurace detektorů, aby byla určena nejvhodnější geometrie pro rekonstrukci lambda hyperonů pomocí sestavy mCBM v reálných datech.

*Klíčová slova:*        FAIR, CBM, mCBM, lambda hyperon, TMVA

*Abstract:*
mCBM is a precursor and demonstrator experiment which was constructed during 2017/18 at the SIS18 facility of GSI/FAIR, and has been taking data within the FAIR phase-0 program since 2019. The primary aim of the mCBM is to commission and optimize the CBM triggerless-streaming data acquisition system including data transport to a high-performance computer farm, the online track and event reconstruction and event selection algorithms, and the online data analysis as well as the software-control packages. The mCBM comprises of prototypes and pre-series components of all CBM detector subsystems and their read-out systems. The reconstruction of lambda hyperons will be used as a benchmark observable probing the performance of the CBM hardware and software. Using simulations, various detector configurations have been tested identifying the most suitable geometry for the reconstruction of the lambda hyperons with the mCBM setup in real data.

*Key words:*         FAIR, CBM, mCBM, lambda hyperon, TMVA

# Contents

# Introduction

The CBM experiment is expected to be one of the most important near-future experiments for research of nuclear matter under extreme conditions. In comparison with the current experiments at LHC and RHIC, the CBM will not be focused on the highest energies, but it will cover the area of the middle energies and higher net baryon densities. The uniqueness of the CMB will be in its ability to collect data at high collision rates which will make CBM sensitive even to even very rare probes. This will enable us to study properties of the nuclear matter and its phase transition with unprecedented precision. Before the CBM experiment will function a testing mini-CBM (mCBM) experiment will be conducted. The purpose of the mCBM is to test detectors, optimize the triggerless-streaming data acquisition, online track and event reconstruction for CBM in order to reduce commissioning time after CBM is built. Succesful reconstruction of $\Lambda$ hyperons is one of the benchmarks verifying that all subsystems of the mCBM are operational including software. Before the next data campaign, many different geometries of the mCBM will be studied and based on the simulations the most suitable geometry will be chosen. The main part of this thesis lies in the simulations of the $\Lambda$ reconstruction efficiencies for the different mCBM geometries, improvement of the $\Lambda$ finding algorithm and using machine learning technique to further enhance the statistical significance of the signal.

The presented thesis is divided into five parts. In the first chapter a brief introduction into physics of heavy-ion collisions is given. The main variables and properties of QCD are described. Next part focuses on the properties of the quark-gluon plasma (QGP). The last part of the chapter consists of multiple observables used for study of the strongly interacting matter produced in collisions of heavy ions.

The second chapter is dedicated to the production of strangeness in heavy-ion collisions. Measurements of ratios of the strange and non-strange particles are discussed as well as an enhancement of the strange particles as a signature of the creations of the QGP in heavy-ion collisions. Importance of strangeness for nuclear equation of state under extreme conditions is also mentioned.

The third chapter is focused on the description of the CBM experiment at FAIR facility. First, the history and current status of the FAIR/GSI are described and then the main focus is moved to the CBM experiment. Individual subsystems and their functionality are described. Next, the current experiment mCBM is described and different possible considered geometries are shown.

The fourth chapter is dedicated to my own work on the $\Lambda$ simulations. At the beginning properties of $\Lambda$ baryon and toy model for $\Lambda$ simulations are introduced. Further real simulation setup is described. One of the most important parts of the

simulations is tracking which is only based on topological cuts and time-of-flight velocity measurements. The key part of this chapter are results for different collision systems studied for different mCBM geometries. The most challenging collision system is Au+Au at energies 1.24 AGeV due to the size of the background and the lowest energy of collision which is under the $\Lambda$ threshold production. Also machine-learning technique was used for the $\Lambda$ reconstruction. The last part is focused on the simulations in real geometries in which data was taken in May and June 2022.

The last chapter is dedicated to analysis of the real data taken in May 2022 of Ni+Ni collisions at 1.93 AGeV and its comparison with simulations. Initially, the time calibrations are discussed as well as the detector performance and alignment. Next part is focused on the $\Lambda$ reconstruction and different approaches how to improve separation of the signal from data. Also comparison of several $\Lambda$ properties obtained from the simulations is shown.

In the appendix proceeding from FAIRness 2022 conference focused on the simulations of $\Lambda$ reconstruction in several different geometries are included.

# Chapter 1

# Relativistic collisions of heavy ions

## 1.1 Standard model

The Standard Model [1–3] is a theory describing interactions of the most elementary particles. It describes three known interactions - strong, weak and electromagnetic (gravity is not included). Figure 1.1 shows particles existing within Standard Model. Part of the Standard Model describing the strong interaction contains three generations of the quarks, up ($u$) and down ($d$) quarks are the first one (almost all observable matter is composed only of these two quarks), the second generation is charm ($c$) and strange ($s$), third generation contains top($t$) and bottom ($b$). Interactions among them are mediated by gluons. Gluons are particles with a spin 1 (thus they are bosons) and they carry a color charge which is used for the description of the strong interaction. Three colors are possible - Red, Green and Blue and each gluon carries one color and one anti-color based on the group SU(3) gauge symmetry. The mathematical theory describing an interaction between quarks and gluons is called QCD (Quantum chromodynamics). The strong force is indeed strongest when compared with the electromagnetic and weak one. If strong force had a magnitude 1 then electromagnetic would have $1/137$ and weak $10^{-6}$. The actual force acting between two color charges is not constant and depends on the distance (transferred momentum). Due to the fact that the gluon carry color charge, and therefore can interact among themselves, its strength is increasing with distance which is quite opposite to the behaviour of the electromagnetic force.

This behaviour can effectively be described by a potential which on large distances behaves as a string. Therefore for quarks it is energetically most favourable to be at a short distance. When quarks are moved apart the potential energy of strong force increases and when high enough a new quark-antiquark pair is created. For this reason, the particles with a bare color charge can not be detected which means gluons and also quarks are not detectable. Only color-neutral particles can be detected which means that quarks have to gather into mesons (quark-antiquark pairs) or baryons (three quarks) and these particles can be detected. This effect is called confinement. It is also the reason why hadronisation occurs at the end of the interaction of the heavy ions.

One way the quark confinement can be described is using the so called MIT Bag model [4]. In this model, hadrons are finite bags with massless quarks inside submerged in the QCD vacuum which creates pressure on the bag. Quarks are confined when there is a balance between the kinetic energy of quarks and the vacuum pressure $B$. Based on this model one can assume the critical temperature of deconfinement as $T \approx 144 \, \text{MeV}$. This suggests a phase transition could exist.
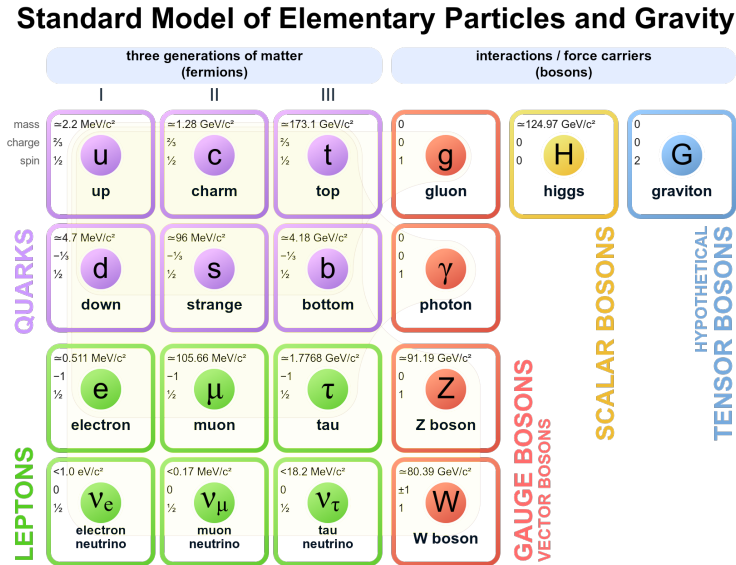


Figure 1.1: Sketch of the standard model particles and interactions. From [5].

## 1.2 Quark gluon plasma

### 1.2.1 Motivation

Motivation for the search for quark-gluon plasma can be somewhat guided by our experiences with other systems for example with water. Water can be in different phases depending on its temperature and pressure. For example under normal pressure when the temperature is increased up to 100°C we can observe a first-order phase transition from water to steam. You can see phase diagram of the water in Figure 1.2. Furthermore, when the temperature and pressure increase we can come to the critical point where the line of the first-order phase transition ends and crossover (second-order) phase transition starts. The difference between these two-phase transitions is following. When the first order transition occurs between two phases, it is need to add some latent heat and the system can stay in a mixed phase (both phases can coexist at one temperature). The second-order transition is smooth and there is no latent heat needed.

With water in our conditions, we do not have experience with this phenomenon however we have practical experience with ferromagnet. When the temperature of the ferromagnet is increased over Curie temperature magnetisation will disappear
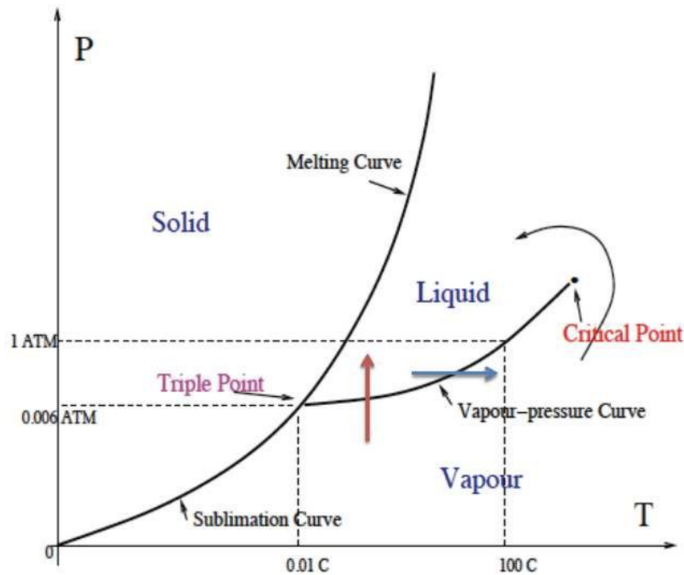
Figure 1.2: Phase diagram of water. From [6].

and the phase transition is smooth (second-order) - this example can be described by so called Ising model. In a ferromagnet, spins can be aligned by application of an external magnetic field producing non-zero magnetization of the material. In the total Hamiltonian of the system, two terms are then present: the first is based on the spin-spin interactions and the second is due to the external magnetic field. When we deal with this system using tools of statistical physics we can define the temperature of the system. When the temperature of the system is high (in ferromagnet higher than Currie temperature) then the random motion of the spins wins and there will be no magnetization. The system is fully symmetric. However, when the temperature is decreasing external field starts playing a more important role over the random motion. The symmetry is then broken due to the alignment of the spins. This is called spontaneous symmetry breaking. If the temperature of the system decreases even more almost all spins are aligned and if the external field is turned off the material will be magnetised.

Water and ferromagnet examples are results of the electromagnetic force. Therefore there is a natural question: Can the strong force produce similar structures?

## 1.2.2 Phase diagram of QCD

Figure 1.3 shows a simplified sketch of the phase diagram of strongly interacting matter. The difference between this diagram and that of water is the use of the net baryon density instead of pressure (the net baryon density can be measured and calculated more easily, but the message is very similar). The net baryon density is defined as the number of baryons minus the number of antibaryons per volume. As can be seen, at the LHC the net baryon density is very small (around zero). One of the advantages of studying matter at low net baryon density is that lattice QCD (lQCD) can predict evolution in this region. The prediction of lattice QCD for the

17
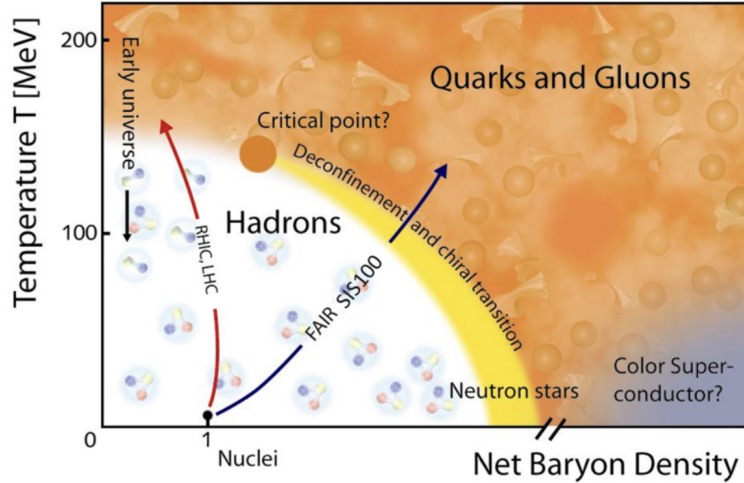
Figure 1.3: Phase diagram of strong interacting matter. From [7].

phase transition in this region is a crossover which is in agreement with the measurements. By moving to lower collision energies, we can reach higher net baryon densities. Many theories predict a first-order phase transition at higher net baryon densities. This implies, in effect, that there should be a critical point of QCD somewhere in between. The theoretical predictions for the critical points from different models are shown in Figure 1.4. As can be seen, the predictions of the models differ significantly which means that the experimental inputs are crucial for understanding QCD. The large differences of the predicted location critical point is due to the inability to calculate the QCD partition function at high net baryon densities and to find its singularities corresponding to the first-order phase transition. This can only be solved for low densities - in lattice QCD. There are several approaches to how to extend the lQCD predictions to slightly higher densities [8].

## 1.3 Relativistic heavy ion collisions

Collisions of heavy ion collisions [1, 2] (HIC) are the most direct way how to experimentally study strongly interacting matter under extreme conditions in the laboratory. Two different arrangements are possible, the first is the collider type experiment - in which two ions are accelerated and interact in the middle of the detector. Such experiments are carried out, for example, at CERN and RHIC. The second are fixed-target experiments, in which the target nuclei are at rest and only the projectile nuclei are accelerated. The future CBM will be a fixed target experiment. Fixed target experiments are more common for lower energies (down to tens of GeV) and have the advantage of being able to measure at high rapidities, high collision rates and offer easier reconstruction of short living particles. On the other hand their disadvantage is higher density of tracks in detectors and naturally the fact that only part of the energy of the projectile is available for particle production due to the conservation of momentum of the center of mass of the system.
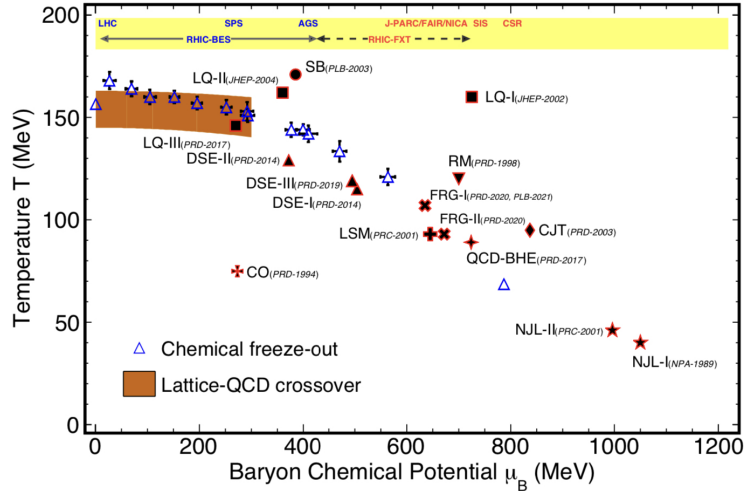
Figure 1.4: Predictions for critical point of QCD (red black symbols), measured freeze-out points measured experimentally and the brown band represents lattice QCD crossover prediction. From [9].

One of the main variables characterising the collision of the heavy-ion is the center of mass energy $s = (p_1 + p_2)^2$ where $p_1$ and $p_2$ are four-momenta of incoming particles, $s$ is one of the Mandelstam variables and it is Lorentz invariant. It can be easily shown that for the fixed-target experiment:

$$s = m_1^2 c^4 + m_2^2 c^4 + 2E_1 m_2 c^2, \tag{1.1}$$

where $E_1$ is the total energy of the first incoming projectile and $m_1$ and $m_2$ are the projectile and target masses respectively. This variable $E_1$ is commonly given in AGeV which means energy of the projectile per one nucleon. From the energy $\sqrt{s}$ final states hadrons will be produced. Commonly variable $\sqrt{s_{NN}} = \sqrt{s}/A$ is used denoting center of mass energy per one NN collision.

Another important variable for describing collision is centrality. Geometrically, it is defined as the transverse distance between the centres of the interacting ions (impact parameter $b$). The centrality of a collision cannot be measured directly, but can be determined using multiplicity or a special detector that measures nuclear fragments. The centrality is then measured as quantiles of the total inelastic cross-section, collisions with centrality $0 - 5\%$ being the most central and with increasing percentage the centrality decreases to the most peripheral collisions with centrality approaching $100\%$. Figure 1.5 shows a sketch of a collision at the centre of mass. Initially, the ions are Lorentz contracted due to their high velocity (up to a gamma factor of thousands at LHC energies, at FAIR energies the gamma factor is in units). When a collision occurs, only a fraction of the ions are involved - they are called the "participants" and the rest are "spectators".

In general, three phases of HIC can be distinguished. The first one is the initial nucleon-nucleus collisions (pre-equilibrium phase). In the interaction region nucleons of the incoming nuclei collide and new particles can be produced. The strongly
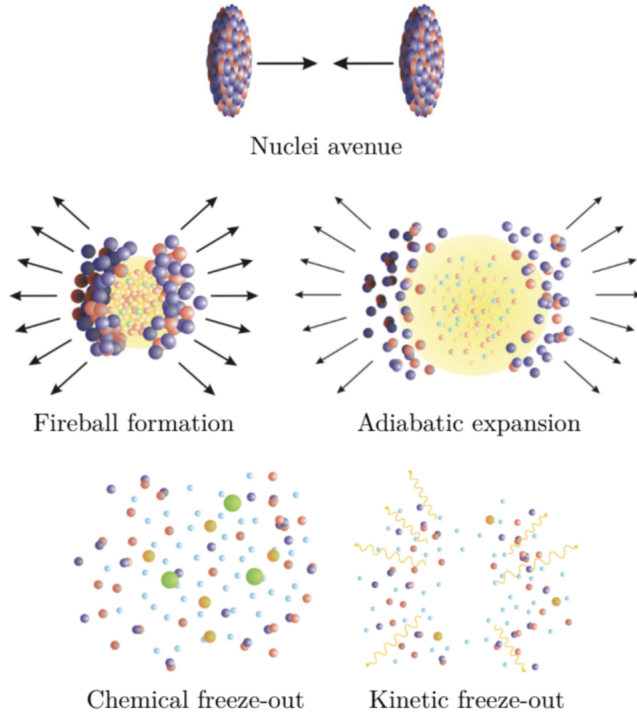
Figure 1.5: Sketch of the relativistic heavy ions collision. From [10].

interacting system then rapidly moves towards thermal equilibrium. The second one is the high (energy) density phase (fireball formation). At sufficiently high temperature, a transition to a quark-gluon plasma can occur (this is expected especially at the collision energies of the LHC and RHIC). At this stage the system evolves and in doing so, it expands and cools. After some time, the temperature is not high enough to sustain the plasma, the phase transition between QGP and hadronic phase occurs. Nevertheless, new particles (for example strange particles) can be still created in inelastic collisions. When the temperature of chemical freeze out is reached the production of new particles through inelastic collisions stops and at this point measured particle ratios are fixed. After further cooling kinetic freeze-out occurs. This is when particles stop interacting even elastically and free stream into the detector. Figure 1.6 shows the evolution of heavy-ion collision as a function of time $t$ and distance $z$ with (right) and without (left) QGP formation.

From the experimental point of view we can "tune" how the system evolves only by setting the collisions energy and making selections such as above described centrality classes. In the Figure 1.7 you can see time evolution of the collision in variables $T$ and $\mu_B$. Collisions with higher energies have smaller baryon chemical potential however maximum reached temperature is higher.

## 1.4 Observables

Studying QGP and hot hadronic matter is a challenging task due to its short lifetime, which is on the order of $10^{-23}$ s. Therefore, QGP cannot be studied by the
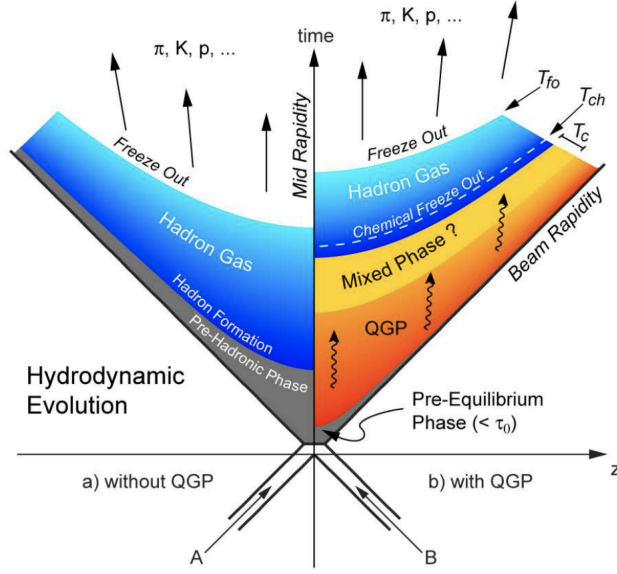
Figure 1.6: Schematic representation of a heavy-ion collision, plotted as a function of $t$ (time) and $z$ (distance), considering a scenario without (left panel) and with (right panel) the creation of a QGP. From [11].
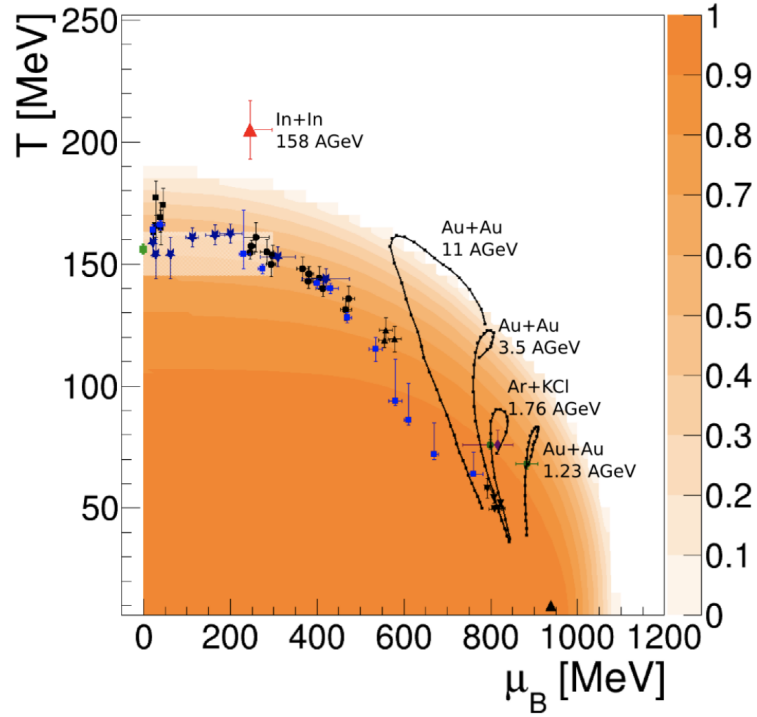


Figure 1.7: Phase diagram of QCD at temperature $T$ and baryon chemical potential $\mu_B$. Lines are time evolution of the collisions. Measured points come from the fit of the statistical model to the particle yields. On z-axis is the quark condensate $\langle \bar{q}q \rangle_{T,\mu_B} / \langle \bar{q}q \rangle_{T=0,\mu_B=0}$. From [12].

same methods as long-living states, as it was for example done in the Rutherford experiment. The properties of QGP can be studied using probes that are produced in the collisions and propagate through the QGP where they interact. Many different observables have been proposed for this purpose.

### 1.4.1   Nuclear modification factor

Nuclear modification factor $R_{AA}$ is one of the most common and powerful tools to measure properties of the hot hadronic matter. It is defined as:

$$R_{AA} = \frac{\mathrm{d}N_{AA}/\mathrm{d}p_T}{\langle T_{AA} \rangle \mathrm{d}N_{pp}/\mathrm{d}p_T},\tag{1.2}$$

where $\mathrm{d}N_{AA}/\mathrm{d}p_T$ is particle yield per event measured in nucleus-nucleus collisions and $\mathrm{d}N_{pp}/\mathrm{d}p_T$ is particle yield per event measured in proton-proton collisions. $\langle T_{AA} \rangle = N_{coll}/\sigma_{NN}^{inel}$ is the nuclear overlap function, where $N_{coll}$ is number of collisions scaling factor (which is often inferred from Gauber model) and $\sigma_{NN}^{inel}$ is inelastic cross-section for NN scattering. If there are no available measurements for proton-proton collisions the denominator is often replaced with results from peripheral collision since there is no expected effect of the hot hadronic matter or QGP. Value of $R_{AA} = 1$ indicates no additional effect in heavy ion collision in comparison with proton-proton, when it is smaller than one it means suppression and when it is higher than one it shows enhancement. In Figure 1.8 you can see measured nuclear modification factor for different particle species at the LHC. Red and magenta points show large suppression of charged hadrons in heavy ion collisions. In stark contrast, $R_{AA}$ for $\gamma$, $W^{\pm}$ and $Z^0$ is equal to one at higher $p_T$ which indicates no additional effect of heavy ion collisions since these particles do not interact strongly with the medium.
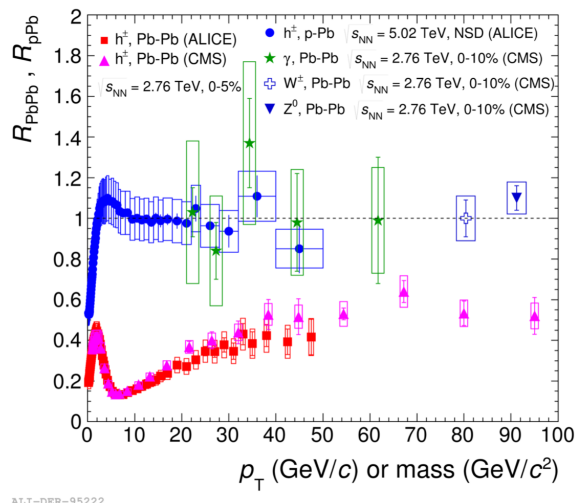


Figure 1.8: Results on nuclear modification factor dependence on the $p_T$ for Pb+Pb and p+Pb collisions at the LHC. From [13]

## 1.4.2 Flow

The so-called "flow" in HIC is a term used for the collective behaviour (correlation of multiple particles) that is reflected in the measured final state spectra. The transverse expansion of the medium (called radial flow) affects the shape of the observed spectra $p_T$. The "blue shift" of the $p_T$ spectra of the particles can be expressed as $p_T \approx p_T^{th} + m\langle\beta\rangle$, where $p_T^{th}$ is the thermal contribution and $m\langle\beta\rangle$ is the contribution from the collective expansion, $m$ is the mass of the particles and $\langle\beta\rangle$ is the average transverse flow velocity. Figure 1.9 shows the effect of radial flow. It has the greatest effect on the spectrum of protons because they have the largest mass. Compared to p+p collisions, protons with small $p_T$ are shifted to higher values, creating the so-called shoulder.

From the measured shape of the spectra one can deduce the velocity and effective temperature of system at the time of kinetic freezout. In Figure 1.9 you can see dependence of $T_{kin}$ on $\langle\beta\rangle$. As can be seen $\langle\beta\rangle$ is decreasing from central to peripheral collisions which indicates more rapid evolution of central collisions. Higher values of $T_{kin}$ in peripheral collisions corresponds to shorter life time of the fireball.
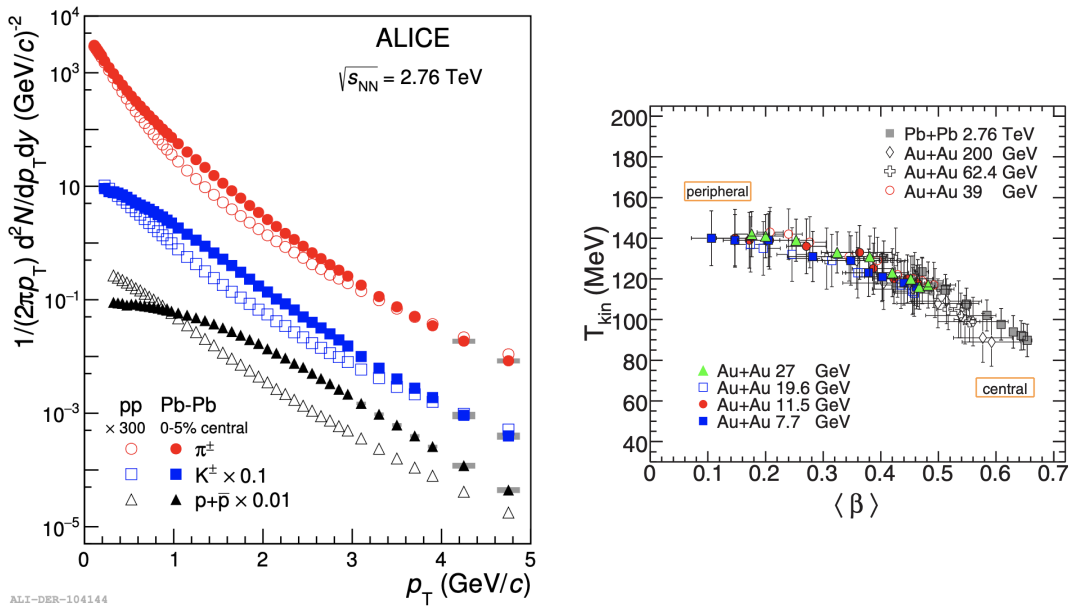


Figure 1.9: Left: Invariant yield in Pb+Pb collisions at $\sqrt{s_{NN}} = 2.76\,\text{TeV}$ for pions, kaons and protons and its comparison with p+p collisions. From [14]. Right: Measured kinetic temperature dependent on $\langle\beta\rangle$ from RHIC beam energy scan and from other experiments. From [15].

The so called anisotropic flow is measured as an anisotropy in the azimuthal distribution of the produced particles with respect to the event plane. It can be studied for a variety of particles, such as hadron flow, strange particle flow, and many others. The main idea is the decomposition of azimuthal part of the spectra into Fourier

series:

$$E\frac{\mathrm{d}^3 N}{\mathrm{d}p^3} = \frac{\mathrm{d}^2 N}{2\pi p_T \mathrm{d}p_T \mathrm{d}y}\left(1 + 2\sum_{n=1}^{\infty} v_n(p_T)\cos\left[n(\phi - \psi_n)\right]\right),\qquad(1.3)$$

where $v_n = \langle\cos[n(\phi - \psi_n)]\rangle$ are the flow coefficients of n-th order and $\psi_n$ is the reaction plane. The reaction plane is given by the impact parameter and the beam direction, but it cannot be measured directly; the symmetry plane defined by the participating nucleons or the event plane must be used instead. Another possibility is to use $Q$ vectors and many-particle correlations. Figure 1.10 shows the definition of the reaction plane.

As often in physics, we are restricted to the first few coefficients due to available statistics. The first coefficient $v_1$ is called the directed flow and arises in the pre-equilibrium phase of the collision and corresponds to the nuclear remnants. The second coefficient $v_2$ is called elliptic flow and it is one of the most important observable in HIC. If we have a non-central collision of two ions, the overlap of the collision zone is asymmetric in the transverse plane with gradients in the density of the created matter. If the system interacts strongly (and possibly thermalizes) it translates into gradients in the pressure driving the expansion of the system. The value of $v_2$ is most important for mid-peripheral events, because in central collisions the created system is symmetric.

The elliptic flow is very important from a theoretical point of view because it can be predicted by many models and allows access to the equation of state of the matter produced at early stages of the collision.
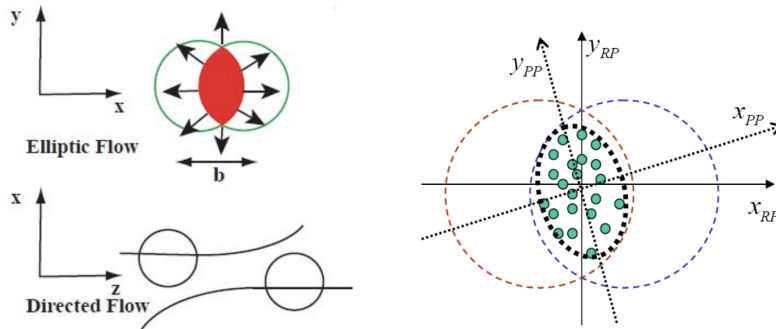


Figure 1.10: Left: The definitions of the Reaction plane and the Participant plane. Right: Diagrams of elliptic flow and directed flow. From [16]

In Figure 1.11 you can see dependence of the slope $v_1$ and $v_2$ on energy of the collision [17]. For higher energies $v_2$ has positive sign which means that more particles are produced in-plane. When the energy is smaller than approximately $\sqrt{s_{NN}} < 7\,\mathrm{GeV}$ flow starts decreasing and for energies smaller than $\sqrt{s_{NN}} < 4\,\mathrm{GeV}$ the flow is negative. The negative $v_2$ at the lowest energies is caused by shadowing effect of the passing spectators (spectators are at these energies slow and they are located in the in-plane direction). On the other hand, positive $v_2$ is created by strong partonic

expansion at the beginning of the collision and it is often interpreted as a sign of the formation of the QGP.
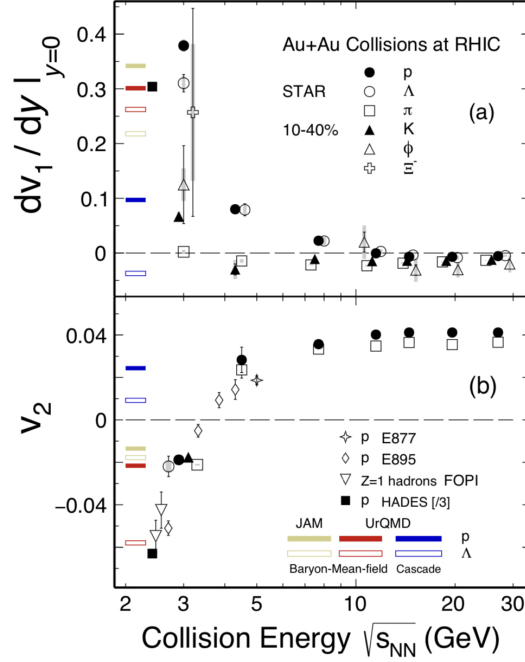


Figure 1.11: Energy dependence of the slope $v_1$ and $v_2$ on collision energy for different particles. Data from RHIC have centrality bin $10 - 40\%$ and collision energy. From [17]

In figure 1.12 you can see results on the measured $v_2$ divided by the number of constituent quarks and its dependence on the transverse kinetic energy. The $v_2$ of particles produced in a collision at $\sqrt{s_{NN}} = 3\,\text{GeV}$ is negative and there is no scaling. The disappearance of scaling is due to the fact that these collisions are not dominated by parton interactions and baryon scattering dominates. It can also be seen that the scaling pattern depends on the actual number of constituent quarks; separate scaling for baryons and mesons. This has been confirmed by measuring the $\phi$ meson, which is heavy (and given its mass we would expect baryon-like scaling) and scales like the other mesons [18].

### 1.4.3 Production of photons

Another experimental probe used to search for the presence of QGP is the detection of emitted photons. Photons are neutral particles and therefore do not interact strongly in QGP. Because QGP has a certain temperature, it emits thermal photons like blackbody radiation, and therefore it should be possible to measure its temperature. This approach suffers from a large background due to the fact that photons are produced throughout all of the collision phases. Hard photons can be produced at the beginning of the collision, bremsstrahlung and photons from decays of particle in the final phase. Other thermal photons come not only from QGP
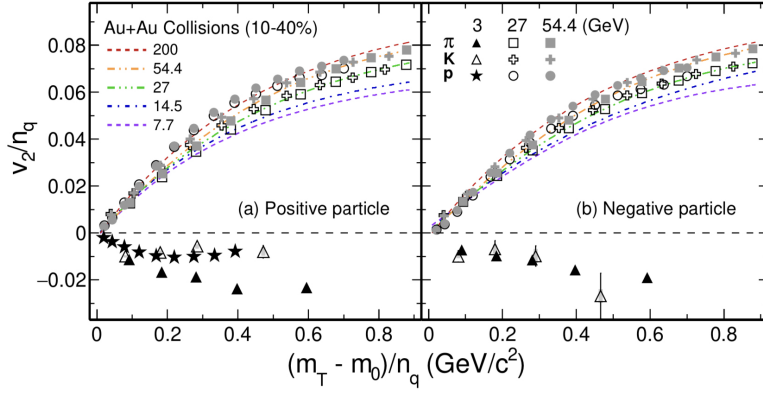
Figure 1.12: $v_2$ scaled by the number of constituent quarks as a function of the transverse kinetic energy for three different collision energies and three different particle species. Coloured lines are fits of the data from STAR experiment. From [17].

but also from thermal radiation of hadrons in the final state. Therefore, the measured temperature is a combination of both and is called the effective temperature $T_{eff}$. In the ALICE experiment, the temperature was measured and the results are shown in figure 1.13. The photons from the QGP are present mostly at the beginning of the spectrum and to extract these photons, the background that dominates this measurement was subtracted. The final result is the measured temperature $T_{eff}^{0-20\%} = (297 \pm 12^{stat} \pm 41^{sys})$ MeV at LHC energies.
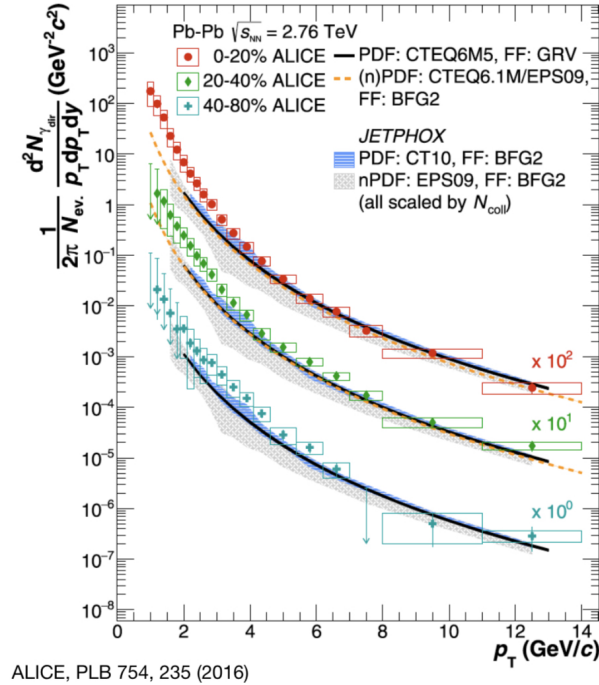


Figure 1.13: Measurement of photons spectrum at ALICE experiment. From [19].

### 1.4.4 Dilepton production

Dileptons are somewhat similar to photons, both are electromagnetic probes. Dilepton pairs are created by decays of virtual photons. Measuring dileptons is even more complicated process due to the even larger number of dilepton production channels. From the beginning of the collision, dileptons can be produced by the Drell-Yan process - annihilation of the quark-antiquark pair (most important for dileptons with large masses), decays of quarkonia, semileptonic decays of the quark-antiquark pair (fragmentation e.g. into $D^0$ and $\bar{D}^0$ mesons, and then into leptons and other particles), which includes all $p_T$, light meson decays (pion annihilation), Dalitz decays ($\pi^0$ into dileptons and $\gamma$), and the same as for photons: thermally produced virtual photons (from QGP and final state). However, dileptons can be used to measure quarkonium production, which is discussed below. The measurement of dileptons is one of the key objectives for the CBM. Figure 1.14 shows of dileptons spectrum measured by HADES collaboration.
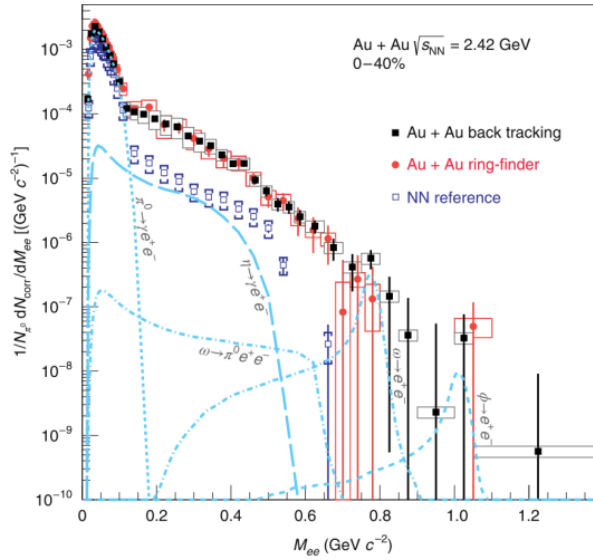


Figure 1.14: Measurement of the di-electron spectra in Au+Au collisions at 2.42 AGeV with HADES. From [20].

### 1.4.5 Heavy quarks

Heavy quarks are an important probe because they are not present in the initial state and must be produced during the collision. The problem with this probe is the quark confinement, because of which we are not able to detect these quarks directly. The heavy quarks are the $b$ and $c$ quarks, which, due to their large masses (on the order of GeV), can only be produced in the initial state (hard scattering) of the collision and then interact with the QGP. The advantage is that the initial production of these quarks can be calculated using pQCD (small coupling constant). However, similarly to the light quarks, their interaction with the system cannot be

calculated using the same approach due to the larger coupling constant at smaller $Q^2$. There are two types of probes. Open heavy flavor particle species, such as mesons $B$ and $D$, and quarkonia, such as $J/\Psi$. The interaction of heavy quarks with QGP is usually measured via the nuclear modification factor $R_{AA}$. At RHIC and LHC collision energies, a significant suppression of open-charm hadrons has been observed indicating existence of strongly interacting medium.

Quarkonium suppression is one of the probes used to infer the temperature of the QGP. When quarkonium is embedded in QGP, it can dissolve in it due to the color field present. In QED, this has an analogy with Debye screening. How much the quarkonium dissolves is determined by the temperature of the QGP and the binding strength of the quarkonium. The $\Upsilon(1, 2, 3S)$ can be used as a QGP thermometer. Such measurement was performed, among others, by the CMS collaboration and the results can be seen in Figure 1.15. $\Upsilon(3S)$ has the lowest binding energy and is suppressed by the highest factor. The suppression factor is also higher for more central collisions. The $\Upsilon$ has been measured through its decay to a pair of $\mu$.
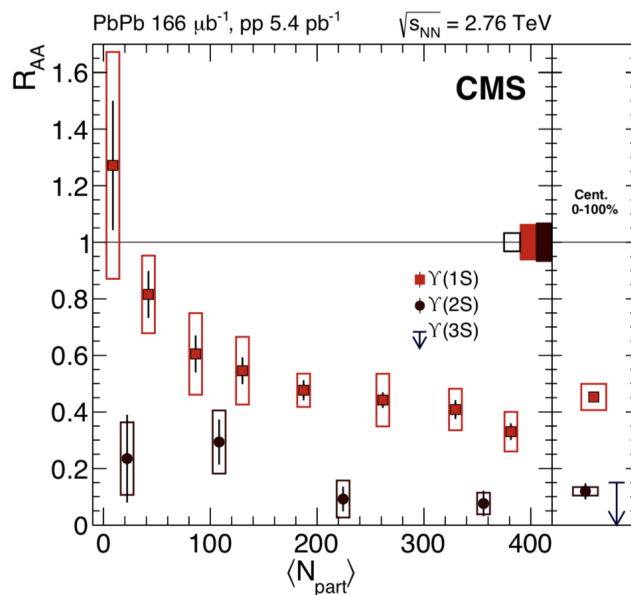


Figure 1.15: Measurement of $R_{AA}$ for $\Upsilon$ by CMS collaboration. From [21].

As described above, flow is an important observed phenomenon in heavy ion collisions. This is also true for heavy quarks, and this measurement can provide information about the interactions between heavy quarks and the deconfined medium. Figure 1.16 shows flow $v_2$ of average $D^0, D^+, D^{*+}$ and $v_2$ of pions. Despite the fact that the mass of the charm quarks is much higher then mass of light quarks the $v_2$ is similar for pions and for $D$ mesons. Thus interaction between the medium and charm quark is strong enough to cause collective behavior of the $c$ quarks.
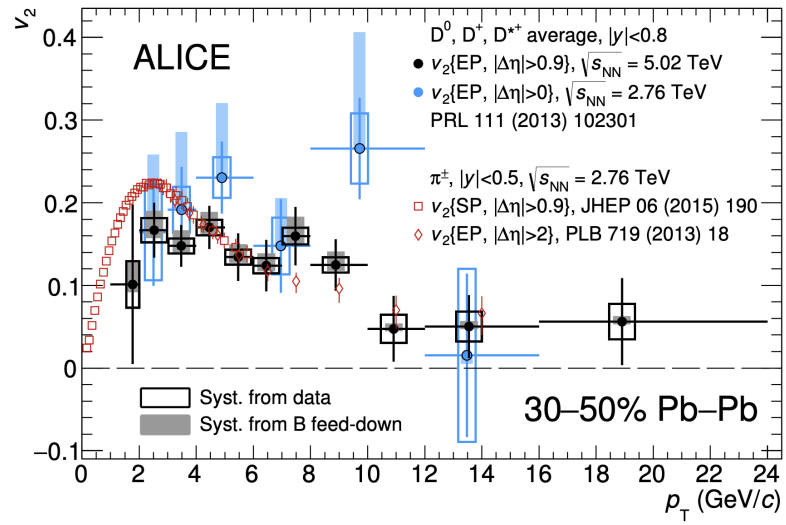
Figure 1.16: Average of $D^0, D^+, D^{*^+}$ $v_2$ in Pb+Pb mid-peripheral collisions at $\sqrt{s_{NN}} = 5.02\,\mathrm{TeV}$ as a function of $p_T$ compared to the same measurement at lower energy $\sqrt{s_{NN}} = 2.76\,\mathrm{TeV}$ and $\pi^\pm$ $v_2$. From [22].

# Chapter 2

# Production of strangeness in heavy ion collisions

The strangeness [18, 23] is another important observable in heavy ion collisions and its importance for intermediate energies is even greater. Since strangeness is conserved in nuclear collisions and the fact that there are no strange quarks in the initial state, the number of produced strange and antistrange quarks must be equal. Particles with strange quark have strangeness number of -1 and particles with antistrange quark have strangeness number of +1. Strange particles can be produced in NN collisions and due to strangeness conservation is the most energetically favorable process:

$$NN \rightarrow N\Lambda K. \tag{2.1}$$

For this process, the value of $Q$ can be calculated as $Q = m_\Lambda + m_K - m_N = 670\,\text{MeV}$. However in QGP, the fusion of two gluons or two light quarks can produce strange-antistrange pairs without the production of accompanying light quarks. Figure 2.1 shows the production rate of strange-antistrange pairs from the fusion of quarks and gluons. The gluon fusion rate is greatly favored compared to quark fusion [24].

The value of $Q$ for this process is proportional to the strange mass, i.e. $Q_{\text{QGP}} \approx 200\,\text{MeV}$. As a result, the production in the QGP should be much higher. In addition, the equilibration time for parton (gluon) fusion is much shorter than the time in hadronic (NN) interactions [25]. For temperatures $T = 200\,\text{MeV}$, the equilibration time is $\tau_{\text{QGP}} \approx 10\,\text{fm/c}$, which is of the order of the heavy ion collision time. However, the duration of the QGP phase may be shorter than this time and the system may not end in chemical equilibrium. On the other hand, in a free hadronic gas, the time to reach equilibrium is strongly dependent on the strangeness. For $\Lambda$ or kaons is $\tau_{\text{HG}} \approx 30\,\text{fm/c}$ and for particles with higher strangeness (for example $\Omega$) the time scale should be ten times longer. Thus, the production of multi-strange particles would be strongly suppressed in hadronic gas compared to QGP. Another effect increasing the production of strange particles is coalescence. If more strange quarks are produced in a collision, they can pair up during the hadronization phase and further increase the production of multi-strange particles in the presence of
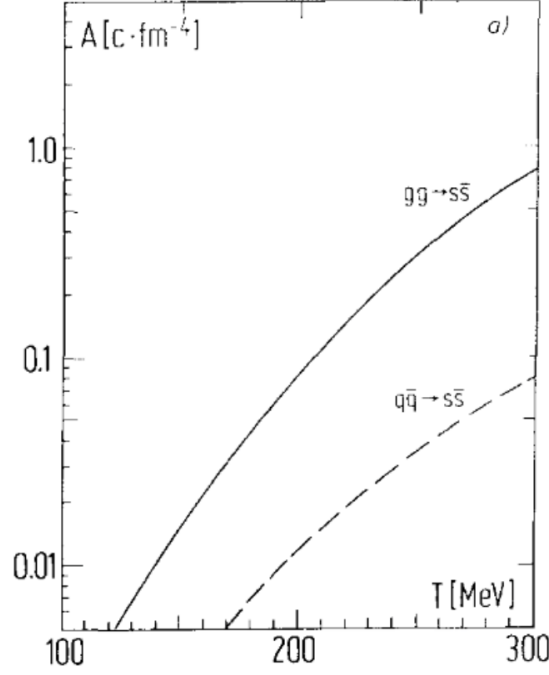
Figure 2.1: Production rate of strange-antistrange pair from different channels dependent on the temperature. From [24].

QGP [26].

In Fig. 2.2 are shown ratios of $K^+/\pi^+$ and $\Lambda/\pi^-$ and its dependency on the energy of the collision. At lower energies, strangeness is confined in hadrons which causes the strong dependence of the ratio on collision energy. Critical energy where first-order phase transition is assumed corresponds approximately to $\sqrt{s_{NN}} \approx 7-8\text{GeV}$. At energies higher than the critical energy ratio of $K^+/\pi^+$ is almost flat. $K^+$ are carrying almost half of produced antistrange quarks so it is proportional to total antistrangeness production. $\pi^+$ is on the other hand proportional to the entropy production, therefore, this ratio can tell us information about the strangeness to entropy ratio. The maximum for particles with higher strangeness content ($\Omega$ and $\Xi$) is shifted to higher values of energy. This is in disagreement with hadron gas model which predicts maximum strangeness production due to the highest net-baryon density. However, this data are not precise enough and it is expected that CBM will measure these ratios with higher precision.

Another important observable [27] is yield per participant relative to proton-proton collision for strange particles. It is expected that multi-strange particles will be enhanced in comparison with proton-proton collision when QGP occurs. Such results can be seen in Figure 2.3. There are presented data from three different experiments at different collisions energies. You can see that enhancement is dependent on the number of participants thus on the volume (higher volume causes longer lifespan of the fireball). Data from NA57 are more enhanced due to the highest net-baryon densities. Also $\Omega$ is more enhanced in comparison with $\Xi$ due to its higher strangeness content.
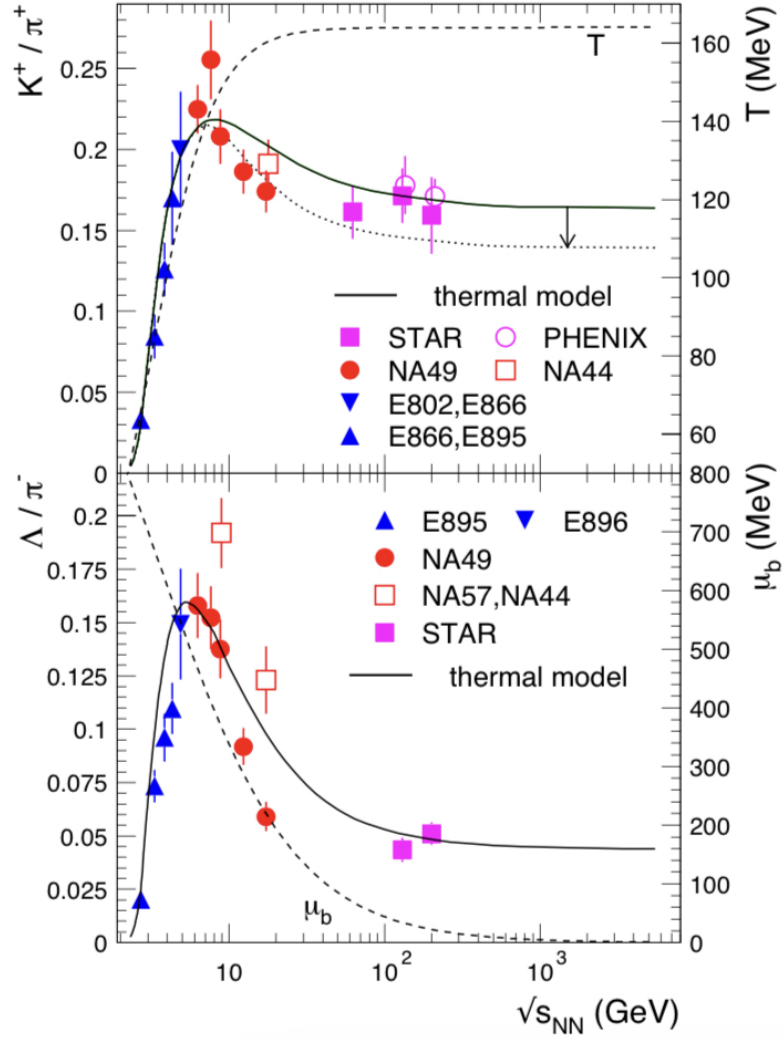
Figure 2.2: Energy dependence of $K^+/\pi^+$ and $\Lambda/\pi^-$ ratios. The solid line comes from statistical model calculations. The dotted line gives results for the ratio including higher mass resonances. The dashed line corresponds to temperature/baryon chemical potential. From [18].

Additionally, dependence of yields ratios of different particles to pions as a function of $\langle \mathrm{d}N_{ch}/\mathrm{d}\eta \rangle_{|\eta|<0.5}$ for Pb+Pb, p+Pb and p+p collisions is shown in Figure 2.4. Strange to non-strange ratio is significantly dependent on the multiplicity and for higher multiplicities this ratio is higher.

## 2.1 Statistical hadronization model

Statistical hadronization model [27, 29] describes production of particles in nucleus-nucleus collisions using methods of statistical physics. The collision is evolving, as it was described in previous chapter, when the system reaches critical temperature $T_c$ hadronization occurs. For purpose of the statistical hadronization, the system
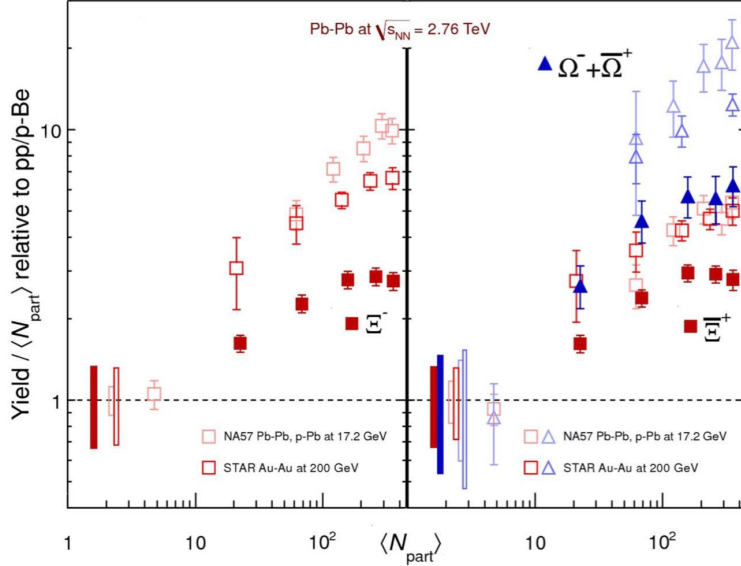
Figure 2.3: Enhancements of strange particles in rapidity $|y_{CM}| < 0.5$ as a function of number of participants. Full data are from LHC, dark open symbols are from RHIC and light open symbols are from NA57. From [27].

is assumed to be in thermal equilibrium. The system can be described using two different partition functions - Canonical and Grand Canonical. In Grand Canonical ensemble:

$$Z^{\mathrm{GC}}(T, V, \mu_Q) = \mathrm{Tr}\left[e^{-\beta(H - \sum_i \mu_{Q_i} Q_i)}\right], \tag{2.2}$$

where $\beta$ is an inverse temperature, $H$ is Hamiltonian of the system (usually Hamiltonian of hadron resonance gas), $Q_i$ are conserved charges and $\mu_{Q_i}$ are chemical potentials of conserved charges. These are electric charge, baryon number and strangeness. Reduction of the parameters can be done via strangeness neutrality and fixation of charge potential by initial isospin asymmetry. Only two parameters are left - temperature $T$ and baryon chemical potential $\mu_B$. Using this approach one can derive particle ratios which can be measured (see Figure 2.5). You can see that the data agree well with predicted values at energies 40 AGeV. In the next Figure 2.6 you can see particle yields as measured by the ALICE experiment. The data are in a good agreement with the fit using the statistical model. Thus, the Grand Canonical function approach can describe well data from AGS, RHIC and LHC.

However, this approach is not valid at lower energies. Grand Canonical description is appropriate only if the number of produced particles carrying the conserved charge is high. In this approach, the net value of charges fluctuates event-by-event and when the number of produced particles is sufficiently high these fluctuations can be neglected. Nevertheless, at low energies multiplicities are low and fluctuations can not be neglected any more. In this case, a Canonical description with explicit charge conservation in each event should be used. In Figure 2.7 you can see predicted $T-\mu_B$ lines from observed particle ratios in different collisions. In the Ni+Ni collisions,
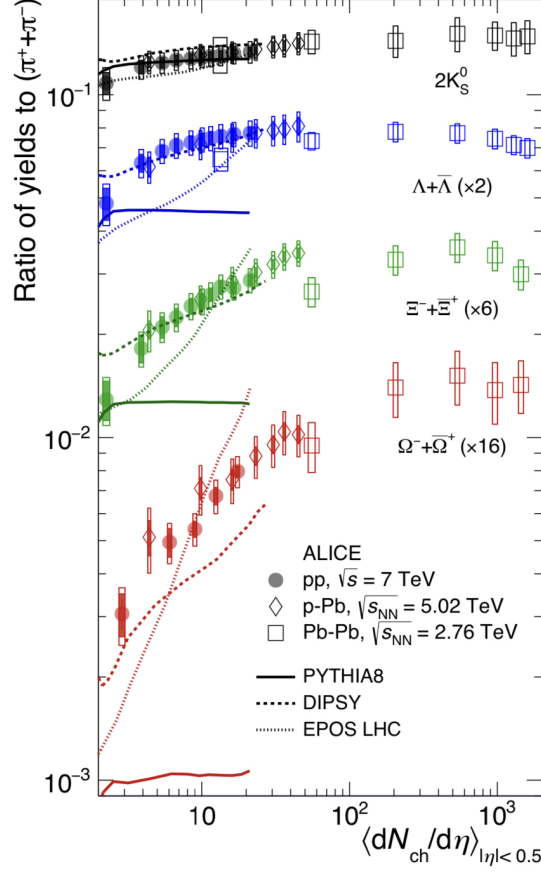
Figure 2.4: Yields ratios of different strange particles to pions as a function of $\langle \mathrm{d}N_{ch}/\mathrm{d}\eta \rangle_{|\eta|<0.5}$. Data from p-p and p-Pb as well as MC simulations are also shown 2.4. From [28].

all lines (except one) meet around $T \approx 70\,\mathrm{MeV}$ and $\mu_B \approx 760 MeV$. In Au+Au collisions this point lays around $T \approx 53\,\mathrm{MeV}$ and $\mu_B \approx 822 MeV$. Therefore with increasing collision energy temperature increases and baryon chemical potential is decreasing. The value of $T$ and $\mu_B$ in Au+Au collisions can be used to demonstrate the problem of the Grand Canonical approach. Results for the $K^+/\pi^+$ ratio for this approach with observed $T$ and $\mu_B$ would be about $K^+/\pi^+ \approx 0.04$ which actually overestimates data more than an order of magnitude at the energy $1.0\,\mathrm{AGeV}$ as measured by [31].

Based on the measured particle ratios in heavy ion collision at different collisions energies baryon chemical potential can be phenomenologically parameterized using CMS energy of collision $\sqrt{s}$ as [29]:

$$\mu_B = \frac{a}{1 + \sqrt{s}/b},\tag{2.3}$$

where $a = 1.27\,\mathrm{GeV}$ and $b = 4.3\,\mathrm{GeV}$.

In Figure 2.8 (left) you can see results for freeze-out parameters $T$ and $\mu_B$ from different experiments. From the phenomenological point of view, all these points have
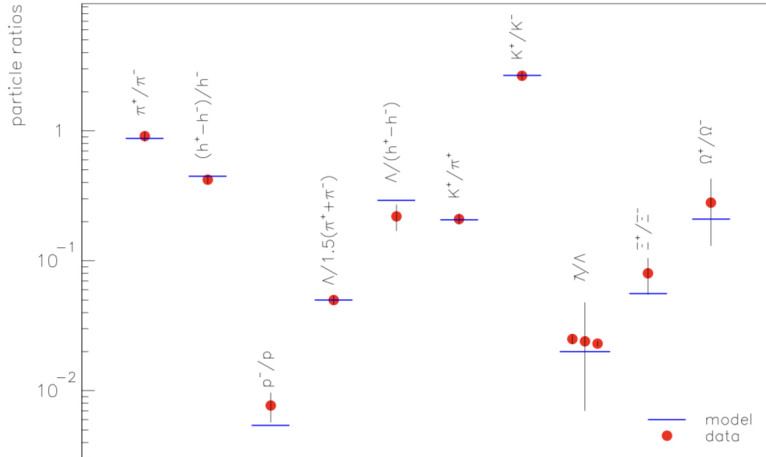
Figure 2.5: Measured particle ratios in Pb-Pb collisions at $40\,\mathrm{AGeV}$ compared with predications from statistical model with $T = 148\,\mathrm{MeV}$ and $\mu_B = 400\,\mathrm{MeV}$. From [29].

the same ratio of average energy $\langle E \rangle$ over an average number of hadrons $\langle N \rangle$ about $1\,\mathrm{GeV}$. Suggesting common condition for chemical freeze-out $\langle E \rangle / \langle N \rangle \approx 1\,\mathrm{GeV}$. For thermally excited nuclear matter in non-relativistic approximation, this ratio can be written as [29]:

$$\frac{\langle E \rangle}{\langle N \rangle} = \langle m \rangle + \frac{3}{2}T, \tag{2.4}$$

where $\langle m \rangle$ is the thermal average mass in the fireball. At SPS energies the mostly produced particles are pions, however their mass does not correspond to $\langle m \rangle$ (since $T$ can be neglected). This can be explained by the fact that most of the pions during the freeze-out are hidden in mesonic and baryonic resonances and the $\langle m \rangle$ corresponds to the mass of $\rho$ meson.

## 2.2 Kinetic transport models

In addition to the statistical model of hadronization, kinetic transport models [18,33] can be used to describe heavy ion collisions. Kinetic transport models provide an important framework for comparing experimental data with theoretical predictions. These models are based only on hadronic degrees of freedom and string excitations. They can answer the question whether the data can be described by pure hadronic interactions or whether parton interactions are needed, even some mean-field potential can be added.

Kinetic models can be divided into two groups: with or without hydrodynamics. The first are called microscopic transport models. The main idea is to describe collision as interactions of many bodies at the microscopic level based on elementary degrees of freedom. The collision dynamics is governed by the Boltzmann equation, which
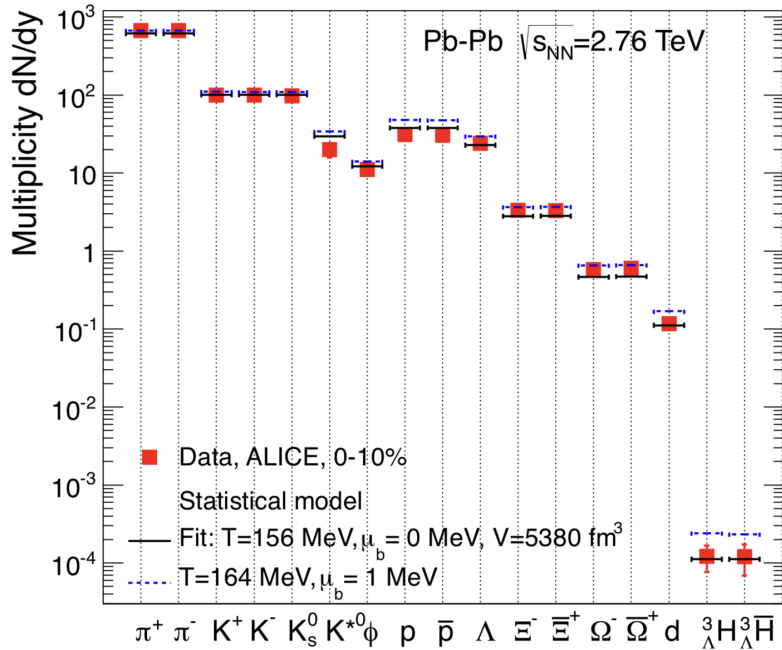
Figure 2.6: Hadron yields measured by ALICE at the LHC with statistical hadronization fit. From [30].

is unfortunately purely classical. One can also add a certain mean-field potential to this equation.

## 2.2.1 UrQMD

Ultrarelativistic quantum molecular dynamics (UrQMD) [34] is one of the widely used kinetic models. The initial hadrons are represented individually as Gaussian distributions, allowing fluctuations to be studied event by event. Hadrons and their resonances (more than 50 baryon and 40 meson species) are chosen as the degree of freedom. Interactions between two particles include soft and hard potential interactions. At higher energies, a cascade mode can be used in which particles propagate in straight lines from collision to collision or decay. The cross-sections are taken from experimental data for lower energies (resonance cross-sections). At higher energies ($\sqrt{s_{NN}} > 3\,\mathrm{GeV}$) a string degree of freedom is added to fill the difference between the inelastic and resonance cross-sections.

UrQMD works as follows. Initially, two nucleons interact when two hadrons are closer than $d < \sqrt{\sigma_{tot}/\pi}$, where $d$ is the impact parameter and $\sigma_{tot}$ is the total cross-section. The product of this interaction then evolves until the next interaction or decay.

Subthreshold particle production can be studied using this kinetic model using a multi-step process. For example, a nucleon in the initial state may gain energy by elastic scattering before interacting with another nucleon to produce a particle. This process is strongly influenced by the potential in the environment. Therefore,
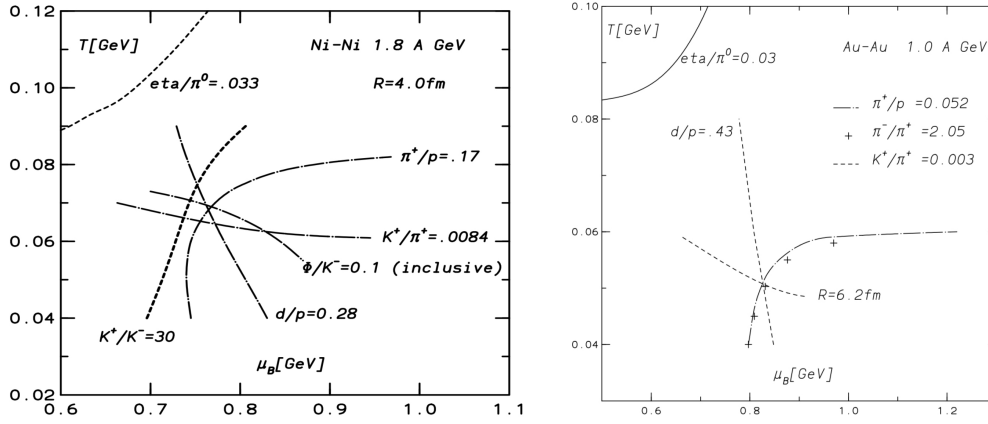
Figure 2.7: Calculated $T - \mu_B$ lines for particle ratios observed in Ni-Ni collisions at 1.8 AGeV (left) and Au+Au collisions at 1 AGeV (right) at SIS. From [29, 31].
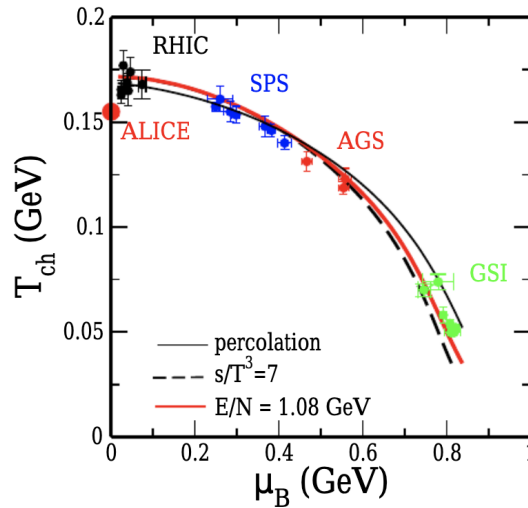


Figure 2.8: A compilation of results for chemical freeze-out points from several experiments with statistical hadronization model prediction (red line). From [32].

subthreshold production is an important observation to better describe the potential in the environment.

UrQMD describes the experimental data well, but at high collisions energies shows signs of deviation because UrQMD cannot describe the complete parton evolution. Therefore, a hybrid UrQMD model was introduced in which the hottest and densest phases evolve using a hydrodynamic approach.

The difference between the predictions of the models and measurements can be demonstrated on the $\phi$ meson production. The $\phi$ meson [23] is composed from $s\bar{s}$, which means its net strangeness is zero, however it is sensitive to strangeness production scenarios and its enhancement was suggested as an indicator for QGP. At the RHIC energies the $\phi$ production is well described by Hadron gas model [35]. But at SPS Hadron gas model and also the kinetic model fail to describe the data. This can be seen in Figure 2.9.

38
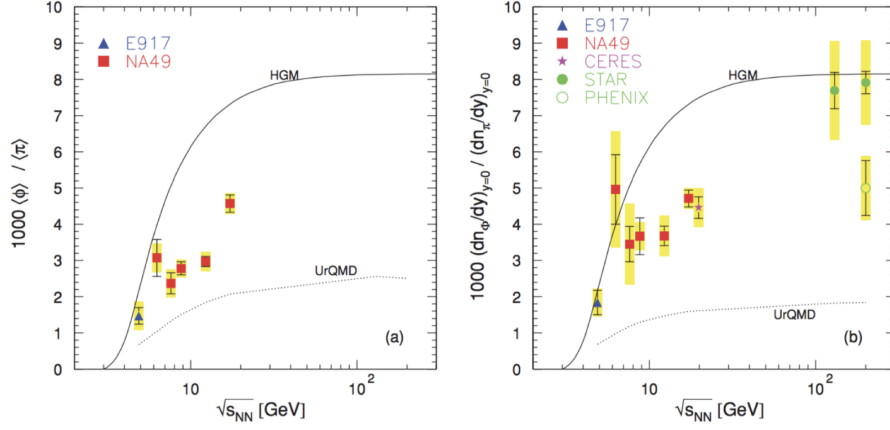
Figure 2.9: $\phi/\pi$ ratio measured in Pb+Pb and Au+Au collisions dependent on collision energy in full space (left) and at mid-rapidity (right). Full line is prediction from Hadron gas model and dotted line represents UrQMD. From [35].

## 2.3 Production of $\Lambda$ baryon

$\Lambda$ is particle composed of three quarks $uds$. Therefore besides $\Lambda$, another particle with strangeness $+1$ must be produced in NN collision. This fact has a large impact on the threshold energy of $\Lambda$ production. Threshold energy can be calculated as the sum of rest energy of all produced particles $N_{prod}$:

$$\sqrt{s_{trh}} = \sum_{i=1}^{N_{prod}} m_i c^2, \qquad (2.5)$$

where $m_i$ is mass $i$-th produced particle. For $\Lambda$ production at the threshold energies, the most important production is with $K^+$and $K^0$, due to their masses. Center of mass energy per nucleon for collisions can be calculated using 1.1. In this thesis collisions of Au+Au at $1.23\,\text{AGeV}$ and Ni+Ni at $1.93\,\text{AGeV}$ are considered and their corresponding center of mass energies per nucleon collision is $2.682\,\text{GeV}$ and $2.400\,\text{GeV}$ respectively. Possible production channels for $\Lambda$ production are in Tab. 2.1 together with their threshold energies and the difference between this energy and center of mass energy of selected collision systems. The mass of nucleon N is the arithmetic mean of the proton and neutron. You can see in the Ni+Ni collision system that $\Lambda$ production is above the threshold for both channels. In the Au+Au system energy of the system is below the threshold, however, $\Lambda$ can be produced in this collision due to other effects discussed below.

| Production channel | $\sqrt{s_{trh}}$ | $\sqrt{s_{NN}}\vert_{Au+Au} - \sqrt{s_{trh}}$ | $\sqrt{s_{NN}}\vert_{Ni+Ni} - \sqrt{s_{trh}}$ |
|---|---|---|---|
| NN $\rightarrow$ N$\Lambda$K$^+$ | 2.549 GeV | $-0.149$ GeV | $+0.133$ GeV |
| NN $\rightarrow$ N$\Lambda$K$^0$ | 2.553 GeV | $-0.153$ GeV | $+0.129$ GeV |

Table 2.1: Possible production channels for $\Lambda$, their threshold energies and comparison with center of mass energies in Au+Au and Ni+Ni collisions. [36]

Fermi momentum - Since nucleons are fermions they are subject to the Pauli principle. That means nucleons must populate higher energetic states and they can gain additional momentum up to Fermi momentum $p_F \approx 250\,\text{MeV}$. This means that individual nucleon pairs can collide during initial phase with higher energy that what is the average.

Multistep process - In heavy ion collision nucleons can gain momentum from elastic scatterings before the final NN interaction creates strange particles. Nucleons can also create resonance which afterwards interacts with another nucleon and strange matter is created.

In medium modification [37]. The effective mass of the strange hadron can be different from the vacuum value due to the potential between strange hadron and nucleons. This fact can play a crucial role in neutron stars and their equation of state. Therefore measurement of the sub-threshold production of strange particles is important.

In Fig. 2.10 is shown the measured excitation function of chosen (strange) particles. Despite the mentioned effect which can provide additional momentum to nucleons, the production in the vicinity of the threshold is strongly suppressed in comparison with higher energies.
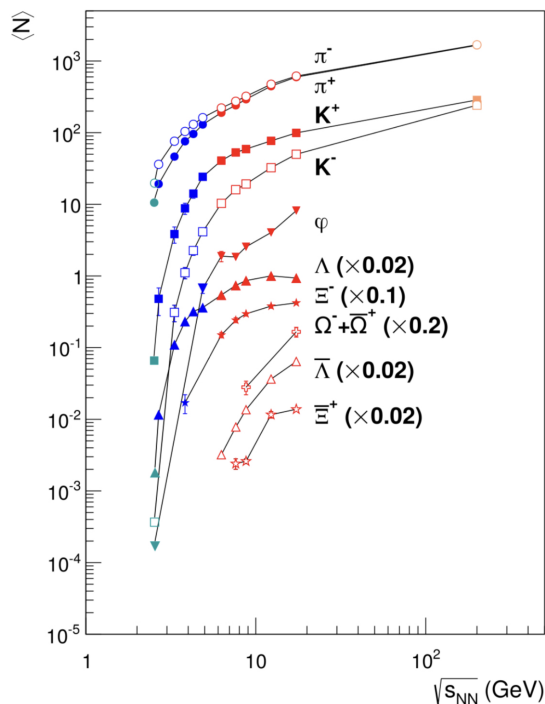


Figure 2.10: Excitation function of the (strange) particles measured at SIS18. From [38].

### 2.3.1 Previous measurement of $\Lambda$

$\Lambda$ production was measured in HADES [39] at energy $\sqrt{s_{NN}} = 2.4\,\text{GeV}$. This was the first measurement of the $\Lambda$ excitation function below its threshold. $\Lambda$ were identified
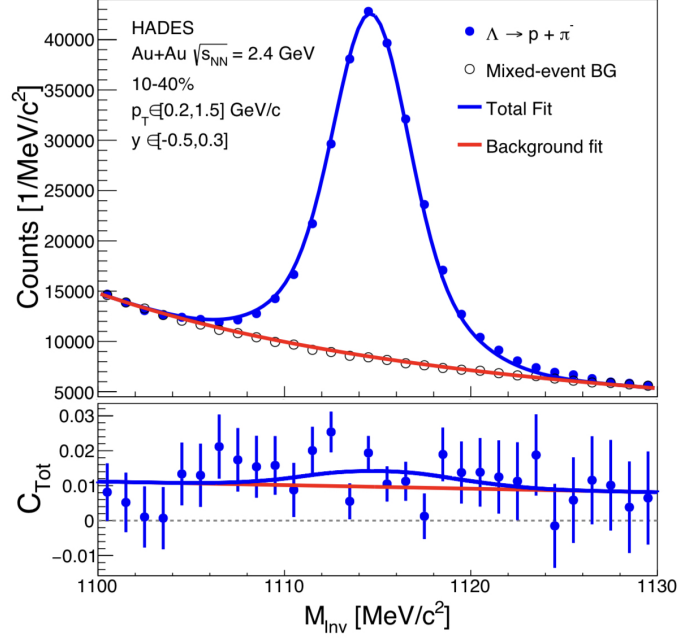
Figure 2.11: The pion-proton invariant mass distribution measured by HADES experiment in Au+Au collision at $\sqrt{s_{NN}} = 2.4\,\mathrm{GeV}$ with centrality $10-40\%$. From [39].

via their decay into proton and pion. An example of the measured invariant mass spectrum is shown in Figure 2.11.

In this paper, the polarization of $\Lambda$ was also measured. The global polarization of $\Lambda$ is arising from vorticity fields which are created in the semi-peripheral collision of heavy ions. Therefore strong dependence on centrality is expected. In Figure 2.12 are presented results for global polarization from many experiments. It can be seen that for high energies the global polarization is compatible with zero. With lowering the energy the polarization increases. The data for more central collisions (red-white points) are lower in comparison with the more peripheral collisions. Also, predictions for different equations of state are presented. Thus measurement of $\Lambda$ polarization at (sub) threshold energies is important observable for the extraction of the equation of the state of the QCD matter.

## 2.4 Equation of state with strangeness

As it was previously mentioned measurements of the production of strange particles at sub-threshold energies are important observables for the determination of the equation of state. At this energies production of strangeness [40] is highly influenced by in-medium interaction and nuclear compressibility. One of the key observables is $K^+$ due to its long mean free path in a dense nuclear medium and absence of absorption. Transport calculations find enhanced $K^+$ production in Au+Au collisions by a factor of two when a soft equation of state is assumed. On the other hand, the repulsive force between $K^+N$ has the opposite effect on its production. In Figure
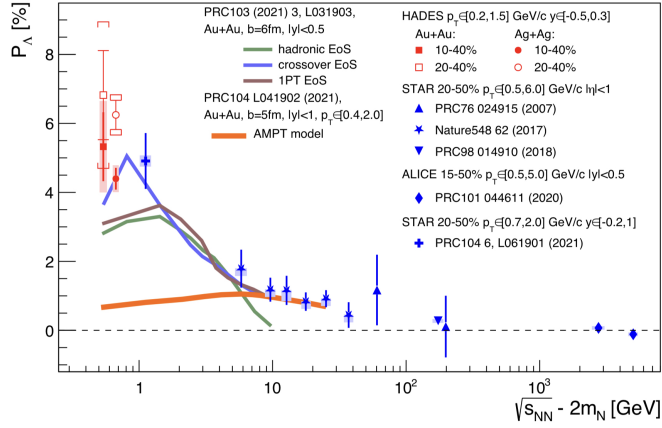
Figure 2.12: Global polarization of $\Lambda$ - dependence on CMS energy from several experiments. The prediction for models with different equations of state is with a full line. From [39].

2.13 are shown results on cross-section for the production of $K^+$ in Au+Au and C+C collisions and prediction for different equations of states with or without in-medium potential. You can see that the cross-section for C+C collisions is influenced more by in-medium potential than the equation of state. In Au+Au collision the effects of in-medium potential are small compared to the effect of the equation of state. Looking closer it can be observed that the measured cross-section agrees more with the soft equation of state rather than the hard one.

The equation of state [41] (EoS) is important not only for description of heavy ions but also for neutron stars. The EoS has a large impact on the radius of neutron stars. Softer EoS leads to smaller radius of neutron stars. You can see this in Figure 2.14. Also the type of the phase transition plays important role for mass-radius dependence.

In order to better picture the link between neutron stars mergers and heavy-ion collisions a simulation of them was made by HADES collaboration. In Figure 2.15 you can see time evolution of two neutron stars merger (top) and time evolution of the heavy ion collision (bottom). While similar energy densities and temperatures are achieved the space and time scales are dramatically different (in space the difference is in the order of $10^{18}$).

## 2.5   In-medium potential

The in-medium potential can be also studied with $K^-$ which has negative charge thus the force $K^- N$ is attractive. In Figure 2.16 are multiplicities per number of participants in Ni+Ni and C+C collisions for $K^+$ and $K^-$. It shows that in nucleon-nucleon collisions $K^+$ multiplicities exceed those of $K^-$ by 1-2 orders of magnitude. Thus in the nucleus-nucleus collision, $K^-$ production has to be much more enhanced in comparison to $K^+$. $K^-$ yields can be explained with strangeness exchange interaction $\pi\Lambda \to K^- N$ and reduction of $K^-$ mass in dense nuclear matter. Also according
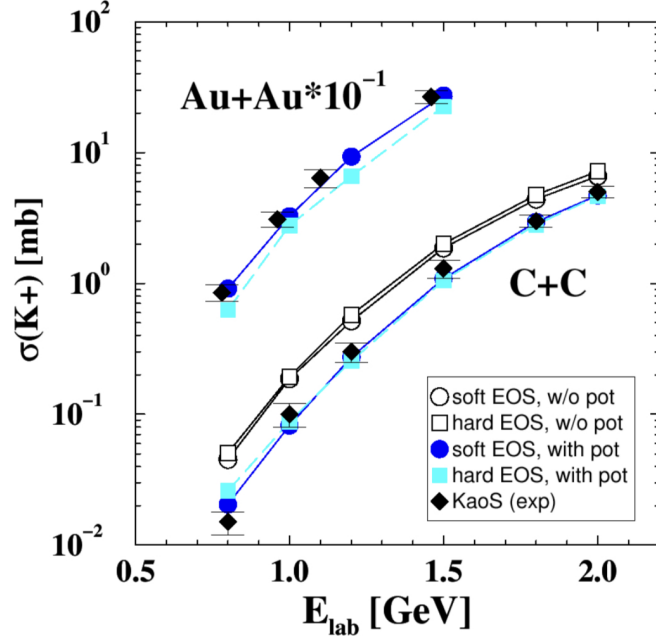
Figure 2.13: Production cross-section of $K^+$ in Au+Au and C+C collisions. Data are black, and predictions for different equations of state are with circles and squares. From [40].
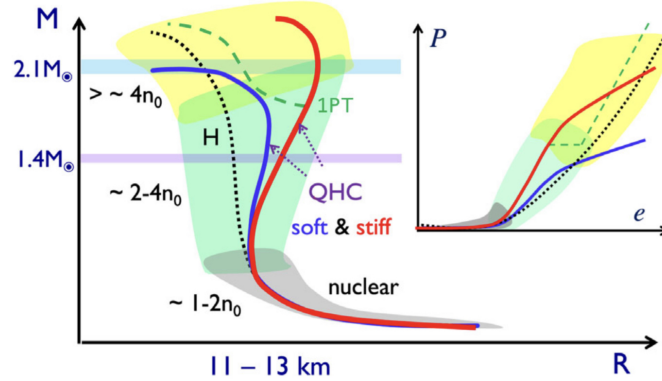


Figure 2.14: Dependence of neutron stars mass on its radius (main figure) and dependence of pressure on energy density (inset) for different equations of state. H refers to purely hadronic EoS, 1PT is a hybrid model with first-order phase transition and QHC refers to EoS with crossover. From [41].

to transport calculations yields of $K^+$ are suppressed by repulsive $K^+N$ potential and yields of $K^-$ are enhanced by attractive $K^-N$.

Another implication of in-medium $K-N$ potentials is the different flow of $K^+$ and $K^-$. Azimuthal distribution of kaons from Au+Au collisions at $1.5\,\mathrm{AGeV}$ is shown in Figure 2.17. Positive kaons have the highest emission at about $90°$ which corresponds to the direction perpendicular to the reaction plane. This behavior is similar to pions, however the reason is different. The flow of pions is caused by a
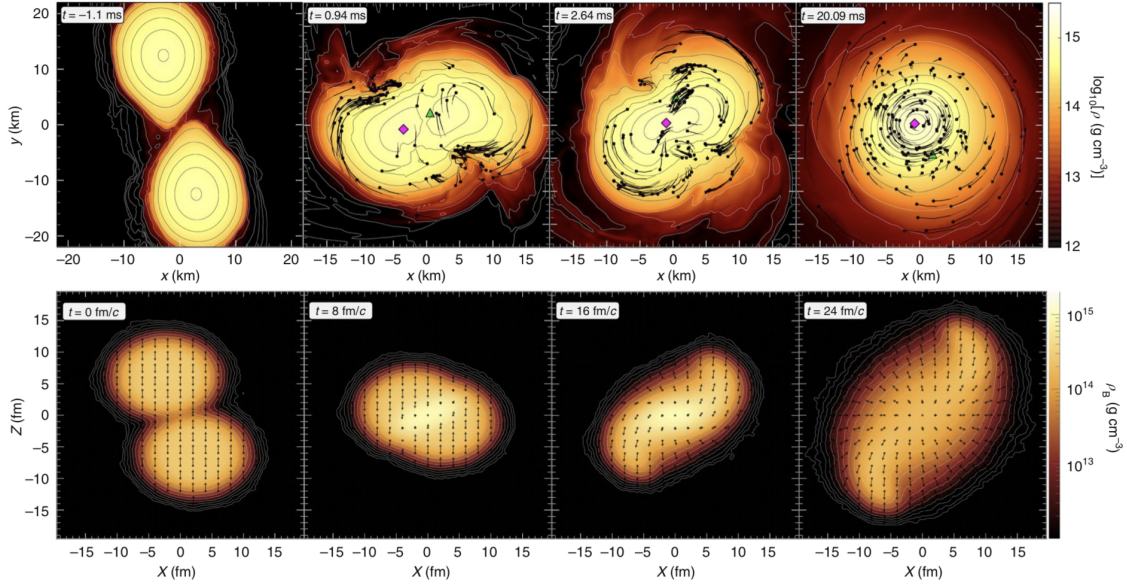
Figure 2.15: Top: Simulation of neutron stars merger with masses $1.35M_\odot$. In the initial state densities are about five times saturation density and temperatures are about 20 MeV. After 20 ms densities are about two times saturation density and temperature is up to 75 MeV. Magenta point indicates the highest density and green point indicates the highest temperature. Bottom: Simulation of time evolution of the central Au+Au collision at energies 2.42 GeV per colliding nucleon pair. Reached densities are about three times normal matter densities and temperature up to 80 MeV. From [42].

small mean free path in dense nuclear matter. In the case of $K^+$ it can be only explained by in-medium repulsive potential. However, the flow of $K^-$ is expected to be isotropic if the in-medium attractive potential is present and this agrees with measured data (Figure 2.17 right).
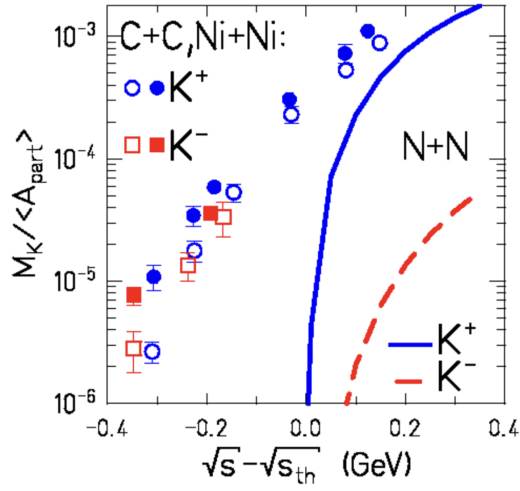
Figure 2.16: Multiplicities per number of participants of $K^+$ and $K^-$ in Ni+Ni and C+C collisions. The lines correspond to the parametrisation of the production cross-section in nucleon-nucleon collisions. From [40].
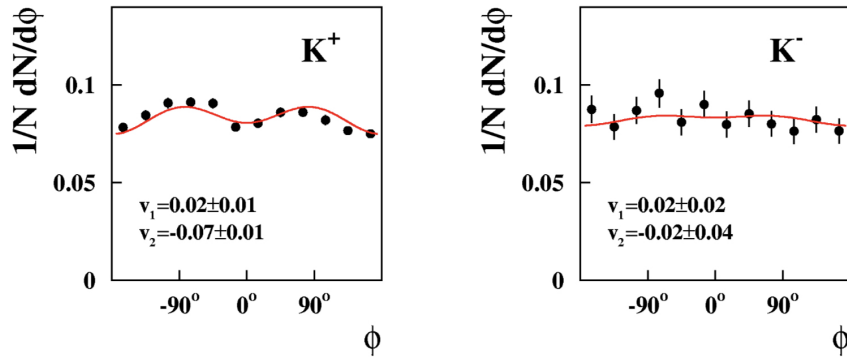


Figure 2.17: Azimuthal distribution of kaons ($K^+$ left, $K^-$ right) measured in semi-central Au+Au collisions at $1.5\,\mathrm{AGeV}$. From [40].

# Chapter 3

# The CBM experiment

## 3.1 GSI

The CBM (Compressed Baryonic Matter) experiment is being built at the FAIR [43] GSI (Helmholtzzentrum für Schwerionenforschung) facility in Germany. The GSI was founded in 1969 and since then has been one of the most important physics research centres. In 1975, the UNILAC accelerator, which is a 120-metre long linear accelerator, was built here. This facility can accelerate all ions from protons to uranium up to energies of $11.4\,\text{MeV/u}$. This accelerator has contributed to the discovery of new elements with atomic numbers from 107 (bohrium) to 112 (copernicium). Currently operational SIS18 is a synchrotron with a circumference of 216 metres, a rigidity of $18\,\text{Tm}$ (rigidity is the maximum available momentum per charge) and can accelerate ions up to energies of $1.23\,\text{AGeV}$ for gold ions and $4.5\,\text{GeV}$ for protons in [44]. This accelerator now provides beams for the mCBM, HADES and many other experiments.

## 3.2 FAIR

The Facility for Antiproton and Ion Research in Europe (FAIR) is part of GSI, which was established in 2010 and has been under construction since 2017. The first phase of construction consists of the SIS100 accelerator and the first experimental facilities (including the CBM cave), which are expected to be completed in 2025. The current status of the work can be seen in figure 3.1. FAIR will consist of new accelerator facilities and new physics experiments. A map of these facilities is shown in figure 3.2. SIS100 [45] is a new synchrotron with a circumference of $1.1\,\text{km}$ and is located $17\,\text{m}$ underground. The older SIS18 will be used to provide beam at the injection energies. Like SIS18, SIS100 has a maximum rigidity of $100\,\text{Tm}$ and the output energy will be from $2\,\text{AGeV}$ to $14\,\text{AGeV}$. In addition, the beam will be injected into the future SIS300 accelerator, which should be able to accelerate to $44\,\text{AGeV}$. However, the realization of the SIS300 accelerator is not certain at this time. The main goal of the FAIR facility is to investigate nuclear matter and its properties,

Figure 3.1: The situation in the FAIR construction site on 28th February 2022.

such as the equation of state, exotic nuclei production, charm production, and many other topics of interest. These goals will be achieved in several experiments, some of them are listed below.
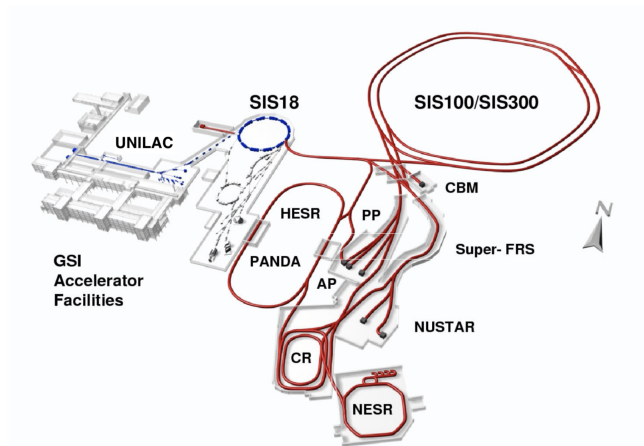


Figure 3.2: Map of experimental facilities in GSI. Older ones are blue, FAIR facilities are red.

NUSTAR (NUclear STructure) experiment is focused on experiments with exotic nuclei. These nuclei will be produced by collisions of heavy ions accelerated by SIS and then selected by Super-FRS (super-conducting fragment separator). PANDA (antiProton ANihilation at DArmstadt) experiment will use antiproton collisions. Antiprotons are produced by the primary SIS proton beam and stored in the HESR (high-energy storage ring) for the use by PANDA experiment. GSI focuses not only on fundamental research but also on applications. For example, proton therapy has been developed at GSI, and research into cancer treatment using protons and heavy ions will continue with the new FAIR facility. Last but not least, it is CBM (Compressed Baryonic Matter) that is the focus of this thesis.

## 3.3   Compressed Baryonic Matter (CBM)

The CBM experiment [46, 47] focuses on the study of dense nuclear matter and its properties. Like other experiments with this goal, CBM will be designed to detect particles produced in collisions of heavy ions. Compared to the two most famous accelerators, RHIC and LHC, whose main focus is on nuclear collisions at very high energies and zero (or very low) baryon densities, CBM will focus on intermediate energies and higher baryon densities in order to investigate the phase diagram in a different region and search for a first-order phase transition and a possible critical point. The geometry of the detector is adapted to this purpose and, unlike the RHIC and LHC experiments, the CBM detector will be a fixed target experiment (instead of a collider). One of the unique features will be its data acquisition system (DAQ) capable of high data acquisition rates of up to $10^7$ interactions per second. This capability will make the CBM sensitive even to very rare probes. One example of heavy ion collision probes at intermediate energies are dileptons originating from vector mesons (e.g. $\rho$). Its yield in heavy-ion collisions is about $10^6$ times lower than the pion yield (as seen in Figure 3.3). Another important probe is the production of (multi-)strange hyperons. This production is also suppressed. These are some of the reasons for the requirements for such high interaction rates.

The continuous readout is challenging compared to earlier experiments there will be no trigger to start the readout. Instead, data will be read continuously, preprocessed online and then stored for offline analysis. The CBM detectors are designed for an event rate of 10 MHz, which corresponds to a beam intensity of $10^9$ ions per second and a 1% target (only one percent chance of beam interaction in the target). Assuming an archiving rate of 1 GB/s and a single event size of 40 kB (corresponding to an Au+Au collision), then only 25 kHz can be received during data acquisition. Therefore, a data reduction algorithm is needed to reduce the data volume by more than 400 times. Fast online event reconstruction is performed on CPU and GPU farms. The track reconstruction is performed based on parallel track reconstruction algorithms implementing, for example, the Kalman filter method. In events with open charm particles ($D$ mesons, etc.), tracking will be used to find secondary vertices and this information will then be used as an online trigger. Events with a $J/\Psi$ meson can easily be triggered using a high energy lepton pairs. A so called "Green IT Cube", new modern computing center, was built to process and store the large amount of data.

The CBM detector consists of several subsystems, as shown in Figure 3.4. The CBM sub-detectors must be extremely radiation hard and very fast due to the high interaction rate. Acceptance of the entire detector will cover the entire azimuth and polar angle between 2.5° and 25°.

There are two different conceived detector setups. The first one is for electron measurements, the second one for measurements with muons. The target for the beam is placed at the beginning of the detector. From this point, the beam continues through a pipe to the PSD (Projectile Spectator Detector) module. The task of the PSD is to detect collision fragments and provide us with information about the centrality and reaction plane of the collision. A silicon tracking detector (STS) is used to deter-
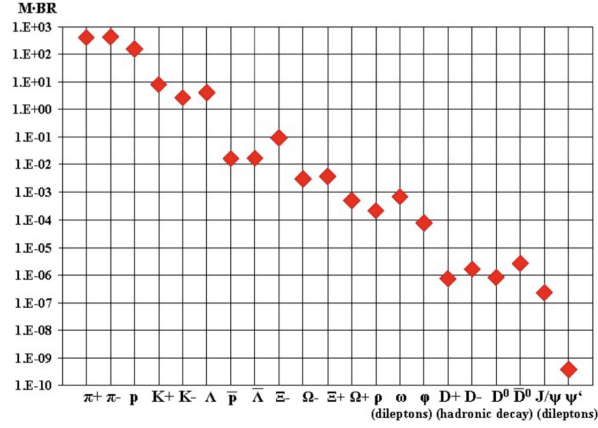
Figure 3.3: Particle multiplicities times branching ratio for central Au+Au collision at 25 AGeV. From [47].
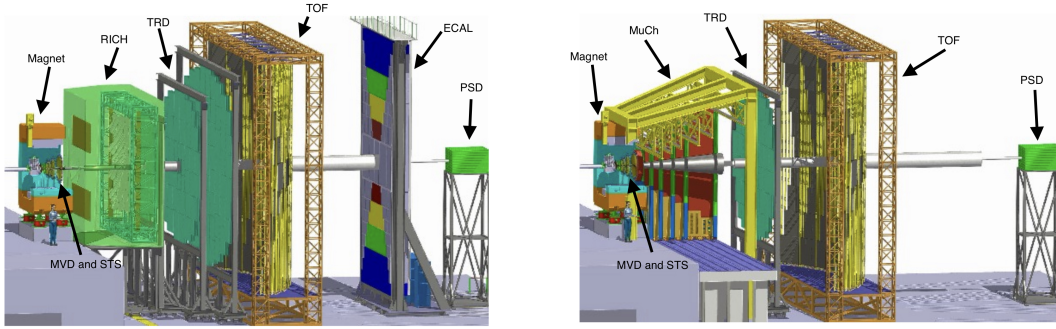


Figure 3.4: Outline of the CBM geometry. On the left is the arrangement for electron measurements (with RICH detector). On the right is the geometry for muon measurements (with MuCh detector). ECAL will not be built.

mine the primary vertex. It is composed of a low-density silicon material. Secondary vertices (from the decayed particles formed in the primary vertex) are reconstructed using the MVD (Micro Vertex Detector). These two detectors are placed in a dipole magnetic field which allows to determine momenta of the detected particles. The magnets are coils of 1749 turns with a maximum magnetic field of 1 T. The next detector for the electron configuration is RICH (Ring Imaging Cherenkov), which is used to distinguish between positrons and protons. The TRD (Transition Radiation Detector) is also used for this purpose. Hadron velocities are measured in the TOF (Time of Flight) composed of the RPC (Resistive Plates Chamber). To detect muons (right setup), the MuCh (Muon Chamber) is substituted for the RICH. Table 3.1 shows which particles are the individual sub-detectors able to observe.

| Observables | MVD | STS | RICH | MuCh | TRD | TOF | PSD |
|---|---|---|---|---|---|---|---|
| $\pi, K, p$ | | x | (x) | | (x) | x | x |
| Hyperons | | x | | | (x) | (x) | x |
| Open charm | x | x | (x) | | (x) | (x) | x |
| Electrons | x | x | x | | x | x | x |
| Muons | | x | | x | | (x) | x |
| Photons | | | | | | | x |
| Photons via $e^{\pm}$ conversion | x | x | x | | x | x | x |

Table 3.1: Particle observability for different detectors. Detectors with "(x)" can be used for the suppression of background. From [47].

## 3.3.1 Detectors

**MVD**

The main task of the MVD [48,49] is to measure the dileptons and determine whether they come from the primary vertex. Another task is to reconstruct short-lived particles, such as $D$ mesons, based on their decay topologies. The lifetime of a $D$ meson is very short, in the low hundreds of micrometers divided by the speed of light, so MVD must be accurate to distinguish secondary vertexes; also high radiation hardness and a low material budget are needed to reduce rescattering. These conditions can be achieved using monolithic active pixel sensors (MAPS) called MIMOSIS with pixel sizes of $18 \times 18\,\mu m^2$ and $20 \times 40\,\mu m^2$. The pixel resolution is from 3.5 to $6\,\mu m$ and the resolution of the secondary peak (in the direction along the beam axis) is $50 - 100\,\mu m$. The detector consists of three layers of approximately $400\,\mu m$ silicon equivalent material (including the support structure). The time resolution should be less than $30\,\mu s$. The locations of these layers are 5, 10 and $20\,cm$ from the target position.

**STS**

The task of the STS [48, 49] detector is reconstruction of trajectories of individual particles and to measure their momenta (this can only be done with a magnetic field). It is made of eight layers located in a distance from 30 to $100\,cm$ from the vertex. Each layer consists of double-sided microstrip silicon sensors placed on a carbon fiber ladder. These ladders are positioned at $15°$ stereo angle (the angle between the beam axis and the horizontal axis). The momentum resolution should be approximately $\Delta p/p = 1\%$ and the material budget of the whole STS is less than $800\,\mu m$ silicon equivalent. A typical collision in a CBM experiment (Au+Au with energy $25\,AGeV$) causes 2 hits per $cm^2$ in the first layer and approximately ten times smaller hit density in the last layer. The hit resolution is planned to be $25\,\mu m$. Figure 3.5 shows a sketch of the detector along with the MVD and magnet.

51
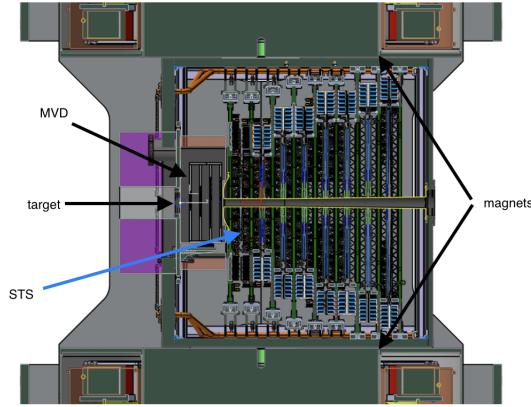
Figure 3.5: Sketch of the heart of the CBM detector - MVD and STS sub-detectors. From [50].

## RICH

Ring Imaging Cherenkov (RICH) [51] detectors are sensitive to Cherenkov radiation produced by charged particles (angle of the emission is inversely proportional to their velocity). This radiation is produced in the radiator and then it is focused by a Fresnel lens. If incident charged particles produced Cherenkov radiation then the detected photons will create a ring behind the lens. Its diameter is proportional to the angle of primary Cherenkov radiation and with this knowledge we can deduce the speed of a particle. In combination with STS (provides information about momentum), one can distinguish between the same charged particles with the same momentum for example negative pion - electron. CBM RICH [47] is designed for this purpose for momenta bellow $8\,GeV/c^2$. The main part of the detector is $1.7\,m$ long gas vessel filled with $CO_2$ as radiator followed by mirror lens with diameter of $3\,m$ and thickness of $3\,mm$. The last part is composed of two photodetectors planes. In a typical collision (already mentioned above) about 100 rings are produced (each consisting of approximately 20 photons). RICH can suppress pions background by a factor larger than 500. In Figure 3.6 one can see the sketch of the RICH detector, the ring produced in it and the ring radius dependence on momentum for electrons and pions. One can see that the threshold for the production of Cherenkov radiation for pions is around $5\,GeV/c^2$.

## MuCh

In the second setup, Muon Chamber (MuCh) [50] detector is used instead of RICH. The MuCh is designed to identify low-momentum muons from the hadronic background in the high multiplicity region. The idea of the detector is based on hadron absorber plates interleaved with detector plates. The absorbers are in five layers of thickness $60\,cm$, $20\,cm$, $20\,cm$, $30\,cm$ and $100\,cm$. The first one is made of a concrete and a graphite block placed in a magnetic field. The other layers are made of iron. The detectors are of the gaseous type and lay between these absorbers in triplets. To
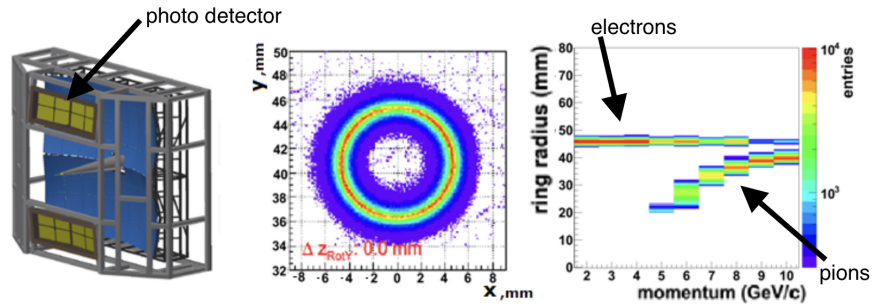
Figure 3.6: Left: a sketch of RICH detector, middle: ring observed in RICH, right: radius dependence on the momentum of electron and pion. From [52].

achieve high resolution, a highly granular gaseous detector based on GEM is used for the first two stations. For the third and fourth stations, single-section low-resitivity high-rate Resistive Plate Chambers (RPC) are used. The GEM [51] (gas electron multiplier) consists of a gas filed between the cathode and the anode. The incident radiation causes the production of electrons-ions pairs. The electrons migrate towards the anode, the ions in the opposite direction. In addition, foils with holes are embedded in them, which create a high electric field and ensure the multiplication of electrons drifting towards the anode. The anode is divided into separate pixels to achieve high precision. For the SIS100 beam, only three layers of shielding and three triplets of detectors are used.
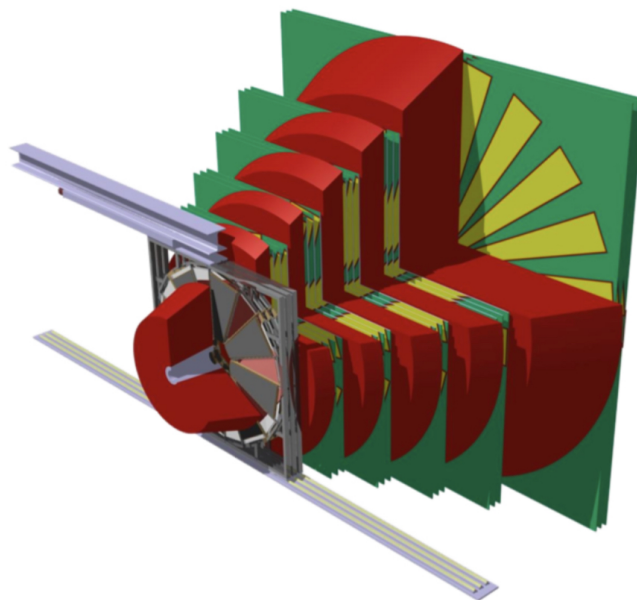


Figure 3.7: Sketch of Muon Chamber. From [53].

## TRD

Transition radiation detectors (TRD) are usually used to measure the gamma factor of the incident particles [51]. The main idea is that while the charged particle crossed the vacuum-dielectric boundary it creates a fast-moving electric dipole (a mirror image in the dielectric) which generates a field. When the particle reaches the boundary, the field disappears in a short time and X-rays are produced. The angle of emission is inversely proportional to the gamma factor of the particle. The particles drifting in the gas then ionize it, and at the same time the X-rays are absorbed and electron-ion pairs are formed. The signal is further amplified in the vicinity of the anode wires. Figure 3.8 shows the effect of the produced X-rays in the case of electrons. With multiple layers of wires, the exact location of the incident radiation can be determined. The TRD CBM detector [47, 50] is located behind the RICH or MuCh station (depending on the layout). Its purpose is to suppress pion background in the electron spectrum up to $1\,\mathrm{GeV}$. The TRD is thus an extension of the RICH detector for energies above $5\,\mathrm{GeV}$. Di-electrons produced from heavy vector mesons above $J/\Psi$ can be then measured efficiently. The pion suppression factor should reach $10-20$. Because of the typical energy losses in TRDs, they can also be used to measure nuclear fragments in the CBM hypernucleus program. The technology used for TRDs in CBM is a wire chamber filled with Xe or $CO_2$ gas with a radiator. There are two transition radiation production regions and they are $3.5\,\mathrm{mm}$ thin, the drift region is $5\,\mathrm{mm}$ thin. The TRD stations will be located at $5\,\mathrm{m}$, $7.2\,\mathrm{m}$ and $9.5\,\mathrm{m}$ from the target. The total active area of the detector is $1100\,\mathrm{m}^2$, one cell is $1\,\mathrm{cm}$. The Au+Au collision will achieve a particle density of $0.05\,\mathrm{cm}^{-2}$ and the position resolution should reach approximately $400\,\mu\mathrm{m}$. One TRD station, which consists of 4 layers will be used for the SIS100 campaign.
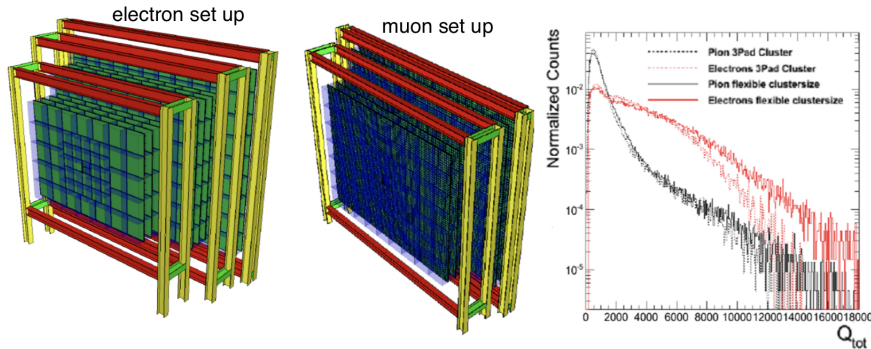


Figure 3.8: Left: a sketch of TRD in electron set up, Center: a sketch of TRD in muon set up, Right: pion and electron identification in TRD. From [52].

## TOF

The time-of-flight (TOF) detector will be used to identify hadrons by measuring their velocity. The CBM TOF consists of a resistive plate chamber (RPC). The RPC [54] technology is based on a gas chamber with two planar surfaces under high voltage. Ionization from the incoming radiation creates an avalanche that causes a

voltage drop across the readout strips. The TOF wall in the CBM [47,50] experiment will be placed at a distance of 10 m from the collision site and will cover 120 m². The size of one pad is 5 cm² and the position resolution is 0.6 cm. The emphasis in the development of the RPC is on high speed (expected hit density is approximately 25 kHz/cm²), low resistance, long-term stability and excellent time response. The time resolution is expected to be better than 90 ps. The TOF wall is only the second part of the timing system, the first part is the $T_0$ beam fragmentation counter (BFTC), which determines the start point of the timing.

**PSD**

The last CBM sub-detector is the Projectile Spectator [47] detector. It is located at the end of the beam tube and is used to determine the centrality of the primary collision and reaction plane by measuring the fragments of the produced nuclei. The PSD is designed as a fully compensated lead scintillation calorimeter with good energy resolution. The detector is constructed from $12 \times 9$ individual models with 60 layers of size 10 cm². Wavelength shifters are attached to the scintillator material to transfer the captured light to SiPM (Silicon PhotoMultipliers). The most important feature of PSDs is radiation resistance for the expected high absorbed doses.

However, as a result of the Russian aggression in Ukraine and the subsequent cessation of all cooperation with Russian institutions, some technologies, including PSDs, are unavailable. Therefore, the PSD will be replaced by another detector developed by our faculty. The detector will be based on the FWall of HADES experiment.

## 3.4   Experiment mini-CBM

Mini-CBM (mCBM) [55] is a testing version of the CBM detector. Its purpose is to test sub-detectors, to optimize various systems and develop software for future CBM detector. Setup of mCBM allows optimization of operation of the detector prototypes in high-rate nucleus-nucleus collisions, the data acquisition system and data transport to Green IT Cube. Also online tracking and event selection, offline data analysis and detectors control system can be studied. Thanks to mCBM, a full CBM detector will be available for physics running in a shorter time after completion. mCBM experiment is located in Target Hall in GSI in Cave-C (HTC). As you can see in Figure 3.9 cave is not very spacious. The beam pipe is shared with experiment R³B and it can be switched by HTD MU1 magnet to the required experiment. This beam pipe is connected to the SIS18 accelerator which can provide beams of different species as shown in Figure 3.10. The most important projectiles for this thesis are Ni at energy 1.93 AGeV and Au at energy 1.23 AGeV. SIS18 can deliver a beam with the same intensity as future SIS100.
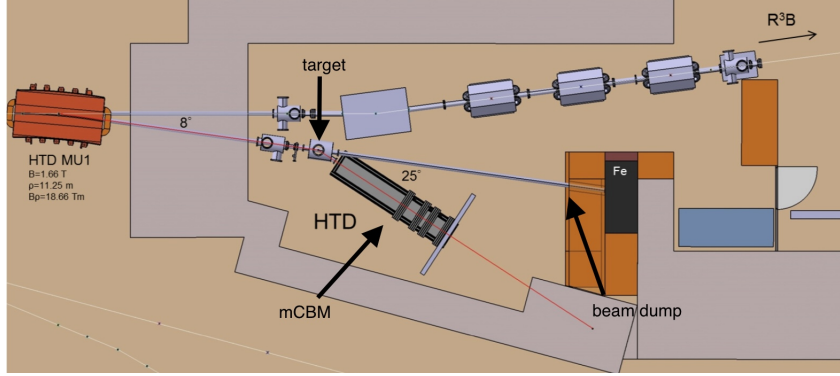
Figure 3.9: The cave of the mCBM experiment. From [55].

| projectile | T @ 10 Tm | T @ 18.66 Tm |
|:---:|:---:|:---:|
| p | 2.21 GeV | 4.74 GeV |
| Ca | 0.83 AGeV | 2.02 AGeV |
| Ni | 0.79 AGeV | 1.93 AGeV |
| Ag($46^+$) | 0.65 AGeV | 1.65 AGeV |
| Au($69^+$) | 0.45 AGeV | 1.24 AGeV |

Figure 3.10: Possible range of beams from accelerator SIS18. From [55].

### 3.4.1 Experimental setup

The mCBM detector is located at an angle of 25° from the incoming beam. Its length is about three meters and it is composed of prototypes of the future CBM detectors in order: mMVD, mSTS, mMUCH, mTRD, mTOF, and mRICH. The only exception is the mPSD detector which is located in the beam direction. After them, the beam is terminated in beam dump (7 m from the interaction point) consisting of six 12 cm long iron plates covered by 80 cm thick concrete block. In the mCBM experiment a magnetic field is not used therefore momentum determination can be done only by using the time of flight detector. The experimental setup is not final and it is being changed to test detectors and also to reach significant statistics when detecting Λ hyperons. The angle at which mCBM is able to detect particles is from 13° to 37° measured from the beam axis in the horizontal direction. The covered vertical angular range is ±12°. Distances from the vertex of the individual detectors can be seen in Figure 3.11.

The mSTS consist of two small prototype stations with $2 \times 2$ (the first layer) and $3 \times 3$ (the second layer) modules consisting of half-ladders. A total of 13 modules are used with a size of $6 \times 6$ cm$^2$ and 1024 pixels on each sensor side. The location is 28 cm and 42 cm from the interaction point for mSTS 0 and mSTS 1 respectively.

The mMUCH is made in a trapezoidal shape. Compared to MUCH detectors in the CBM, there is no large shielding. The mMUCH is composed only of GEM modules mounted on 10 mm aluminium plate. Each of them has 2304 pads. In mCBM, up to three mMUCH detectors can be inserted. The position of the first layer is 80 cm
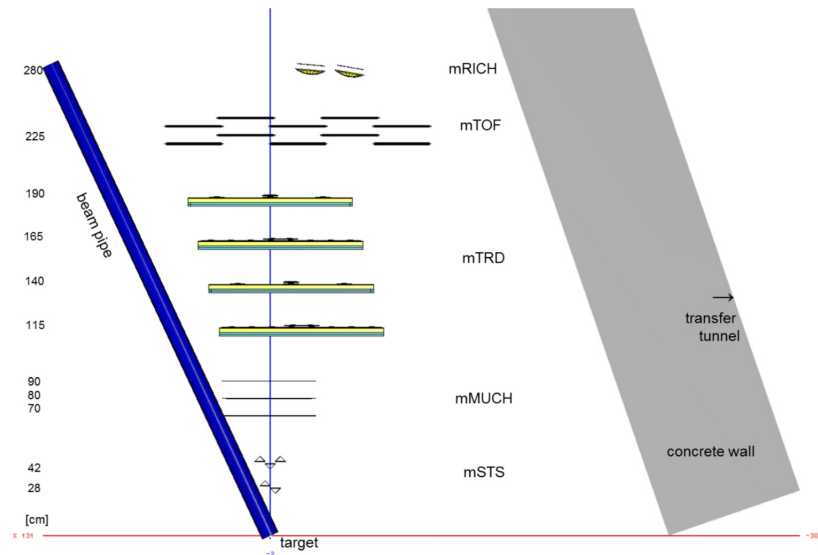
Figure 3.11: Sketch on mCBM detectors. From [55].

from the interaction point and the next stations are separated by $10 - 20\,\mathrm{cm}$.

The TRD1D modules are placed in $190\,\mathrm{cm}$ (last station). One station is $95 \times 95\,\mathrm{cm}^2$ large and contains 768 pads. The layer consists of 6 rows of 128 pads, every next station is rotated radially by $90°$. A maximum of four-layers can be placed in the setup. The TRD2D module is placed in front of them. The TRD2D is two sided and has the same granularity of pads in both directions.

The mTOF is the last detector of mCBM in geometries for years 2021 and 2022. It is located $225\,\mathrm{cm}$ from vertex. The mTOF is divided into modules composed of five MRPCs (type MRPC3a) with readout systems. The total active area of mTOF is $150 \times 125\,\mathrm{cm}^2$ and has 1600 readout channels. The mTOF is connected to $T_0$ counter which provides information about starting of measuring time. The $T_0$ is composed of a single plate $20 \times 20\,\mathrm{mm}$ electronic grade polycrystalline diamond plates of $0.3\,\mathrm{mm}$ thickness placed in the beam pipe. The design goal for the $T_0$ counter time resolution is $50\,\mathrm{ps}$ for reaching $80\,\mathrm{ps}$ resolution of the whole TOF system.

## Geometry 2022

In Figure 3.12 you can see one of the geometries for 2022 data taking run - 2022_02. This geometry includes all subdetectors, other possible geometries are: 2022_03 - removed one GEM station, 2022_04 - no GEM stations, 2022_05 - no GEM and TRD2D stations, 2022_06 - only mSTS and mTOF stations. In Table 3.2 differences between setups are shown.

|          | mSTS | 1st GEM | 2nd GEM | TRD2D | TRD1D | mTOF |
|----------|------|---------|---------|-------|-------|------|
| 2022_02  | x    | x       | x       | x     | x     | x    |
| 2022_03  | x    |         | x       | x     | x     | x    |
| 2022_04  | x    |         |         | x     | x     | x    |
| 2022_05  | x    |         |         |       | x     | x    |
| 2022_06  | x    |         |         |       |       | x    |

Table 3.2: Comparison of different 2022 geometries
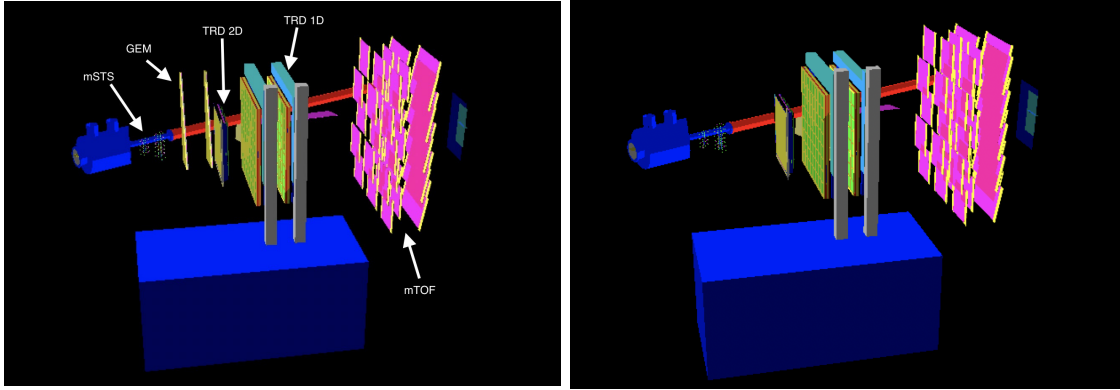


Figure 3.12: The geometry of the mCBM with all subdetector systems 2022_02 (left) and geometry without two GEM foils 2022_04 (right).

## Geometry 2021

In Figure 3.13 you can see a sketch of the mCBM geometry 2021_07 in comparison with 2022 geometries in the 2021_07 there are different positions of mTRDs and mTOF, also GEM foils are missing.

## Real geometry

The geometries mentioned above are ideal ones, not the real ones used for data taking. The real geometry 2022_05_23_nickel used for data campaign for in May (Ni+Ni at 1.93 AGeV) and in June (Au+Au at 1.24 AGeV) is in Figure 3.14. The difference between this geometry and geometry 2022_04 is in the mTOF modules. In the real geometry approximately one third of the mTOF is missing and thus it has smaller a acceptance.
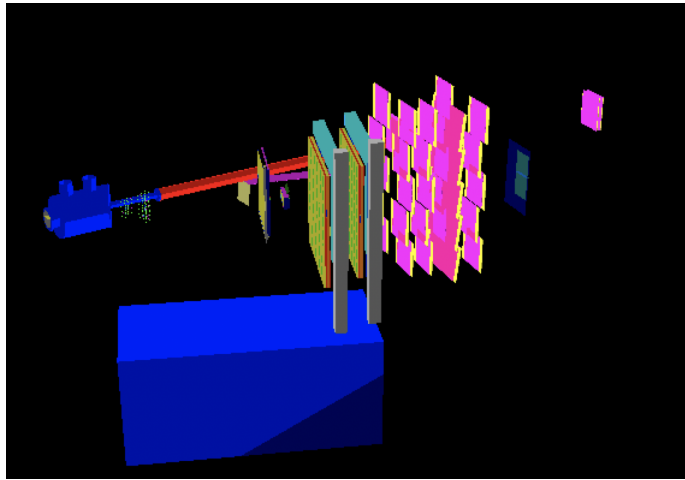
Figure 3.13: The geometry of mCBM 2021_07.
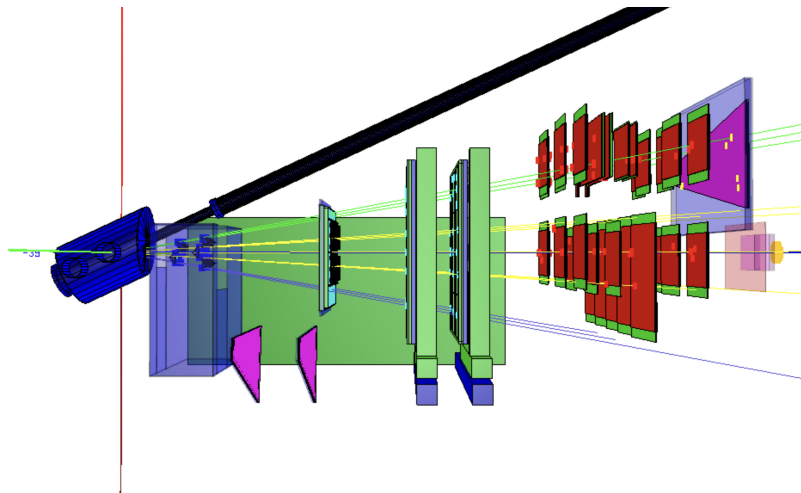


Figure 3.14: The geometry of mCBM 2022_05_23_nickel.

# Chapter 4

# Λ simulations

A large part of my own contribution to the mCBM is the simulation and reconstruction of Λ hyperons. As already mentioned, the detection of Λ hyperons is one of the physics benchmarks of the mCBM experiment.

Simulations are important for estimating the expected signal and understanding the influence of selection criteria and their optimization. In this work, simulations are performed for systems of O+Ni with energy $2\,\mathrm{AGeV}$, Ni+Ni with energy $1.93\,\mathrm{AGeV}$ and Au+Au with energy $1.24\,\mathrm{AGeV}$ (these are the maximum energies provided by SIS18, as given in 3.10). First, pure Λ samples with thermal spectrum are generated to verify that all systems work well. Then, the O+Ni system is simulated to obtain results with a smaller background since O+Ni is much smaller compared to the Au+Au system. The atomic numbers are 28 for nickel, 16 for oxygen and 79 for gold. After this setup, different geometries and selection criteria are studied. The Au+Au and Ni+Ni collisions are studied to optimize the setup for real data analysis. Based on these simulations, it was actually decided in the mCBM collaboration which geometry should be used for the data collection campaign.

Λ is composed of three quarks - u, d and s [36]. Mass of a Λ is $1.115\,\mathrm{GeV/c^2}$ and its mean lifetime is $2.6{\cdot}10^{-10}\,\mathrm{s}^{-1}$. Λ hyperon decays into a proton and negative pion with a branching ratio of 67% or into a neutron and neutral pion with a branching ratio 33%. In the mCBM, the Λ candidates are detected through the proton-pion channel. Using these properties one can make a "toy model" for Λ simulation to get a better idea about the decay geometry. The toy model uses root class `TGenPhaseSpace` in which Λ hyperon properties are introduced. As it will be discussed below in the reaction of Ni+Ni at $1.93\,\mathrm{AGeV}$ produced Λ hyperons have momenta distribution maximum between 1 and $2\,\mathrm{GeV/c}$. Therefore simulated Λ were simulated in this energy range and the results can be seen in Figure 4.1. Λ with higher energy have longer decay lengths and smaller opening angles.

In Figure 4.2 you can see the same plot for Λ with momentum $0.5\,\mathrm{GeV/c}$ . For this energy of Λ, the mean opening angle is about two times larger in comparison with $1\,\mathrm{GeV/c}$ Λ. In some events, the pions are produced backwards. Also, these Λ have short decay length. Thus for such decay geometries we are not able to reconstruct Λ in the mCBM due to its geometry (the detector is only in a positive direction
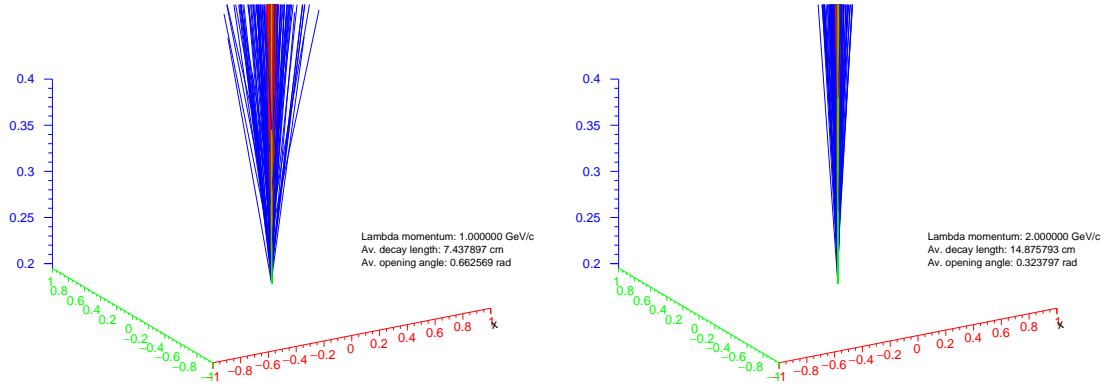
Figure 4.1: Λ decay simulation in the "toy model", on the left there are simulated Λ with momentum 1 GeV/c and on the right with momentum 2 GeV/c. The green line is the direction of the Λ, produced protons are red and pions are blue. In these plots, one hundred events are simulated. All axis are in meters.

within a limited angle). The "toy model" is working well for getting an intuition for working with Λ, nevertheless, cannot be used any further.
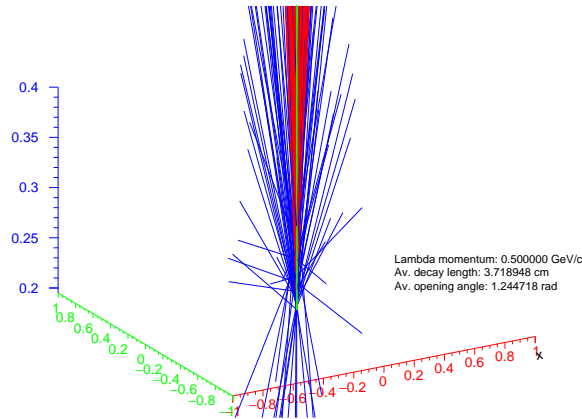


Figure 4.2: Λ decay simulation in the "toy model", on the left are simulated Λ with momentum 0.5 GeV/c. The green line is direction of the Λ, produced protons are red and pions are blue. In the figure are simulated 100 events. All axis are in meters.

## 4.1 Simulation setup

In this work, the GEANT [56] (GEometry ANd Tracking) software was used to describe the propagation of particles through matter using Monte Carlo methods. Two versions of GEANT are currently available, GEANT3 and GEANT4. GEANT3 is used in this work.

Most of the work has been done in the cbmroot software framework, which is a customized version of the original root invented at CERN in 1997 [57]. The use of cbmroot is very broad, it can be used for simulations, reconstructions and data analysis. The first version of the software was released in 2004.

The simulation of $\Lambda$ baryons is divided into several steps. The first part is the simulation of events using UrQMD, which is described above. The number of events generated was chosen to be 100M (the number of real data events should be about ten times larger). The second option instead of UrQMD is to simulate pure $\Lambda$ baryons. In this case, particles are generated with a thermal shape distribution. The next step is a transport code in which the produced particles are transported through the detectors in UrQMD (macro: `mcbm_transport.C`). Here, GEANT3 is used to simulate the interactions between the produced particles and the detector material. The next stage of the process is to digitize the detector response to the particles (macro `mcbm_digi.C`). This means that the information about the deposited energy in the active volume of the detectors is used to simulate the electronic output. After this process, the induced signals need to be processed similarly to real data. Therefore, event reconstruction (`mcbm_reco_event.C`) is performed. The reconstruction can be done in two possible ways. The first is the event base, in this approach the events are separated and reconstructed one by one (`mcbm_reco.C`). The second approach is time-based, which means that there is no time separation between events and events are reconstructed continuously. The data is only split into time periods containing a large number of events. The second option is more realistic because the future CBM detector will be read out in this way. Despite omitting the effect of overlapping events, event-based reconstruction is a useful tool for getting a better idea of the effectiveness of $\Lambda$ detection (especially for runs with low interaction rates) and for deciding what setup should be used for data acquisition. Therefore, an approach based on event-based simulations is used for $\Lambda$ reconstruction. The last part of the simulations is hadron analysis (`mcbm_hadron_analysis.C`). In this phase, the tracks are reconstructed and the $\Lambda$ search algorithm is processed. The above scripts are sent using `sendJobArrayScript.sh` to the Virgo computer farm working with the Slurm cluster manager. The simulated 100 million events are divided into 1000 computational jobs, each containing 100000 events. Figure 4.3 shows the flow diagram of the simulations.
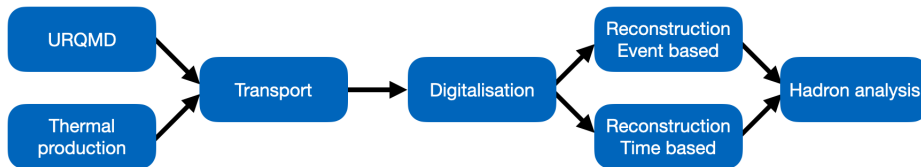


Figure 4.3: The flow diagram of the $\Lambda$ simulations.

## 4.2 Tracking in mCBM

The tracking system of the mCBM is based on the `CbmHadronAnalysis.cxx` which is part of the cbmroot installation. I modified this macro from its default behavior so that it saves information about the reconstructed vertexes into ROOT `TNtuple` structure. This enables making different cuts afterwards with only single pass of the script on the data hence significantly speeding up the whole study.

Tracking in the mCBM uses only hits in the mSTS, mTOF and mTRD detectors. All additional detectors are not implemented in the tracking thus they are effectively dead material for this study. The logical conclusion is that the best results should be provided by the geometries without GEM detectors. That is true, however, these detectors have to also be tested and therefore one has to balance this need against the efficiency of $\Lambda$ reconstruction. The main part of the tracking system is provided by mSTS and mTOF hits, mTRD hits are only associated with the tracks as a possible additional track confirmation. The $\Lambda$ reconstruction is based on the detection of the daughter proton and pion. There are two types of cuts. The first ones are associated with finding candidates for proton and pion. The second ones are used to select on the mother $\Lambda$ hyperon decay geometry. All of them will be discussed below.

Firstly, `CbmHadronAnalysis.cxx` macro is trying to find primary particle tracks. It scans all mTOF hits and makes a line from the primary vertex point to the mTOF hit. Then mSTS hits are scanned and if any has a smaller distance from this line then $d_1$ the analysis continues with the finding of a second mSTS hit and if the distance of the second hit from the line mSTS-mTOF is smaller than $d_2$ a new primary track is made out of these two mSTS hits. This track could be also confirmed by mTRD stations. mTRD hit is associated with the track only when it has a smaller distance from the track than the value of $TRDdist$ cut and the number of these hits is higher than the cut value ($TRDmult$).

In the next step, data are scanned for secondary proton candidates. These proton candidates are selected from the pool of the primary tracks with an additional conditions. The line made from two mSTS points associated to the track has to have a larger distance from the vertex than $d_{proton}$. The idea here is based on the fact that the proton carries away most of the momentum of the primary hyperon and hence the proton could be selected from a set of tracks that point close to the primary vertex. Naturally, as can also be seen from the toy model simulations, this approach will not work so well for $\Lambda$ with low momenta.

The pion candidates are produced from points which do not pass condition $d_1$ in the primary track reconstruction. The line from mTOF and mSTS hits are made and again the mSTS is scanned for close hits. If there is a second hit in a distance smaller than $d_{pion}$ from the mTOF-mSTS line, the track is flagged as pion candidate. Track is then recalculated using mSTS points. In Figure 4.4 there is a scheme of tracking in the mCBM (upper figure) and a flow diagram of the tracking (bottom figure).

Distributions of the variables described above are presented in the Figure 4.5 from simulations of Ni+Ni collisions at 1.93 AGeV in the geometry tagged as 2022_05_23.

Typical set of values of the selection criteria which were used for finding the proton and pion candidates is shown in Table 4.1.

In addition to using the information from mSTS and mTOF, the primary and secondary tracks can also have associated mTRD hits. That means it is possible to require for the track to be taken as proton or pion candidate to have a number of associated mTRD hits larger than $TRDmult$ each with a distance smaller than $TRDdist$. From the simulations of the pure $\Lambda$ it was possible to observe that most of the signal is typically found with $TRDdist$ smaller than $10\,\text{cm}$ for both primary
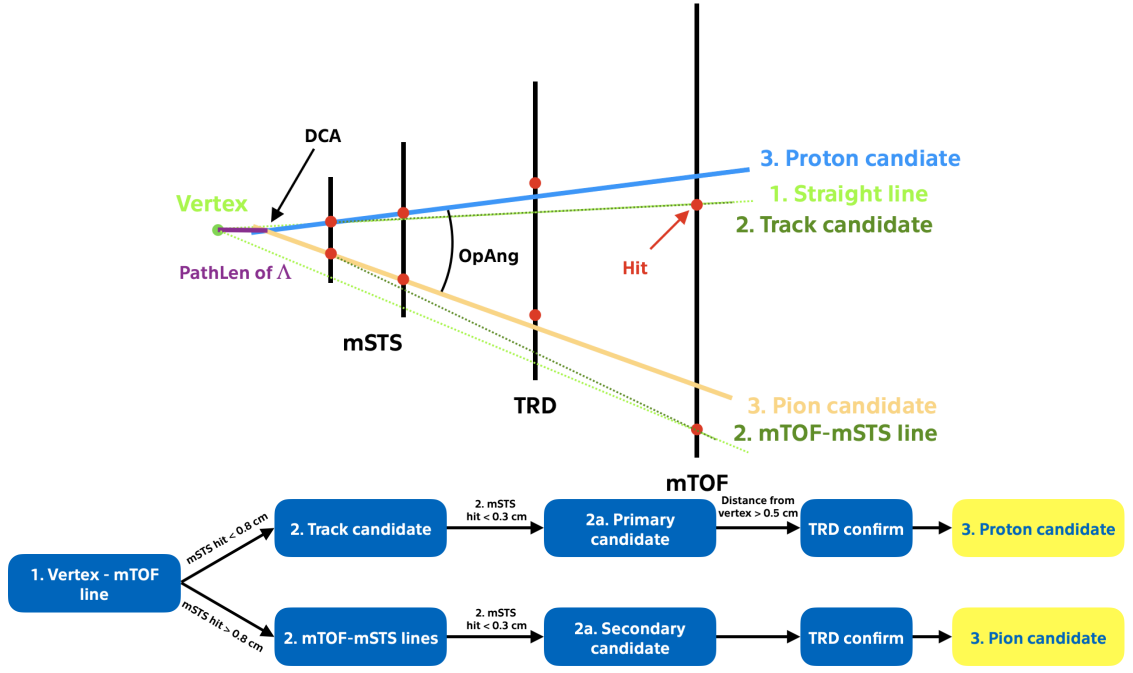
Figure 4.4: Upper figure: Scheme of the mCBM tracking. Bottom figure: Flow diagram of the tracking.
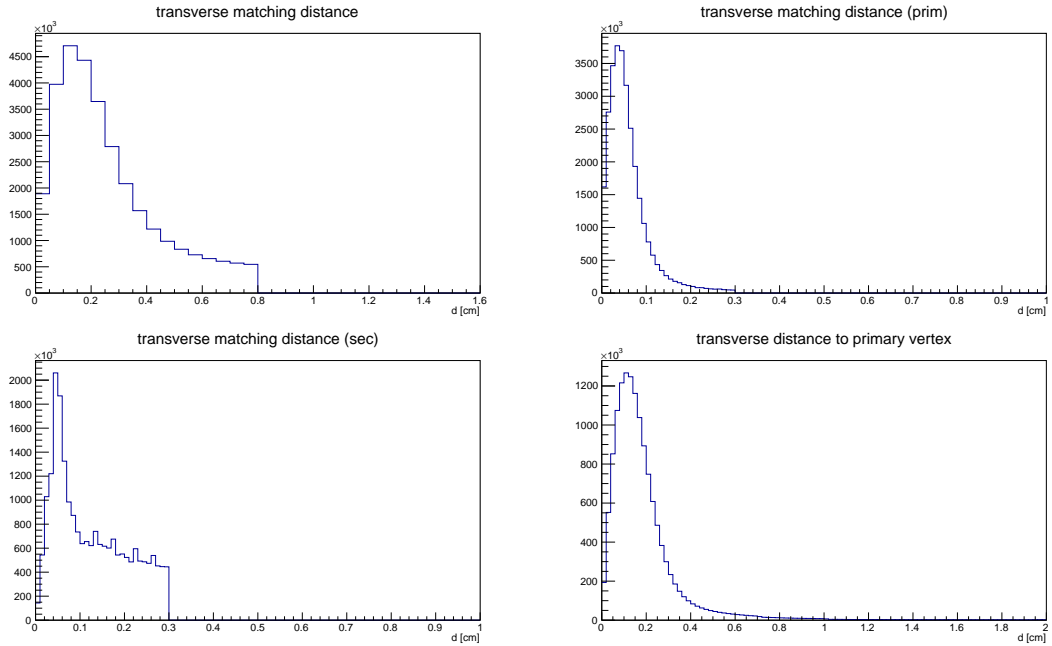


Figure 4.5: Distributions of the $d_1$ (top left), $d_2$ (top right), $d_{pion}$ (bottom left), $d_{proton}$ (bottom right) for Ni+Ni collision at energy $1.93\,\mathrm{AGeV}$ in geometry 2022_05_23.

and secondary candidates. This can be seen in Figure 4.6.

Although the distance of $TRDdist < 10\,\mathrm{cm}$ could be used for confirmation of proton and pion candidates. It is much below the expected mTRD resolution.

|        | [cm] |
|:------:|:----:|
| $d_1$ | 0.8 |
| $d_2$ | 0.3 |
| $d_{proton}$ | 0.5 |
| $d_{pion}$ | 0.3 |
| $TRDdist$ | 10 |

Table 4.1: Values of the cuts for accepting pion and proton candidates.
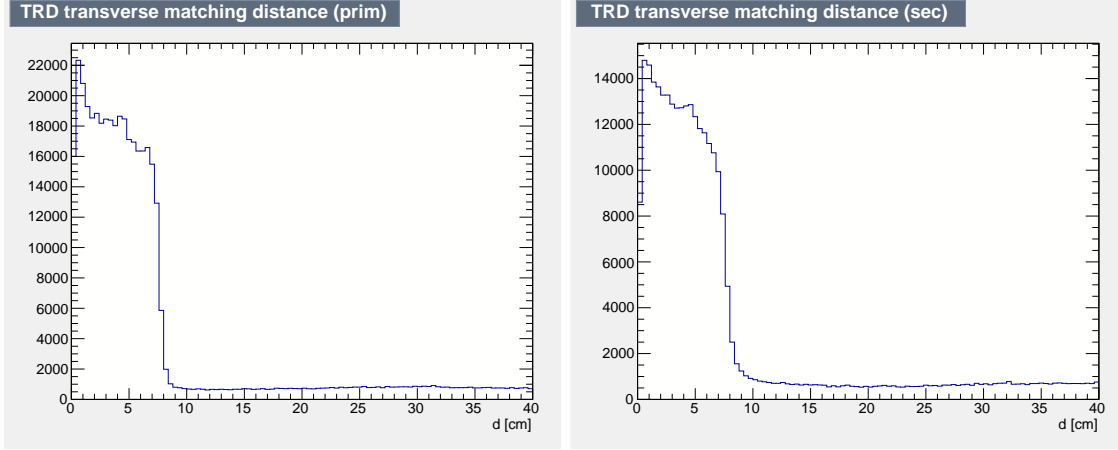


Figure 4.6: Distributions of distance ($TRDdist$) of mTRD hits from primary (left) and secondary (right) tracks from pure $\Lambda$ simulations.

As the name TRD1D suggests, TRD1D test module is composed of a long pad with high resolution in one direction. In the second direction, the resolution is low due to the width of these pads (hit position is taken at the center of the pad). Therefore for signal extraction $TRDdist$ must be computed from the direction along the high granularity of the mTRD module. For example, the x-direction of TRD1D (the first layer of the TRD1D has a good resolution in the x-direction). Hence the original `CbmHadronAnalysis.cxx` (which assumed double-sided module) was updated and $TRDdist$ was computed only from the components which have high resolution. The first layer of the TRD1D is used for the x-direction and the second is used for the y-direction. In Figure 4.7 there are $TRDdist$ for primary and secondary track candidates from pure $\Lambda$ simulations. On the x-axis are shown distances in the direction with high resolution and on the y-axis distances along low resolution direction. Based on this mTRD cuts were chosen. Typically $TRDdist < 0.4$ cm are required and additional $TRDdist\_sec < 8$ cm which is used to make sure that the hit is in the nearest pad. Module called TRD2D was also added for validation of the pion and proton candidates. The difference between TRD1D and TRD2D is in that TRD2D is double sided and hence has a good resolution in both directions and therefore $TRDdist$ for TRD2D is taken as the maximum of the $TRDdist$ in the x-direction and y-direction and for validation is required to have this distance smaller than $TRDdist < 0.4$ cm.

When one has proton and pions candidates then they can be combined to form $\Lambda$ candidates. Several selection criteria (cuts) are used in order to separate real signal
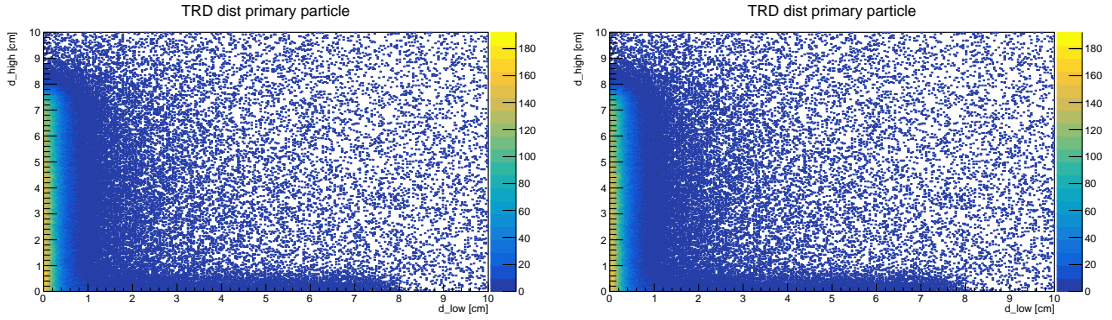
Figure 4.7: Two-dimensional graph of the distances between tracks and mTRD hits from TRD1D modules for primary particles (left) and secondary (right) particles. On the x-axis are distances in the along direction with high resolution of the TRD1D and on the y are distances along the worse direction. Results were obtained from pure $\Lambda$ simulations in geometry 2021_07 .

|  | Initial values | New values |
|---|---|---|
| max $DCA$ | 0.1 cm | 0.7 cm |
| min $PathLen$ | 5 cm | 1 cm |
| max $PathLen$ | 25 cm | 25 cm |
| min $OpAng$ | 0.2 rad | 0.2 rad |

Table 4.2: Values of the cuts for the $\Lambda$ candidates for filling into the `TNtuple`.

from combinatorial background. The first one is the distance of the closest approach ($DCA$). This is a smallest distance between the daughter tracks of the $\Lambda$ candidate. Another variable is the opening angle ($OpAng$) between the two daughter tracks. The difference between the position of the $DCA$ and vertex position (which for the simulations is at the beginning of the coordinate system) is the path length (decay length) of the $\Lambda$ candidate ($PathLen$). Last, but the most important variable, is the invariant mass of the $\Lambda$ candidate ($Minv$) which is calculated from the four-momenta of the daughter tracks using the proton and pion assumption. The cuts on all of the mentioned variables were opened larger when filled into `TNtuple`. Initial values of the cuts are presented in Table 4.2. Some of the cuts are at their maximum possible value. For example, the maximum $PathLen$ of the $\Lambda$ is 25 cm because at this distance is the first layer of the mSTS detector.

The background is created using the Mixed-Event background. In this technique, pions and protons from different events are mixed, and since there is no correlation between them, these candidates form a background.

Additionally, information about matching of Monte Carlo (MC) tracks and reconstructed tracks was added into `TNtuple`. In other words, we would like to know how the response of the detector looks when $\Lambda$ is produced in the nucleus-nucleus collision. This is important when one would like to use advanced techniques, such as machine learning to select reconstructed $\Lambda$. Input from pure $\Lambda$ signal is needed as a training dataset.

This matching can be done in multiple ways. I chose following. We have a $\Lambda$ candidate and this candidate is flagged as real signal input when $\Lambda$ is produced in the

acceptance of the detector (in angles ±12°). The reconstructed Λ is matched to the MC mother if the momentum of the MC Λ and reconstructed Λ are very similar (the difference is smaller than 0.05 GeV) and momentum of the MC pion and reconstructed pion is very similar. This approach has one significant drawback. The MC tracks and the reconstructed tracks are not connected by their position. This can cause spurious results in the reconstruction of the MC Λ.

## 4.3   Primary Λ simulations
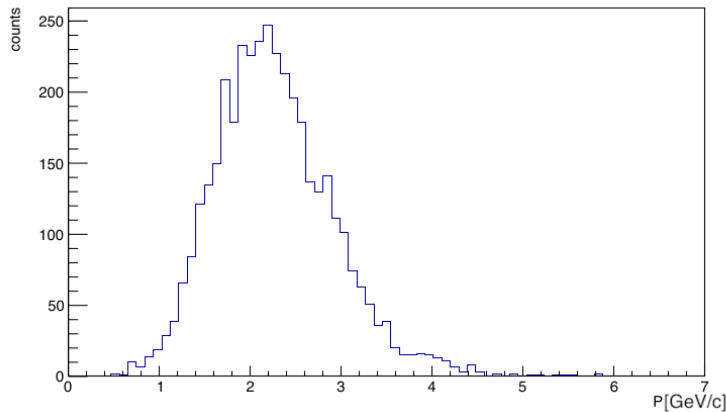


Figure 4.8: Reconstructed momentum spectrum of the simulated Λ.

For first simulations only pure set of Λ was chosen with thermal shape of the spectrum. The reconstruction was done in the same way as in the diagram in Figure 4.3. These simulations were made for detector geometry 2021_07 which is slightly different in comparison with 2022 geometries. The reconstructed momentum spectrum of the simulated Λ can be seen in Figure 4.8. Clearly we are not able to reconstruct Λ with smaller momentum than $1$ GeV/c due to the large opening of decay angle and small decay length. This was expected based on the simple toy model simulations.

The cuts used previously are in Table 4.2 (left column) and corresponding plots of these variables are in Figure 4.9. Cuts for the $DCA$ and $PathLen$ look reasonable however opening angle behaves the opposite of what we would expect. Such a high angle is impossible to measure with mCBM (it covers angles ±12° and this angle is almost in opposite direction). The problem was in the order of mSTS layers when finding proton candidates (they were switched in code and therefore proton momentum was opposite).

All the cuts applied on the `Ntuple` for Λ reconstruction are shown in Table 4.3. These values are also used for other systems.

The last plot (Figure 4.10) in this section is the invariant mass of the pure Λ sample. As could be expected, we can only see the signal from Λ and the background is practically zero. A decrease in the number of reconstructed Λ is caused by a more strict cut on the opening angle.

|  | Cut value |
|---|---|
| max $DCA$ | $0.1\,\mathrm{cm}$ |
| min $PathLen$ | $5\,\mathrm{cm}$ |
| max $PathLen$ | $20\,\mathrm{cm}$ |
| min $OpAng$ | $0.19\,\mathrm{rad}$ |
| min $OpAng$ | $0.54\,\mathrm{rad}$ |
| min $MMom$ | $0.4\,\mathrm{GeV/c}$ |

Table 4.3: Values of the cuts applied on the `Ntuple` for $\Lambda$ reconstruction.
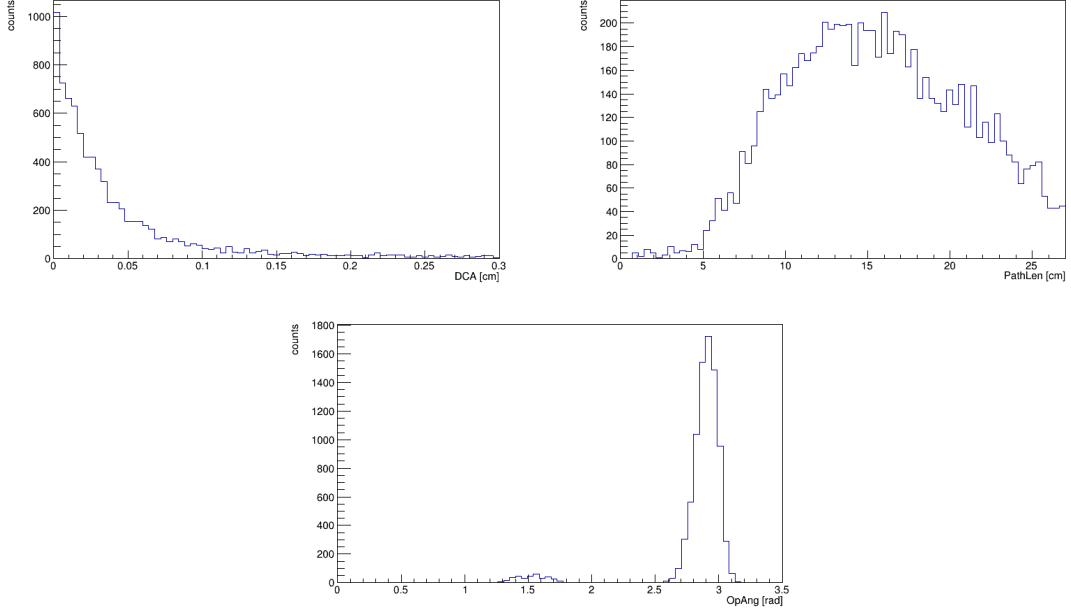


Figure 4.9: Distributions of the opening angle, distance of the closest approach and path length of the $\Lambda$ with thermally produced $\Lambda$ and geometry 2021_07 and with no additional cuts on the `Ntuple`.
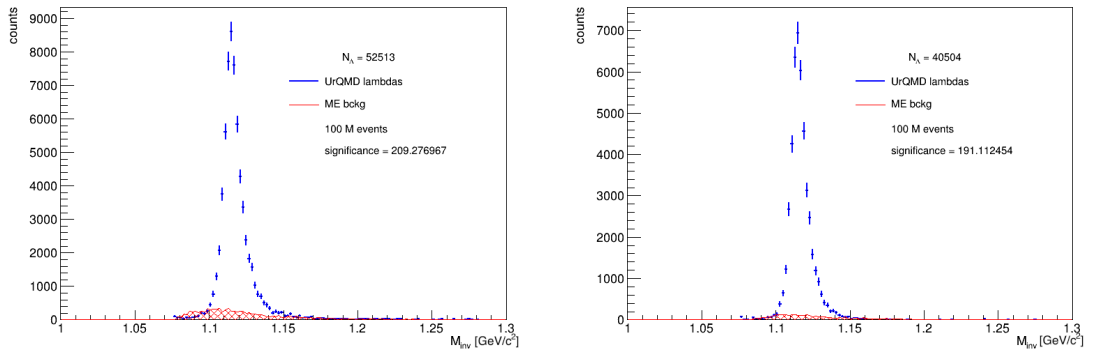


Figure 4.10: Invariant mass distribution of the reconstructed pure $\Lambda$ sample in geometry 2021_07 with older cuts (left) and new cut (right).

69

## 4.4 Λ simulation in the O+Ni

As a second simulation setup system of the O+Ni at 2 AGeV was chosen. These simulations were made for all (five) 2022 detector setups (see Table 3.2) and also for one 2021 setup. In Figure 4.11 invariant mass spectra of the reconstructed Λ candidates for all these detector geometries are shown. The geometry 2021_07 (full geometry used for data campaign in 2021) has the smallest number of reconstructed Λ and the significance of the signal is also the smallest. Let's focus on the 2022 geometries. The number of found Λ increases when removing detectors. But even in full mCBM geometry (2022_02) the number of reconstructed Λ candidates is relatively high and significance is also sufficient. The largest increase of the reconstructed Λ yield is between geometries 03 and 04 where the second layer of the GEM is removed. Geometries with one (02) and two (03) GEM layer show very similar results in significance. Therefore the second layer does not affect much Λ reconstruction efficiency. The effect of removing the two layers of the TRD1D (05 → 06) is suspicious as one would expect that number of the Λ should increase but the effect is the opposite. In all 2022 setups signal has enough significance and therefore can be used for Λ reconstruction. Also, it is not necessary to use additional mTRD hits to improve the signal.

## 4.5 Λ simulation in the Ni+Ni

Simulations of the Ni+Ni collision were made at energy of 1.93 AGeV. In comparison with O+Ni system, there is an increase in the combinatorial background. In Figure 4.12 the invariant mass distributions for the different detector geometries are presented. As shown, in all of the geometries significance of the Λ signal is higher than 5σ and therefore Λ are detectable in all geometries. The same effect in comparison with O+Ni collisions can be observed. The highest background is in full geometry (2022_02). When one GEM foil is removed the signal increases, however this increase is small in comparison with the increase when the second GEM foil is removed. The last switch between geometries 2022_04 to 2022_05 causes an increase in the number of Λ, but the background also increases, thus the significance of the signal decreases overall.

Figure 4.13 shows a comparison of the signal after background subtraction for different geometries. As was already mentioned, the number of reconstructed Λ is higher with fewer detectors with GEM foils having the largest effect.

## 4.6 Λ simulation in the Au+Au

The last simulation setup was Au+Au collisions at 1.24 AGeV. The used geometries are 02, 04 and 05. It should be noted again that the energies of the collisions are smaller than in previous cases and actually under the Λ production threshold in hadronic collisions. Therefore we expected that number of reconstructed Λ will be
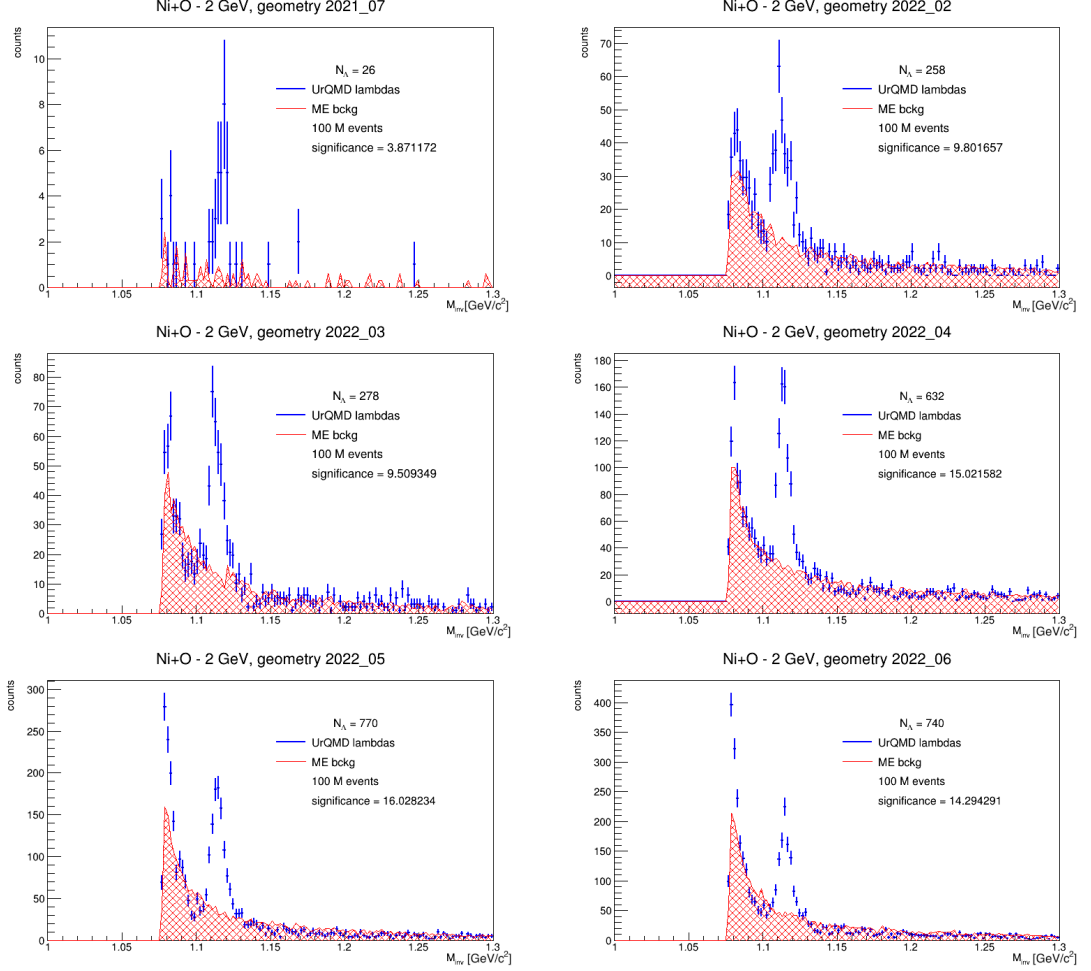
Figure 4.11: Invariant mass spectra for different mCBM detector geometries. Used cuts are in Table 4.3

significantly smaller. At the same time, the background should increase because we have to deal with a larger collision system. Figure 4.14 shows an example of the invariant mass distribution when the analysis is done similarly as in the previous systems at higher energy. As you can see the signal is very small and also significance is about 0.4. Basically, the $\Lambda$ hyperon is not visible. Plots for other geometries are not shown since the situation is very similar. To solve this issue three methods were used. The first one is additional mTRD hits for accepting pions and protons candidates, the second is mTOF multiplicities and the third is an application of machine learning methods (TMVA).

### 4.6.1 mTRD

mTRD hits were used as it was described during the explanation the tracking algorithm. For validation of the proton and pion candidates mTRD hits were required to have smaller distance than $TRDdist < 0.4$ cm from track candidates. In the analysis, tracks with one, two and three mTRD hits were considered. In Figure 4.15 one can see results for geometry 2022_05 with the addition of one mTRD hit (left) and
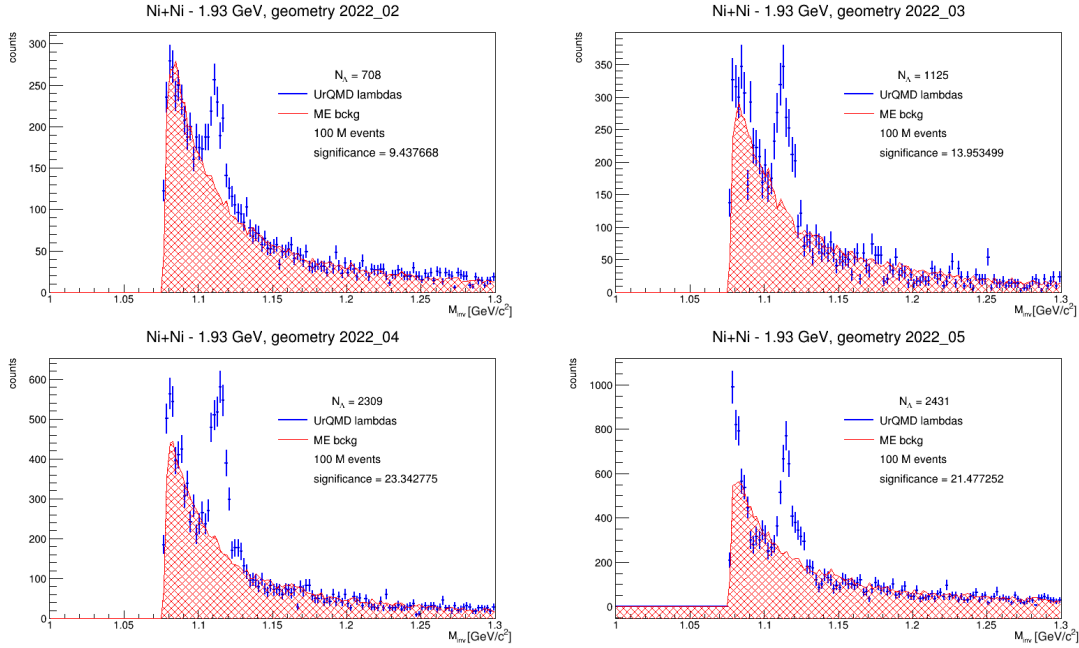
Figure 4.12: Invariant mass spectrum in Ni+Ni collisions at 1.93 AGeV for different geometries. Cuts are in Table 4.3 without additional TRD hits.
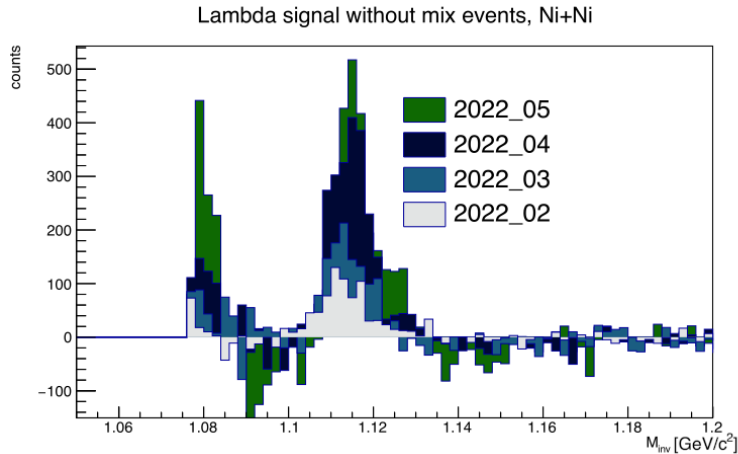


Figure 4.13: Comparison of the Λ yields in different geometries.

2 mTRD hits (right). As can be seen the significance substantially increase when 2 mTRD hits are used. The use of 1 mTRD hit also increases significance, but it does not reduce background as strongly as when 2 hits are required.

In geometry 2022_05 there are only two TRD1D layers while in other presented geometries there is also TRD2D installed. Therefore when one requires at least two mTRD hits these hits can come from three stations instead of two. As you can see in Figure 4.16 there is a visible effect of turning on and off the TRD2D in geometry 2022_04. In both variants, the signal has quite good significance but when TRD2D is used signal has a significance greater than five. The requirement of three mTRD hits was also tested, but this cut is too restrictive and reduces significance.
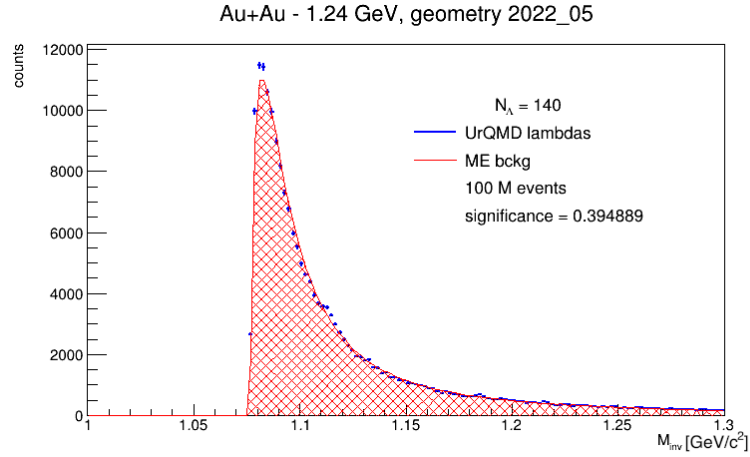
Figure 4.14: Reconstructed invariant mass for geometry 2022_05 in Au+Au collisions at 1.24 AGeV.
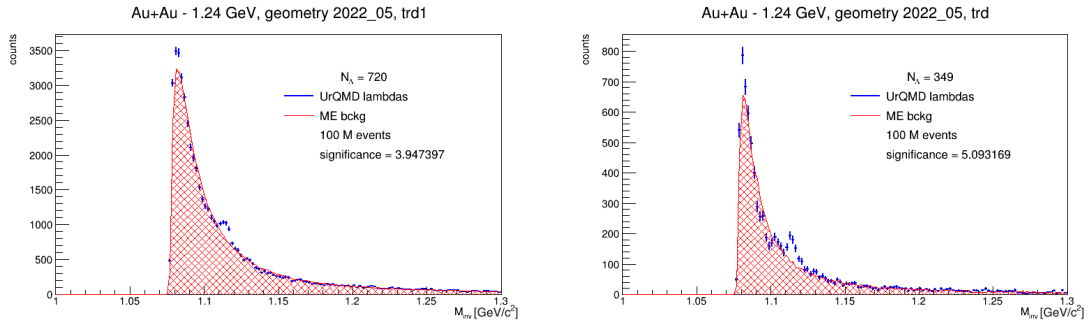


Figure 4.15: Mass spectrum of the Au+Au collisions at 1.24 AGeV for geometry 2022_05 when using additional one mTRD hit (left) and two mTRD hits (right).
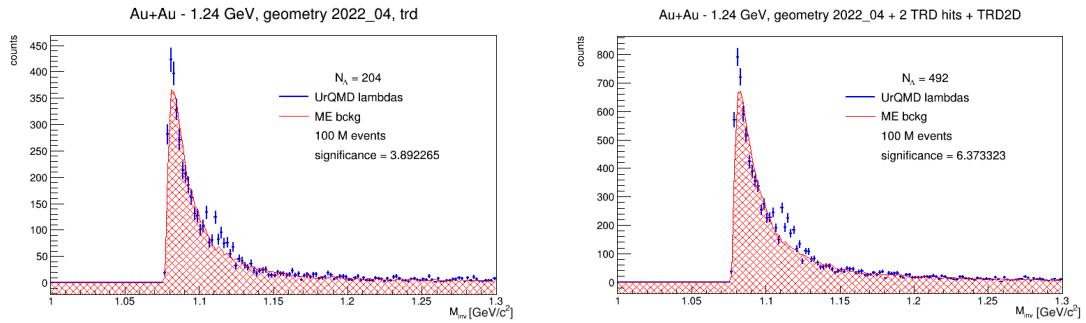


Figure 4.16: Mass spectrum of in Au+Au collisions at 1.24 AGeV for geometry 2022_04 using additional two mTRD hits and turning off TRD2D (left) and turn on TRD2D (right) module.

In Figure 4.17 you can see results for geometry 2022_02 (full mCBM geometry) with two mTRD hits. Here significance is too small and therefore this geometry is not suitable for $\Lambda$ detection even when mTRD hits are used.
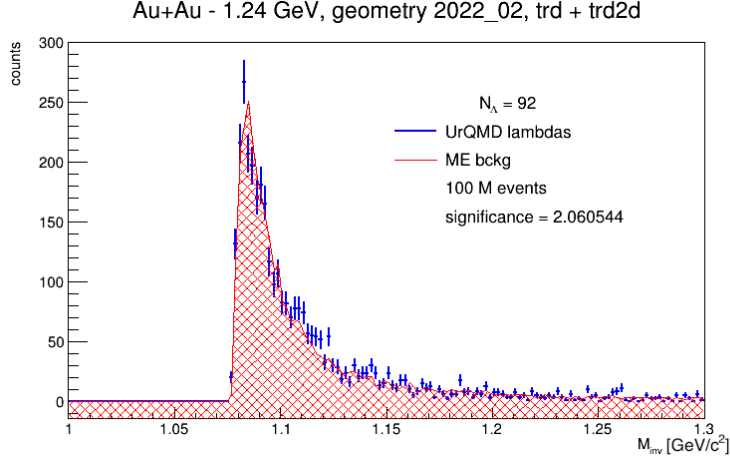
Figure 4.17: Mass spectrum in the Au+Au collisions at $1.24\,\mathrm{AGeV}$ for geometry 2022_02 with using an additional one mTRD hit (left) and two mTRD hits (right).

## 4.6.2 Multiplicity in mTOF

Another possible effect that can influence the $\Lambda$ signal may come from the multiplicity in the mTOF. This is important because when one finds out that $\Lambda$ is more likely reconstructed for example in events with higher multiplicities then real data can be triggered to this region. However, there are two effects which work against each other. When we have an event with high multiplicity then we can assume that we have a more central collision and $\Lambda$ production cross-section is higher. On the other hand, in events with large multiplicity the $\Lambda$ finding algorithm has much more hits in the detector from which track candidates can be made and this results into higher combinatorial background. Oppositely, when multiplicity is small then a collision can be less central, but the significance of the reconstructed signal could be higher because of smaller background. In Figure 4.18 dependence of the mTOF digies (number of digital signals) on the impact parameter $b$ is presented. It can be seen that events with small impact parameters have a larger number of the mTOF digies. It is visible that when cut on the mTOF digies is made at about 100 we can filter out a high percentage of the peripheral events.

In Figure 4.19 you can see the spectrum of the mTOF digies for MC-selected $\Lambda$ (left) and for the case without cuts (right) in geometry 2022_05. Almost all $\Lambda$ have the number of mTOF digies higher than 50 which corresponds with the previous plot ($\Lambda$ are not produced in a peripheral collision).

In Figure 4.20 a mass spectrum in geometry 2022_05 with two mTRD hits and a different number of digies is shown. You can see that signal for events with digies between 40 and 80 is much worse than in the second case where the number of digies is higher than 80. On the other hand, significance decreases which can be caused by reducing statistics. From this point cut on the number of digies is reasonable, nevertheless it has much smaller impact on the reconstruction, thus it will not be used for real data campaign.
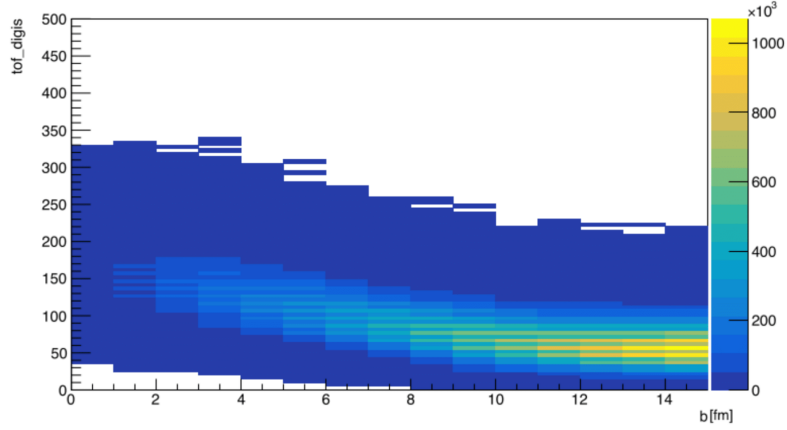
Figure 4.18: Dependence of the mTOF digies on the impact parameter $b$ in the simulations.
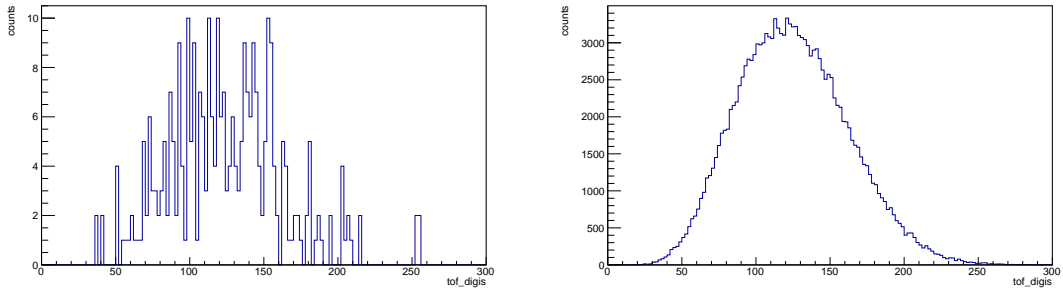


Figure 4.19: Spectrum of the mTOF digies for MC selected $\Lambda$ (left) and for the case without cuts (right) in geometry 2022_05.
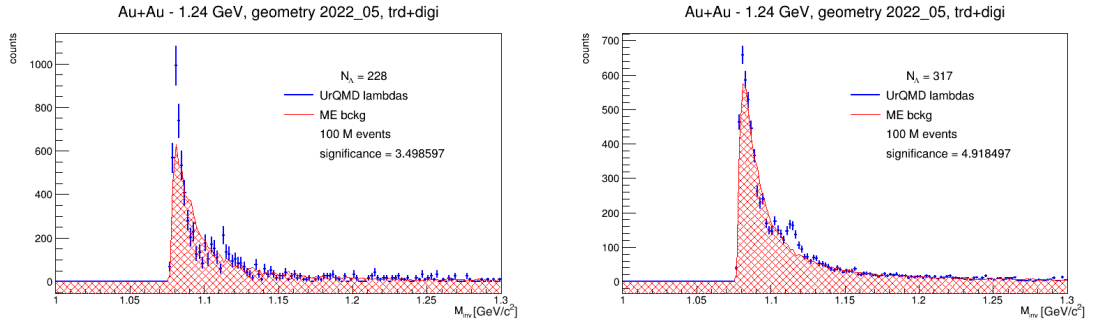


Figure 4.20: Mass spectrum in geometry 2022_05 with two mTRD hits and cut on the number of mTOF digies between $40 - 80$ (left) and higher than 80 (right).

## 4.6.3  TMVA

Toolkit for Multivariate Analysis (TMVA) [58] is ROOT-integrated environment software for the classification of data based on machine learning techniques. TMVA is specifically designed for high-energy physics. TMVA provides several methods for the classification including Rectangular cut optimization, Multi-dimensional likelihood method estimations, Boosted decision trees (used in this thesis) and many others.

Boosted decision trees are a structure based on repeated yes/no decisions. The node starts with a cut on one variable then phase space is split into the regions and the second split occurs. This sequence will be repeated many times and the final result (leaves) will be flagged as signal or background. A sketch of one decision tree is in Figure 4.21. However, this structure is very sensitive to fluctuations and therefore many trees are produced (forest). And then events are classified on a scale from $-1$ to 1 where 1 is the best value corresponding to the signal.
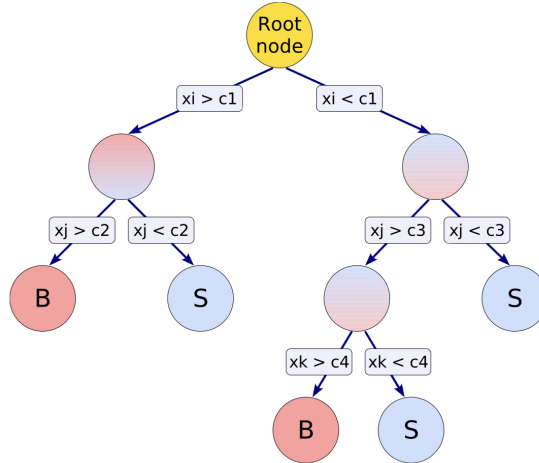


Figure 4.21: Schematic view of the decision tree. From [58].

TMVA was used in the following way. Firstly, the pure signal of reconstructed $\Lambda$ baryons has to be obtained. This was done using matching to MC $\Lambda$ as it was already mentioned before. Events were flagged as coming from $\Lambda$ when MC $\Lambda$ were in acceptance of the detector ($\pm12°$), measured momentum of the $\Lambda$ was similar to MC $\Lambda$ ($|MMom - MMom_{MC}| < 0.5\,\text{GeV/c}$) and momentum of reconstructed pion and MC pion was similar as MC pion ($MPion - MPion_{MC}| < 0.5\,\text{GeV/c}$). Using these cuts one was able to get pure $\Lambda$ signal as shown in Figure 4.22.
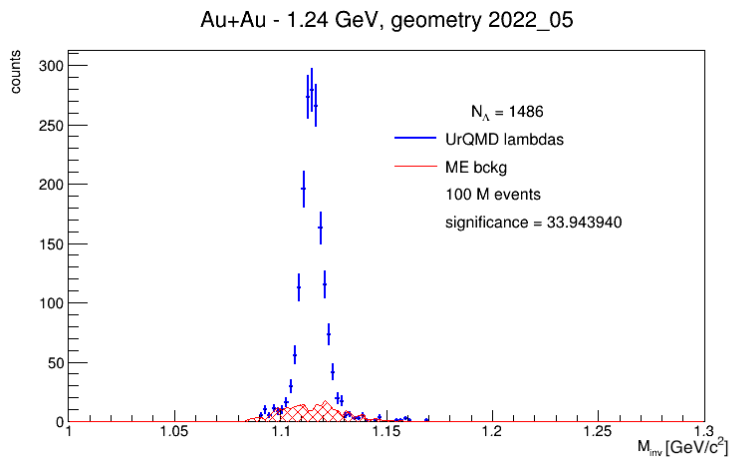


Figure 4.22: Mass spectrum in geometry 2022_05 with MC cuts.

After this signal selection also background selection was made. As a background mixed events (iMixEv $> 1$) were defined and they were filled in `TNtuple` . Both

signal and background events were converted from `TNtuple` to `TTree` and these were inserted into TMVA. In TMVA following variables were selected for optimization: $OpAng$, $DCA$, $PathLen$, $MMom$. It is expected that there should be significant non-trivial correlations among these variable which the BDT should exploit. After the Boosted decisions trees were trained and tested the next step was to classify events and choose classification cut value for getting the best significance of the signal. TMVA trained on one dataset can be also used for evaluation of the other set (for example TMVA trained on geometry 2022_05 can be used for geometry 2022_02). In Figure 4.23 are shown efficiencies for TMVA trained on geometry 2022_05.
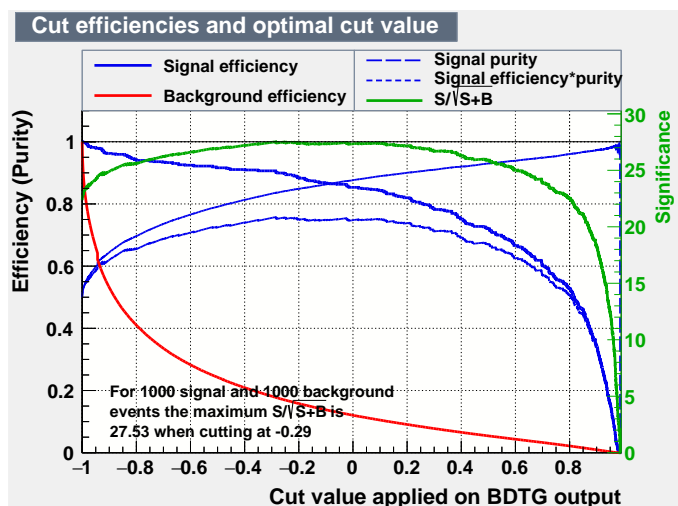


Figure 4.23: Cut efficiency and optimal cut value for 1000 events of signal and 1000 events of background.

With increasing the cut value background efficiency decreases with the largest change in the range of small cut values. It is quite opposite for the signal efficiency which is decreasing slowly at the beginning and this decrease gets steeper for cut values near one. Therefore signal/background ratio has its maximum. These plots suggest putting the cut value to the $-0.29$ for the best signal/background ratio. On the other hand, this is true for 1000 events of background and signal, but in the sample, there is much more background than signal. Therefore several cut values were tested and the best significance was achieved for cut value 0.92. Figure 4.24 presents results for geometry 2022_05 with the TMVA approach. In comparison with Figure 4.14 there is a large increase of the significance from 0.4 to 6.3 and with this value $\Lambda$ are detectable.

The same approach can be used for the same geometry with additional 2 mTRD hits. TMVA was trained on this sample and evaluated. Results are in Figure 4.25, where the significance was high enough even without TMVA (see 4.15) and further increased from 5.1 to 8.2.

Similarly, TMVA was used on geometry 2022_04 with two mTRD hits to improve the results shown in Figure 4.16 (right one). In Figure 4.26 one can see that the significance increases from 6.4 to 7.7.
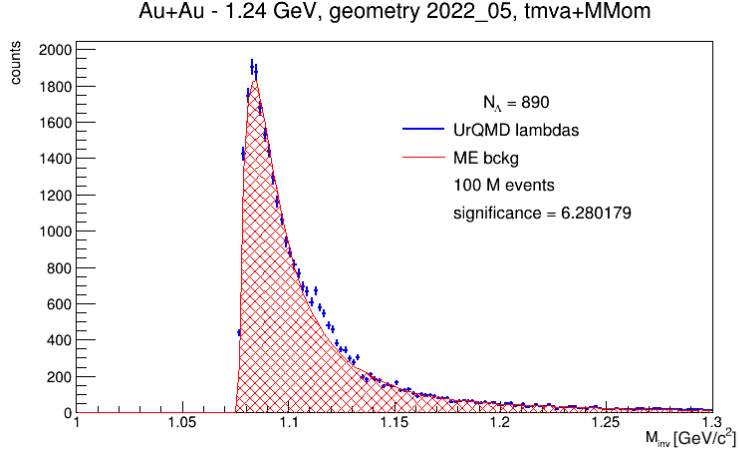
Figure 4.24: Invariant mass distribution for geometry 2022_05 with TMVA trained on the same sample.
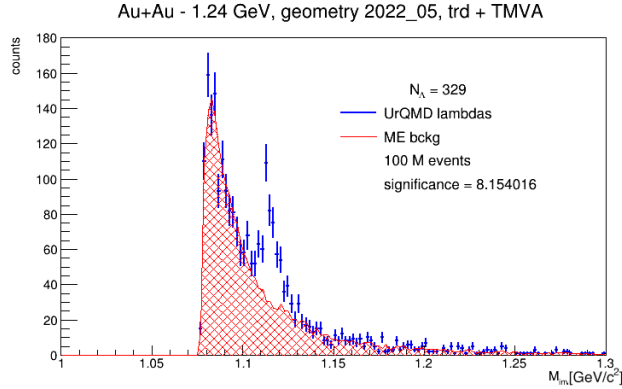


Figure 4.25: Invariant mass distribution for geometry 2022_05 with additional two mTRD hits with TMVA trained on the same sample.

TMVA was also used on geometry 2022_02 but due to small number of events, it was not effective to train BDT on this sample. Therefore TMVA was trained on geometry 2022_04 and events were evaluated on the full geometry. In Figure 4.27 are presented the results. In comparison with Figure 4.17 the significance increased from 2.1 to 2.6 which is still not enough for the detection of $\Lambda$.

## 4.7 Simulations of real geometry

The real geometry used for data taking in 2022 was 2022_05_23_nickel. Results from this geometry can be compared with geometry 2022_04 to evaluate the effects of different mTOF acceptances. In Figure 4.28 one can see results for Ni+Ni collisions at 1.93 AGeV. These results can be compared with Figure 4.12 (bottom left). The decrease in significance is about 50% however this value is still sufficient.

To increase the significance one can use additional mTRD hits for the selection of tracks. In Figure 4.29 are shown the corresponding results. Results for geometry

78
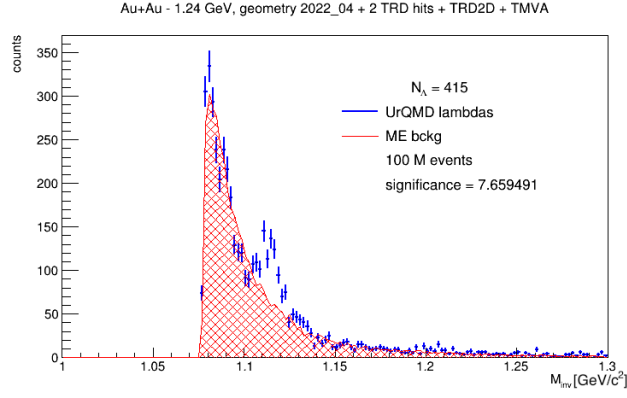
Figure 4.26: Invariant mass distribution for geometry 2022_04 with additional two mTRD hits with TMVA trained on the same sample.
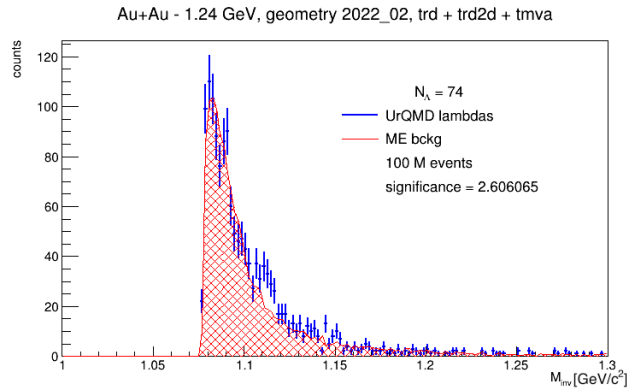


Figure 4.27: Invariant mass distribution for geometry 2022_02 with additional two mTRD hits with TMVA trained on the geometry 2022_04.

2022_04 are located on the left-hand side, these can be also compared with Figure 4.12 (bottom left). Here the significance decreased but the signal-to-background ratio is better. The same effect can be observed when comparing to geometry 2022_05_23_nickel.

The last were simulations of Au+Au collisions in geometry 2022_05_23_nickel. In Figure 4.30 results are shown. This plot can be directly compared with Figure 4.16 (right). It is clear that effect of smaller mTOF acceptance is much larger in comparison with Ni+Ni collisions. The number of reconstructed $\Lambda$ is 30 instead of 492 for geometry 2022_04. This can be caused by higher background and required mTRD hits for proton and pion confirmations. Based on this simulation, the $\Lambda$ production run in Au+Au was extended to reconstruct $\Lambda$ on the order of thousands.
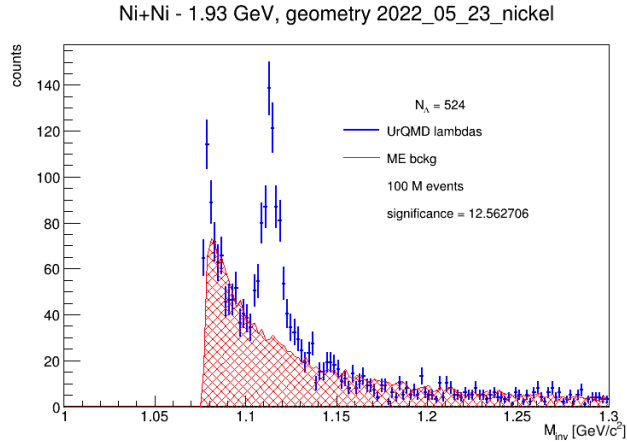
Figure 4.28: Invariant mass distribution for geometry 2022_05_23_nickel.
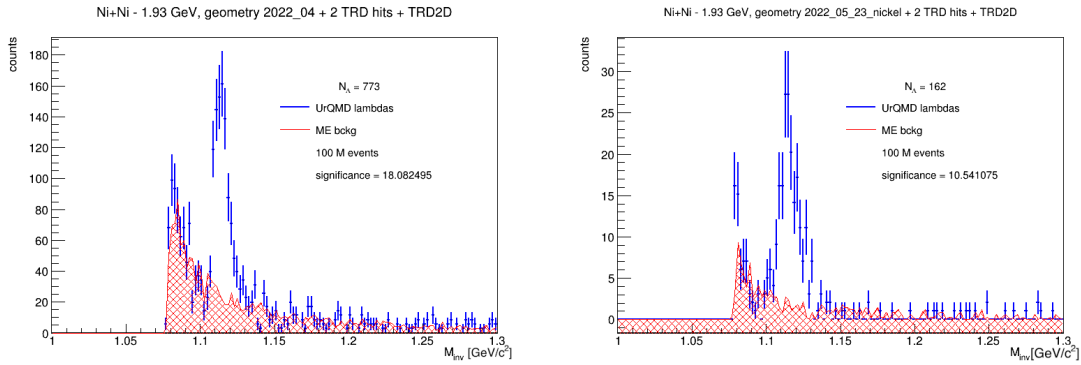


Figure 4.29: Invariant mass distribution for geometry 2022_04 (left) and 2022_05_23_nickel (right) with two mTRD hits.
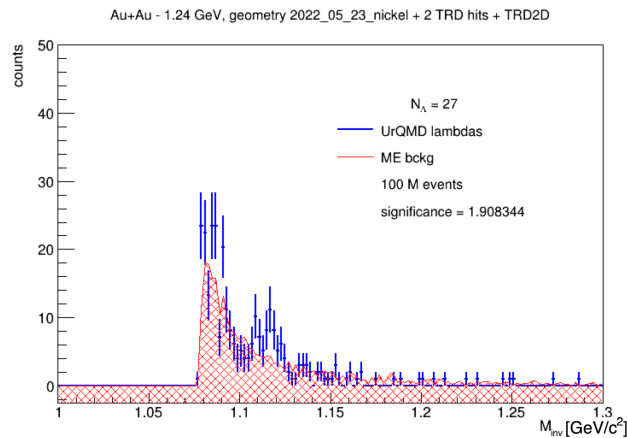


Figure 4.30: Invariant mass distribution for Au+Au collisions at 1.24 AGeV in geometry 2022_05_23_nickel with two additional mTRD hits.

# Chapter 5

# Analysis of the real data

The analysed data were recorded during the data-taking campaign in 2022. The nickel data (Ni+Ni at $1.93\,\mathrm{AGeV}$) were taken in May and the gold data (Au+Au at $1.23\,\mathrm{AGeV}$) in June. The geometry used for data taking was chosen based on simulations (two GEM foils were removed). The beam time was divided into several periods with different purposes. The first period was a production run to collect statistics for $\Lambda$ measurements. After this phase geometry of mCBM was changed and the rest of the beam time was used for detector testing at different collision energies and intensities. The production run data are divided into approximately two-hour-long packages. In my analysis, I used data Ni+Ni data tagged 2391. This data were taken on May 26 between 3:19 and 5:16. The target was $4\,\mathrm{mm}$ thick nickel which corresponds to 10% target. Beam intensity was about $4 - 5 \cdot 10^7$ nickel ions per spill (spill was $10\,\mathrm{s}$ long). That means the average collision rate was $400\,\mathrm{kHz}$. With these conditions about $10^9$ interactions per hour are expected. And in comparison with simulations where $10^8$ minimum bias collision the statistic in run 2391 is expected to be larger by about one order. During the nickel data taking there was a problem with the mTOF gas system, due to this the time resolution is slightly worse. This issue was solved before gold data taking.

## 5.1   Time calibrations

After the data taking work on the alignment and calibrations has started. This is a continuous effort that aims at improving our understanding of the detector and beam conditions. The calibration used for this work was tagged as 2391.4.0000. The time calibrations are based on the idea that almost all particles are produced in primary vertex and their velocity spectrum has to end at the speed of light. In the real data start point for time measurement is the T0 detector. In Figure 5.1 you can see the distribution of velocities assigned to the mTOF hits. The end of the spectra agrees with the speed of light which is approximately at $30\,\mathrm{cm/ns}$. However, this calibration is not final since different mTOF modules have different velocity spectra and therefore the calibrations have to be further improved.
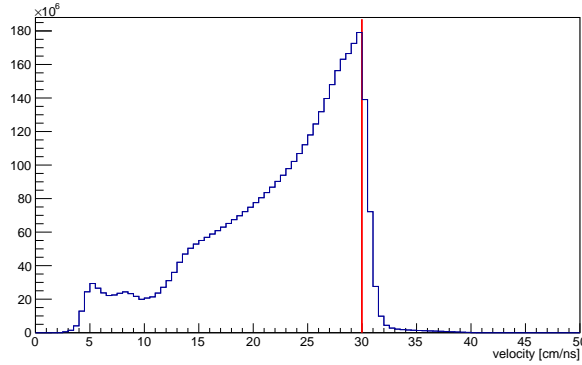
Figure 5.1: Velocity spectrum of the mTOF hits.

## 5.2 Analysis chain

The collected data were stored on the lustre file system in the "tsa" files. Each "tsa" file contains a number of time slices (time slice is time interval containing large number of events). The analysis chain consists of two macros. The first one - `mcbm_unpack_event.C` is used for unpacking "tsa" files and producing so called "digi_event" files. During this stage data from selected detectors are unpacked and events are selected with some trigger condition and then they are built. The second macro is `mcbm_event_reco_L1.C`. In this macro calibrations and alignment are applied and the same hadron analysis as in the case of the simulation is processed. The final result is ROOT tree filled with $\Lambda$ candidates. Events in real data were triggered by "trigger4" conditions which requires: 1 or 2 hits in the T0 detector, a minimum of two hits in the mSTS and a minimum of 8 hits in at least 4 layers of mTOF. After this selection the number of events in the 2391 run is 860M.

## 5.3 Detector performance

Now I would like to focus on the hit distribution in the detector and its comparison with simulations. In Figure 5.2 distributions for two stations of the mSTS are shown. The left part of the second station ($x < -3\,\mathrm{cm}$) is dominated by noise and therefore it has to be removed for further analyses. Also, there is a missing part in the same station for $x > 3\,\mathrm{cm}$ and $y$ between $-3$ and $2\,\mathrm{cm}$ due to module malfunction.

In Figure 5.3 the same distributions for simulations is shown (normalized to the same number of events as in real data). Thus we can compare hits densities per one event between simulations and real data. The hit densities in both mSTS layers are higher compared to the real data.

In Figure 5.4 hit densities in the mTOF in real data (left) and in simulations (right) are shown. In contrast with mSTS, in mTOF the densities of hits are comparable between simulations and real data.

For a more realistic comparison of the real data with simulations, the missing part
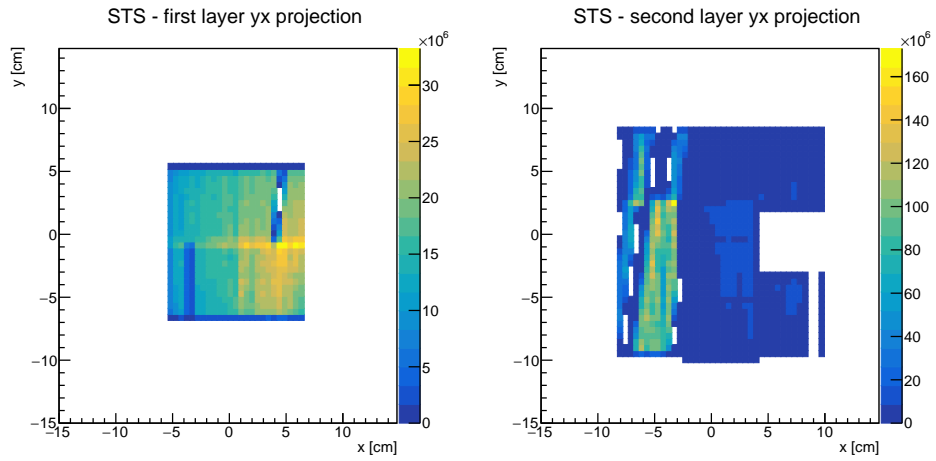
Figure 5.2: mSTS hit distribution for real data.
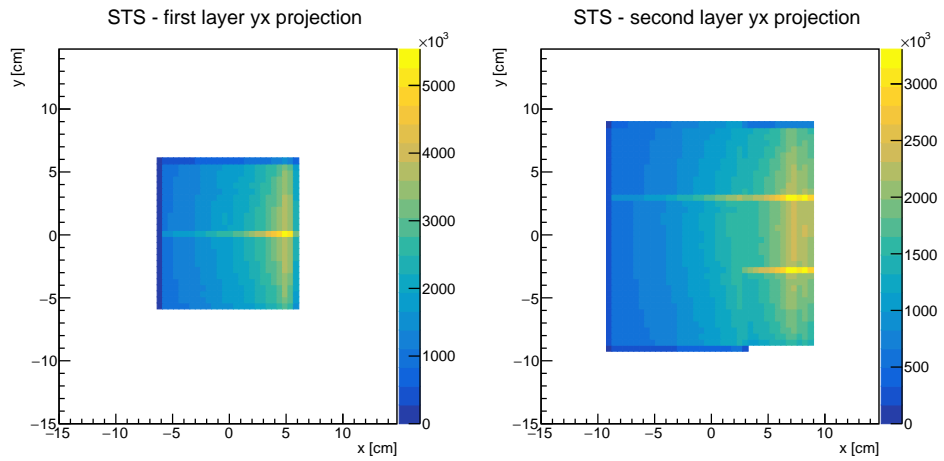


Figure 5.3: mSTS hit distribution for simulations. Normalized to 860M events.

of the mSTS in simulations was also removed.
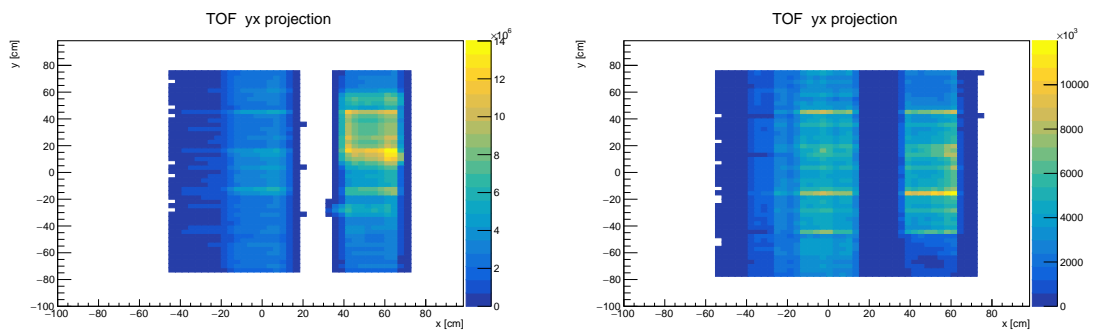


Figure 5.4: mTOF hit distributions for simulations (left) and for real data (right). Normalized to the same number of events.

## 5.4 Λ reconstruction

Λ in real data are reconstructed in the same way as in the simulations. In Figure 5.5 properties of the proton and pion candidates are shown. The variables can be compared with simulations in Figure 4.5. $d_1$ (top left) has the same behaviour in simulation and data. $d_2$ (top right) has maximum shifted to higher values which could be probably caused by misalignment. The biggest difference is in $d_{pion}$ (bottom left), simulations have a maximum at the small values and then it is decreasing. In real data, it is still increasing. $d_{proton}$ (bottom right) compared to simulations is shifted to higher values. Nevertheless, the variables indicate similar behaviour. However, this agreement is achieved with additional requirement on the second mSTS hit. Due to high hit densities in the mSTS, the second mSTS hit was found in the same layer as the first one which caused broken proton and pion candidates. This was solved by requesting a difference larger than 5 cm in the z-direction.
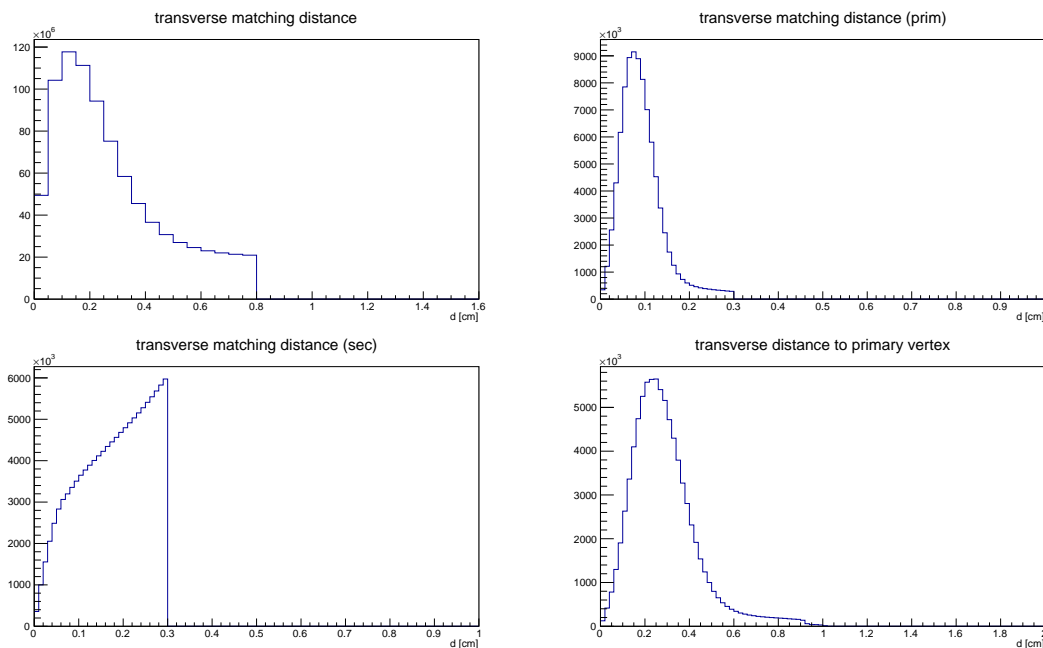


Figure 5.5: Distributions of the $d_1$ (top left), $d_2$ (top right), $d_{pion}$ (bottom left), $d_{proton}$ (bottom right) for Ni+Ni data.

From primary candidates, one can reconstruct the primary vertex as shown in Figure 5.6. The z-position of the primary vertex is in a good agreement with zero however the non-symmetric structure suggests a possible alignment issue.

In Figure 5.7 results for real data with cuts from Table 4.3 can be seen. The beginning of the spectra does not agree with the mixed background. In the Figure, one can additionally see the signal separated from the background and fitted with the Gauss function.

In Figure 5.8 the same spectrum is presented for simulations where the non-working parts were removed (as described above). In comparison with real data, the peak width is about two times smaller and also the background is much smaller.
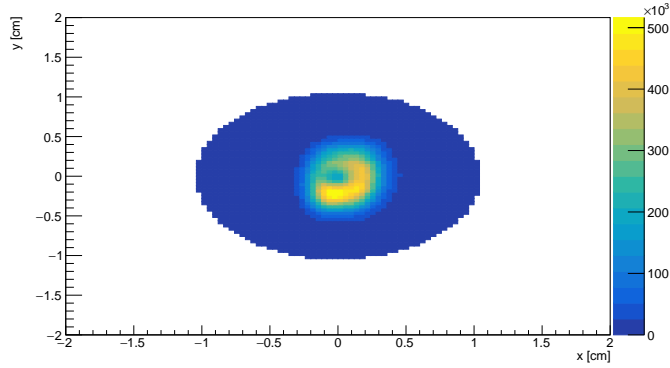
Figure 5.6: position of the reconstructed primary vertex using primary track candidates.
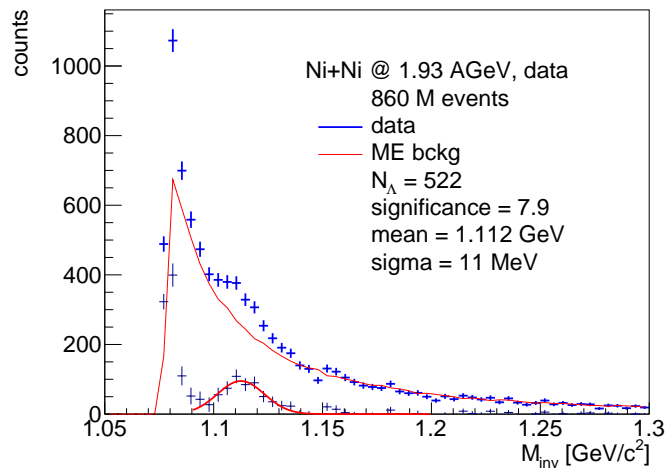


Figure 5.7: Invariant mass distribution of the Λ candidates in real data.

These results can be improved by introducing additional cuts on the pion momentum ($MPion$) and with a more strict cut on the momentum of lambda ($MMom$). Momentum of pion was required to be larger than $0.17\,\mathrm{GeV/c}$ and momentum of lambda larger than $1\,\mathrm{GeV/c}$. Results for real data with these additional cuts are shown in Figure 5.9. The number of reconstructed Λ is comparable with "standard cuts" nevertheless background is more suppressed and the data agree with the mixed events background at the beginning of the spectra. The significance was also enhanced.

For the case when the same cuts are applied to the simulations the final spectra can be seen in Figure 5.10. In this case, almost all background is suppressed.

Another studied variable was the orientation of the Λ decay plane. That means the angle between the proton-pion line in the x-y plane and the vertical axis. Produced Λ are orientated randomly however due to the geometry of the detector and its non-working parts we expected to reconstruct more Λ with the decay plane oriented vertically. In Figure 5.11 one can see the invariant mass spectra for three different angles. Spectra for the decay plane orientated vertically (top left and bottom) show
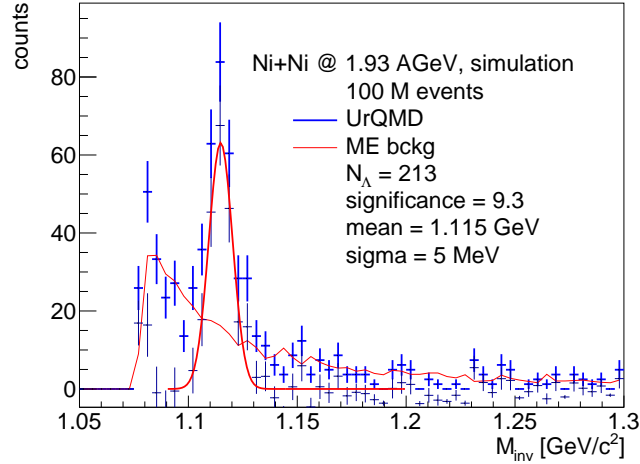
Figure 5.8: Invariant mass of the Λ candidates in simulations in nickel geometry with removed parts of the detector.
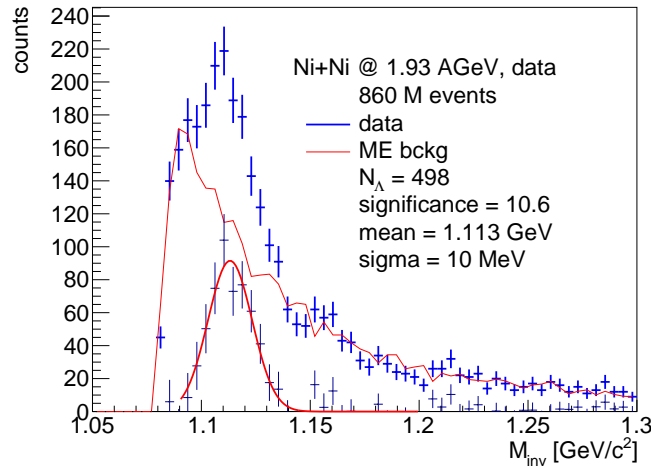


Figure 5.9: Invariant mass distribution of Λ candidates in real data with additional cuts.

a large number of reconstructed Λs and also the description of the background is better.

## 5.5   Comparison with simulations

For the purpose of comparison with simulations, the invariant mass spectrum was divided into three areas. The first area is - under peak (invariant mass between 1.1 and 1.14 $\mathrm{GeV/c^2}$), the second area covers small invariant masses (smaller than 1.1 $\mathrm{GeV/c^2}$) and the third covers large invariant masses (larger than 1.14 $\mathrm{GeV/c^2}$). There are three different data sets compared. Real data are the same as in Figure 5.9, simulations (sim) with the same cuts as real data (Figure 5.10) and simulations (sim2) with larger background (Figure 5.8). All of them are normalized to 100M
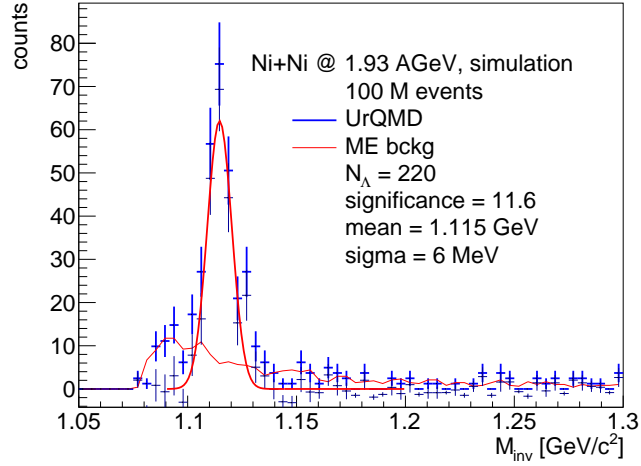
Figure 5.10: Invariant mass distribution of the Λ candidates in simulations with additional cuts.
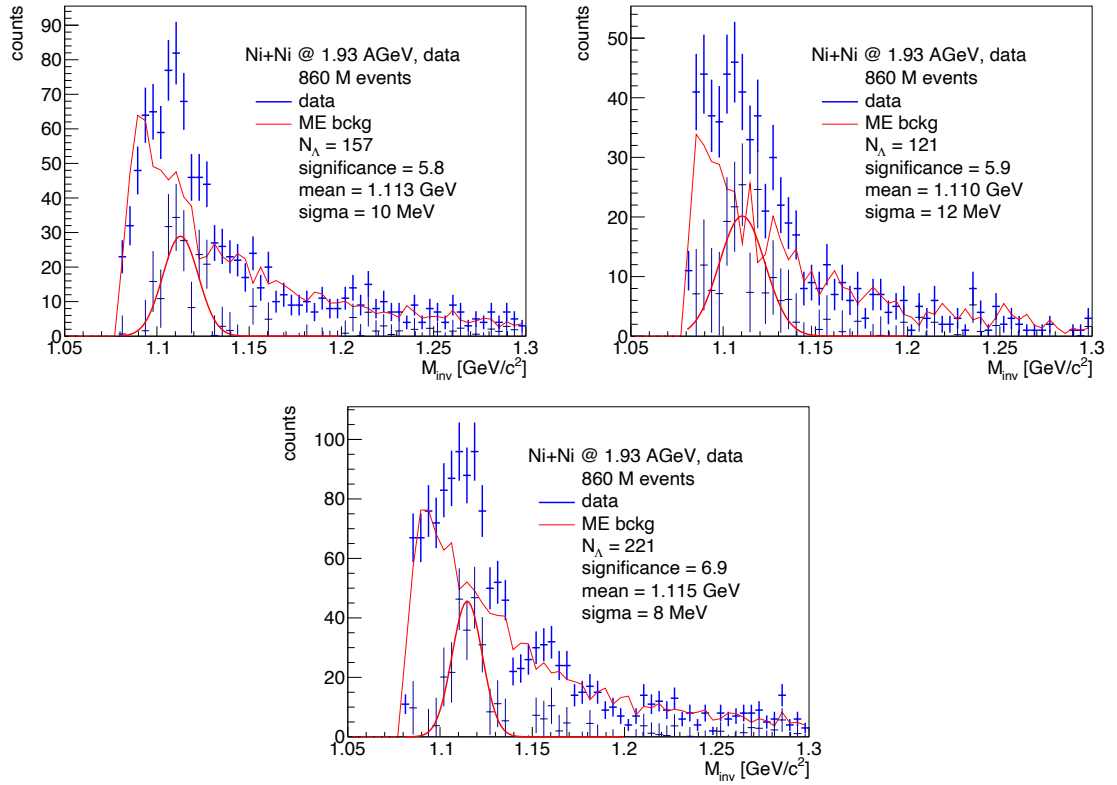


Figure 5.11: Invariant mass distribution of Λ candidates with different decay plane orientation angles. Orientation: left top: $0 - \pi/3$, top right: $\pi/3 - 2\pi/3$, bottom: $2\pi/3 - \pi$.

events however normalization is not important at all, what is important is the shape.

In Figure 5.12 one can see a comparison of the Opening Angle of the Λ candidates. This variable behaves similarly in real data and in simulations.

In Figure 5.13 the same comparison for the momentum of Λ ($MMom$) is shown.
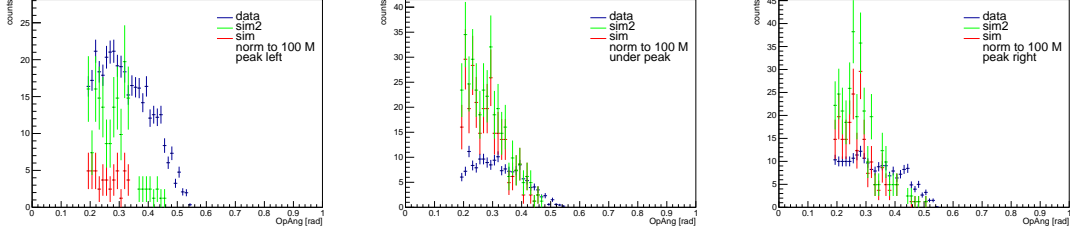
Figure 5.12: Opening Angle ($OpAng$) distribution comparison between three data sets for three region of invariant mass.

There is also good agreement between data and simulations, mainly in the peak region. The peak in the small invariant mass region (top left) of sim2 (simulations with larger background) is caused by a less strict cut on this variable ($MMom > 0.4$ instead of $1\,\text{GeV/c}$).
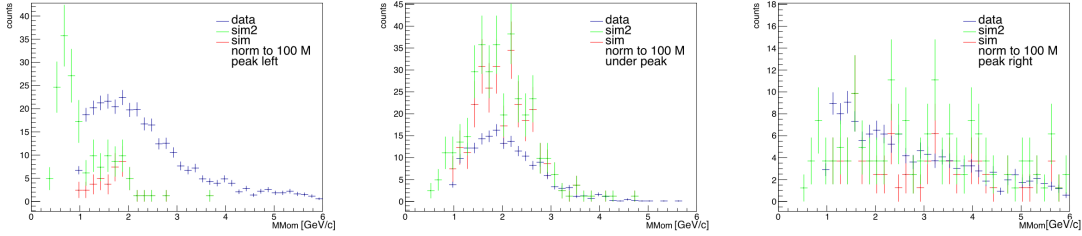


Figure 5.13: Momentum of lambda ($MMom$) distribution comparison between three data sets in the three regions of invariant mass.

In Figure 5.14 a distribution of the $DCA$ of $\Lambda$ candidates is presented. In all three regions, the distribution is flat both in the data and in the simulations. Thus there is an agreement between data and simulations.
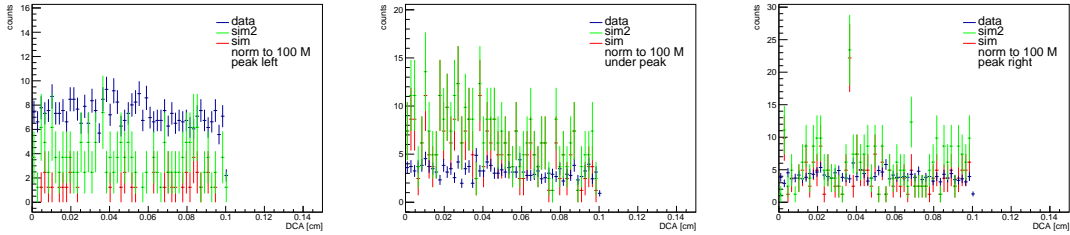


Figure 5.14: Distance of the closest approach ($DCA$) distribution comparison between three data sets for the regions of invariant mass.

The last examined variable is the path (decay) length of the $\Lambda$ ($PathLen$). Obtained results are presented in Figure 5.15. The most important plot is the left one. In the region of low invariant masses, a peak in simulations (with larger background) and in real data can be seen. This peak could be an effect of the target box because in the simulations this distance agrees with the distance between the target box and target itself. However, this distance is shifted about $2\,\text{cm}$ in real data which could be an additional effect of the non-perfect alignment.
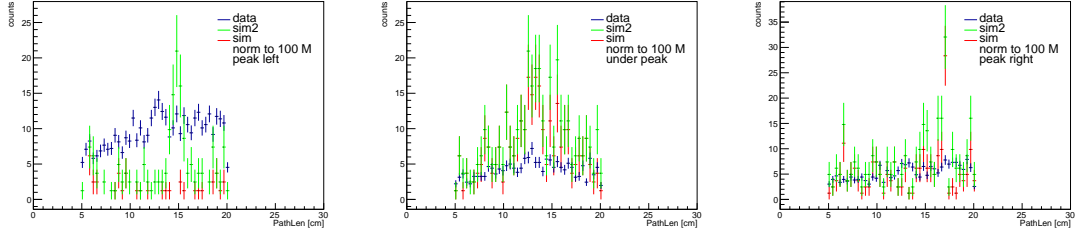
Figure 5.15: Path length (PathLen) distribution comparison between three data sets for the three regions of invariant mass.

## 5.6 mTRD hits

Similarly as in the simulation also in the real data I tried to use mTRD information for selection of the proton and pion candidates. In the simulations, the best value for distance between mTRD hit and track candidate was 0.4 cm for at least two hits. However it was found that this does not work in real data. This distance has to be actually increased to 2 cm and the number of mTRD hits changed. Results for this selection criteria are shown in Figure 5.16. The most plausible explanation for the difference between data and simulations is a possible misalignment.
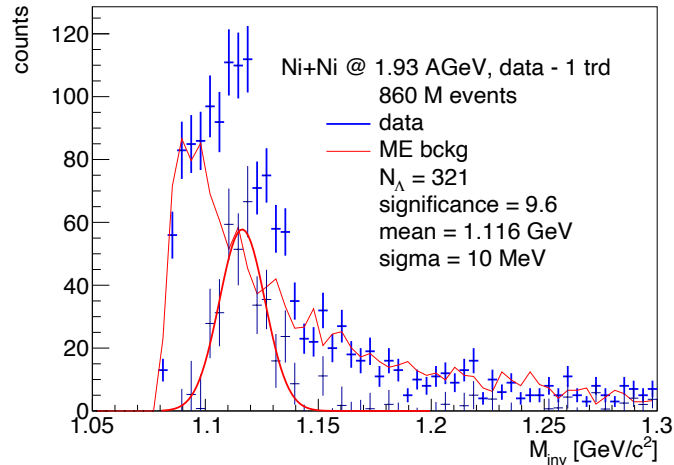


Figure 5.16: Invariant mass spectrum of $\Lambda$ candidates when using mTRD hits.

## 5.7 TMVA

TMVA was also used for the improvement of the real data results. However, the Boosted decision trees have to be trained on the simulation and then used for real data analysis. This means that one relays on the correctness of the simulations. Additionally, the Momentum of Pion has to be included as input variable (the effect of the cut on this variable you can see above). It is caused by larger background at the beginning of the mass spectra and with a cut on the Momentum of Pion it can be suppressed.

Boosted decision trees were trained on the simulation in nickel geometry with variables $OpAng$, $PathLe$n, $DCA$, $MMom$ and $MPion$. Trained trees were used for validation of the events from simulation and also real data analysis. In Figure 5.17 results for simulations are presented. The BDT have a similar effect as advanced cuts (Figure 5.10).
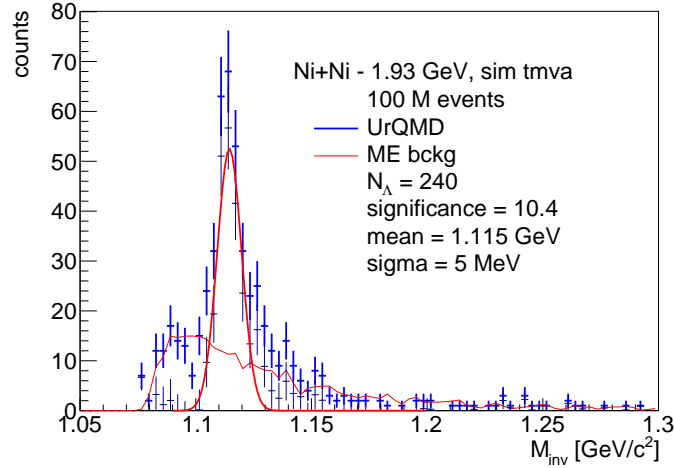


Figure 5.17: Invariant mass spectrum for $\Lambda$ candidates using BDT instead of standard cuts (simulation).

In Figure 5.18 results for invariant mass spectrum using TMVA are shown. Results are very similar to the ones with advanced cuts (Figure 5.9) however the signal/background ratio is slightly better.
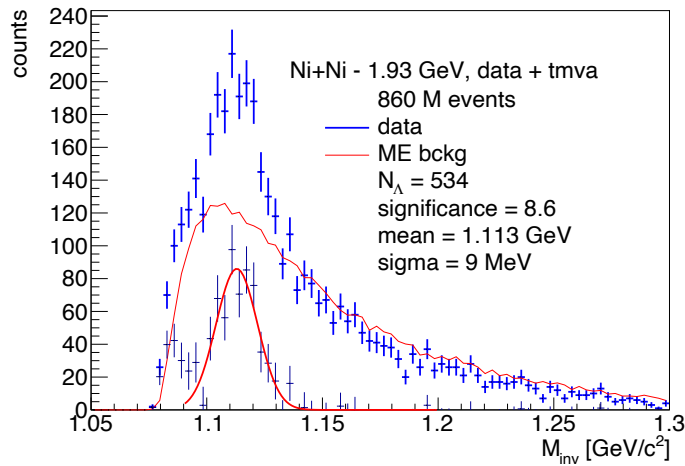


Figure 5.18: Invariant mass spectrum for $\Lambda$ candidates using BDT instead of standard cuts (real data).

# Summary

The presented thesis is focused on the CBM experiment with emphasis on its precursor, the mini-CBM experiment. One of the main goals was to get acquainted with the physics of the CBM as well as with its software and hardware. The physics of the CBM is described in the first two chapters and the experiment in the third chapter.

Before the CBM itself will be built, mCBM takes its place as a demonstrator experiment. The aim of mCBM is to test detectors and software functionality in the most realistic environment possible. One of the indicators which unambiguously demonstrates that all systems are working all the way from detector signal readout to real data reconstruction is the detection of the $\Lambda$ hyperon. The goal of my own work in this thesis was to optimize mCBM setup so that the experiment would be able to reconstruct $\Lambda$ hyperons from the short data-taking campaign of 2022 and later work on the obtained real data.

Multiple possible geometries of the mCBM were tested in simulations in order to select the one which would be later used for data-taking. In the beginning, pure $\Lambda$ sample was used and thanks to these simulations initial estimates for cuts on $\Lambda$ candidates were obtained. The next step were simulations of O+Ni at beam energy of $2\,\mathrm{AGeV}$. This system contains only small background and the energy of the collisions is higher than the threshold of $\Lambda$ production. I was able to manually tune the cuts and show that for these collisions it will be possible to reconstruct $\Lambda$ in all considered mCBM setups.

Another collision system was Ni+Ni at $1.93\,\mathrm{AGeV}$. The amount of background is higher when compared to O+Ni collisions and the energy of the collision is only slightly above the threshold. Nevertheless, the signal is still sufficient and no additional substantial improvements in methodology are needed for the extraction of the $\Lambda$ signal in all of the setups. When comparing different geometries we can see a clear effect of the additional material budged on the obtained significance of the $\Lambda$ signal.

The last simulated collision system was Au+Au at $1.24\,\mathrm{AGeV}$. This collision system has the lowest energy (below threshold) and the highest combinatorial background. Hence the detection of $\Lambda$ is very challenging. By using the same methods as in previous systems $\Lambda$ are not detectable. Nevertheless, additional mTRD hits used as intermediate track points can be very useful. With the mTRD information $\Lambda$ can be detected in geometries without GEM foils. The last way how to improve the significance of the reconstructed signal was by using techniques of machine learning.

The method of boosted decision trees was successfully employed. With this approach we can observe signal with high enough significance, but only in setups without GEM foils which add too much material.

Based on these results the optimal setup for Au+Au collisions was selected for data taking. The data-taking campaign took place in June 2022 and I was part of the on-site expert crew.

The last chapter of the thesis is dedicated to real data analysis of Ni+Ni data taken at beam energy of $1.93\,\text{AGeV}$ in 2022 and its comparison with simulations. Time calibration and detector performance are discussed. It was found that part of the second layer of the mSTS module is missing and a problem with noise was identified. The $\Lambda$ properties in simulations were found to be in a reasonably good agreement with real data. This allowed to use the machine learning techniques trained on simulations to enhance the significance in the real data. This, in turn, will allow in future to extract reconstruction efficiencies and obtain physics results on $\Lambda$ production at mCBM.

Results presented in this thesis show that mCBM is operational and the obtained $\Lambda$ signal has been presented to the FAIR community as one of the milestones towards building full CBM experiment. The intermediate results of this thesis were presented as a poster at FAIRness 2022 conference and proceedings from this conference were published in the Proceedings of Science.

# Bibliography

[1] R. Vogt. *Ultrarelativistic heavy-ion collisions*. Elsevier, Amsterdam, 2007.

[2] C. Wong. *Introduction to high-energy heavy-ion collisions*. World Scientific Publishing, Singapore, Singapore, December 1990.

[3] M. Thomson. *Modern Particle Physics*. Cambridge University Press, 2013.

[4] K. Johnson. The M.I.T. Bag Model. *Acta Phys. Polon. B*, 6:865, 1975.

[5] Wikipedia contributors. Physics_beyond_the_standard_model — wikipedia, the free encyclopedia, 2017. [Online; accessed 3 -May -2022].

[6] S. Giorgini. *Lecture Notes on Statistical Mechanics - Course for the Master degree in Physics at the University of Trento from 2010 to 2015 (misprints amended and solution to problems added)*. 01 2016.

[7] O. Denisovskaya and et al.. Dense cold nuclear matter study with cumulative trigger. proposal, 11 2009.

[8] M. Bluhm, P. Alba, W. Alberico, A. Beraudo, and C. Ratti. Lattice qcd-based equations of state at vanishing net-baryon density. *Nuclear Physics A*, 929:157–168, 2014.

[9] A. Pandav, D. Mallick, and B. Mohanty. Search for the QCD critical point in high energy nuclear collisions. *Progress in Particle and Nuclear Physics*, 125:103960, jul 2022.

[10] V. Pospíšil. Experimentální studium relativistických jádro-jaderných srážek s pomocí di-leptonového spektrometru HADES. Diplomová práce, České Vysoké Učení Technické Fakulta Jaderná a Fyzikálně Inženýrská, Praha, 2005.

[11] B. Betz. Jet propagation and mach-cone formation in (3+1)-dimensional ideal hydrodynamics, 2009.

[12] F. Seck. Thermal dileptons as fireball probes at SIS energies. *Talk at Critical Point and Onset of Deconfinement 2016 in Wroclaw*.

[13] F. Noferini. ALICE Highlights. *MDPI Proc.*, 13(1):6, 2019.

[14] A. Morreale. Production of $\pi 0$ , $k^{\pm}$ and $\nu$ mesons in pb-pb and pp collisions at $= 2.76$ tev measured with the alice detector at the lhc. *Journal of Physics: Conference Series*, 779:012051, 01 2017.

[15] L. Adamczyk and et al. Bulk properties of the medium produced in relativistic heavy-ion collisions from the beam energy scan program. *Phys. Rev. C*, 96:044904, Oct 2017.

[16] S. A. Voloshin, A. M. Poskanzer, and R. Snellings. Collective phenomena in non-central nuclear collisions. 2008.

[17] M.S. Abdallah and et al. Disappearance of partonic collectivity in snn=3gev au+au collisions at rhic. *Physics Letters B*, 827:137003, 2022.

[18] C. Blume and C. Markert. Strange hadron production in heavy ion collisions from sps to rhic. *Progress in Particle and Nuclear Physics*, 66(4):834–879, 2011.

[19] ALICE Collaboration. Direct photon production in Pb–Pb collisions at sNN=2.76 TeV. *Physics Letters B*, 754:235–248, 2016.

[20] Hades Collaboration. Probing dense baryon-rich matter with virtual photons. *Nature Physics*, 15(10):1040–1045, July 2019.

[21] CMS Collaboration. Suppression of $\Upsilon(1S)$, $\Upsilon(2S)$, and $\Upsilon(3S)$ quarkonium states in PbPb collisions at sNN=2.76TeV. *Physics Letters B*, 770:357–379, 2017.

[22] S. Acharya and et al. $d$-meson azimuthal anisotropy in midcentral pb-pb collisions at $\sqrt{s}_{nn} = 5.02$ TeV. *Phys. Rev. Lett.*, 120:102301, Mar 2018.

[23] V. Friese. Strangeness from sps to fair: Searching for the onset of deconfinement. *EPJ Web Conf.*, 164:06004, 2017.

[24] P. Koch, B. Müller, and J. Rafelski. Strangeness in relativistic heavy ion collisions. *Physics Reports*, 142(4):167–262, 1986.

[25] J. Rafelski and B. Müller. Strangeness production in the quark-gluon plasma. *Phys. Rev. Lett.*, 48:1066–1069, Apr 1982.

[26] P. Koch, B. Müller, and J. Rafelski. From Strangeness Enhancement to Quark–Gluon Plasma Discovery. *Int. J. Mod. Phys. A*, 32(31):1730024, 2017.

[27] J. Rafelski. Melting hadrons, boiling quarks. *The European Physical Journal A*, 51(9), 2015.

[28] J. Adam and et al. Enhanced production of multi-strange hadrons in high-multiplicity proton-proton collisions. *Nature Phys.*, 13:535–539, 2017.

[29] P. Braun-Munzinger, K. Redlich, and J. Stachel. Particle production in heavy ion collisions. *Quark–Gluon Plasma 3*, 2004-01-21.

[30] J. Song. Production of hadronic resonances measured with ALICE at the LHC. *J. Phys. Conf. Ser.*, 1602(1):012008, 2020.

[31] J. Cleymans, H. Oeschler, and K. Redlich. Influence of impact parameter on thermal description of relativistic heavy ion collisions at $(1 - 2)a$GeV. *Phys. Rev. C*, 59:1663–1673, Mar 1999.

[32] J. Cleymans. Status of the thermal model and chemical freeze-out. *EPJ Web of Conferences*, 95, 12 2014.

[33] M. Bleicher and E. Bratkovskaya. Modelling relativistic heavy-ion collisions with dynamical transport approaches. *Progress in Particle and Nuclear Physics*, 122:103920, 2022.

[34] S Bass and et al. Microscopic models for ultrarelativistic heavy ion collisions. *Progress in Particle and Nuclear Physics*, 41:255–369, 1998.

[35] C. Alt and et. al. Energy dependence of $\phi$ meson production in central Pb + Pb collisions at $\sqrt{s_{NN}} = 6$ to 17 gev. *Phys. Rev. C*, 78:044907, Oct 2008.

[36] P.A. Zyla and et al. Review of Particle Physics. *PTEP*, 2020(8):083C01, 2020.

[37] D.B. Kaplan and A.E. Nelson. Strange goings on in dense nucleonic matter. *Physics Letters B*, 175(1):57–63, 1986.

[38] L. Chlad. Study of transverse flow of kaons in au+au collisions at 1.23agev. Doctoral thesis, Faculty of mathematic and physics Charles University, Praha, 2021.

[39] R. Abou Yassine and et al. Measurement of global polarization of lambda hyperons in few-gev heavy-ion collisions. *Physics Letters B*, 835:137506, 2022.

[40] P. Senger. Particle production in heavy-ion collisions. *Progress in Particle and Nuclear Physics*, 53(1):1–23, 2004. Heavy Ion Reaction from Nuclear to Quark Matter.

[41] Y.J. Huang and et al. Merger and postmerger of binary neutron stars with a quark-hadron crossover equation of state. *Physical Review Letters*, 129(18):1859–1896, 2022.

[42] J. Adamczewski-Musch and et al. Probing dense baryon-rich matter with virtual photons. *Nature Physics*, 15(10):1040–1045, 2019.

[43] O. Brüning and S. Myers. *Challenges And Goals For Accelerators In The XXI Century*. World Scientific Publishing Company, 2016.

[44] A. Smolyakov, W. Fischer, C. Omet, and Peter Spiller. Comparison of the present and planned operation of the sis18 and the ags booster with intermediate charge state heavy ions. 01 2005.

[45] P. Spiller and et al. The fair heavy ion synchrotron sis100. *Journal of Instrumentation*, 15:T12013–T12013, 12 2020.

[46] V. Friese. Cbm physics at the sis-100. *Verhandlungen der Deutschen Physikalischen Gesellschaft*, (Maiz2012issue):1, 2012. Nuclear physic and radiation physics.

[47] B. Friman and et al. *The CBM Physics Book: Compressed Baryonic Matter in Laboratory Experiments*, volume 814. 01 2011.

[48] J. Heuser, W. Müller, V. Pugatch, P Senger, Ch. Schmidt, Ch. Sturm, and U. Frankenfeld, editors. *[GSI Report 2013-4] Technical Design Report for the CBM Silicon Tracking System (STS)*. GSI, Darmstadt, 2013.

[49] T. Balog. Overview of the cbm detector system. *Journal of Physics: Conference Series*, 503:012019, 04 2014.

[50] CBM Progress Report 2019. Technical Report CBM-PR-2019, Darmstadt, 2020.

[51] C. Grupen and B. Shwartz. Particle detectors, second edition. *Particle Detectors, Second Edition*, pages 1–651, 01 2008.

[52] V. Friese and Ch. Sturm, editors. *CBM Progress Report 2012*. GSI, Darmstadt, 2013.

[53] P. Senger and V. Friese. Cbm progress report 2021. Technical report, 2022.

[54] S. Tavernier. *Experimental Techniques in Nuclear and Particle Physics*. Springer, Berlin, Germany, 2010.

[55] CBM Collaboration. mCBM@SIS18. Technical report, Darmstadt, 2017.

[56] R. Brun, F. Bruyant, M. Maire, A. C. McPherson, and P. Zanarini. Geant3. 9 1987.

[57] R. Brun and R. Rademakers. Root — an object oriented data analysis framework. *Nuclear Instruments and Methods in Physics Research Section A: Accelerators, Spectrometers, Detectors and Associated Equipment*, 389(1):81–86, 1997. New Computing Techniques in Physics Research V.

[58] J. Therhaag. TMVA Toolkit for multivariate data analysis in ROOT. *PoS*, ICHEP2010:510, 2010.

# Appendix A

# Publication

# Performance studies for the mCBM experiment campaigns in 2022

**Radim Dvořák**[1,*] **and Lukáš Chlad**[1,2] **for the CBM collaboration**

[1]*Czech technical university in Prague,*
*Jugoslávských partyzánů 1580/3, Prague, Czech republic*

[2]*Ústav jaderné fyziky AV ČR, v. v. i.*
*Husinec - Řež, čp. 130, 250 68 Řež*

*E-mail:* dvorar10@fjfi.cvut.cz

With mCBM@SIS18 (short "mCBM") a CBM precursor and demonstrator experiment has been constructed in 2017/18 at the SIS18 facility of GSI/FAIR, taking data within the FAIR phase-0 program since 2019. The primary aim of mCBM is to commission and optimise the CBM triggerless-streaming data acquisition system including data transport to a high performance computer farm, the online track and event reconstruction and event selection algorithms and the online data analysis as well as the controls software packages. mCBM comprises of prototypes and pre-series components of all CBM detector subsystems and their read-out systems. The reconstruction of $\Lambda^0$ hyperons will be used as a benchmark observable probing the performance of the CBM hard- and software. Using simulations, various detector configurations have been tested identifying the most suitable geometry for reconstruction of $\Lambda^0$ hyperons with the mCBM setup in real data.

*FAIR next generation scientists - 7th Edition Workshop (FAIRness2022)*
*23-27 May 2022*
*Paralia (Pieria, Greece)*

# 1. Introduction

$\Lambda^0$ hyperons are detected in mCBM via their decay into proton and pion. Due to the lack of the magnetic field and particle identification $\Lambda^0$s are detected only trough topological cuts on straight tracks under mass assumptions.

Fig. 1, left side sketches one of the mCBM detector configurations evaluated for data taking in 2022, tagged 2022_02. The setup consists of prototypes or pre-series modules of all CBM detector subsystems: Silicon Tracking System (mSTS), Muon Chamber (GEM chamber module), Transition Radiation Detector (TRD1D and TRD2D), Time-of-Flight detector (mTOF). Other configurations with different setups and hence material budgets are tested as well, namely 2022_04 - without two GEM layers, 2022_03 without one GEM layer, 2022_05 without two GEM layers and without TRD2D (two sided prototype).

A simple track finding algorithm is applied based on combining hits in mSTS and mTOF with the additional possibility of adding TRD hits. The scheme of the processing flow is shown in Fig. 1, right side. The algorithm starts with hits in mTOF and construction of Vertex-mTOF lines. Afterwards mSTS layers are scanned for hits (upper branch of the flow diagram). If two hits are found within 3mm from the line a track from the two hits is formed. This track is taken as primary if it's distance from primary vertex (VDCA) is more then 5mm. Since most of the $\Lambda^0$ momentum is carried off by the proton these tracks are considered as proton candidates. mSTS hits which are not assigned to proton candidates are used for finding secondary pion candidates. mTOF-mSTS lines are constructed and mSTS is scanned for the second mSTS hit within 3mm. If a hit is found accordingly a pion candidate is created. Both pion and proton candidate tracks can be further approved or rejected by additional matching of TRD hits. The momentum is obtained by measuring velocity via time of flight in mTOF and the assumption that proton and pion candidates have corresponding masses. Hence, a $\Lambda^0$ candidate is created in case a pair of pion and proton candidates have their DCA, opening angle (OpAng) and $\Lambda^0$ decay position (PathLen) within certain cut ranges which were optimized in this study.
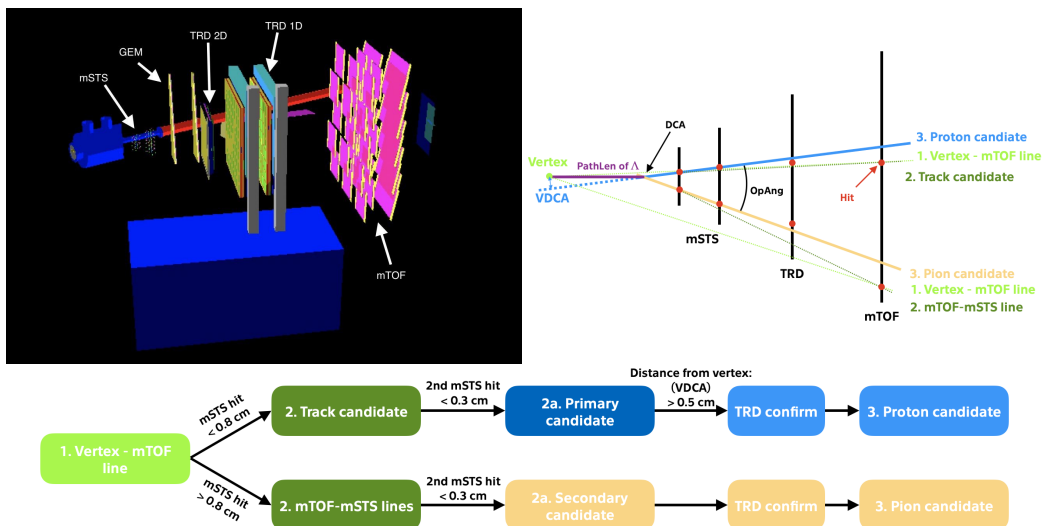


**Figure 1:** Sketch of the full mCBM geometry 2022_02 (left), $\Lambda^0$ finding algorithm (right) and flow diagram of the track finding algorithm (bottom).

## 2. Results

Nucleus-nucleus collisions were simulated with UrQMD, sampling 100M minimum bias events. Result for Ni+Ni collisions at kinetic beam energy of 1.93 AGeV are shown in Fig. 2. The combinatorial background was obtained using mixed-event technique. As can be seen, even in full (2022_02) geometry $\Lambda^0$s are reconstructed with sufficient significance and additional TRD hits are not mandatory. Also, the clear effect of additional material on reconstruction yield is observable. As shown in Fig. 2, the two MUCH stations (GEMs, geometry 03 and 04) reduce the yield significantly while the TRD2D station has only a moderate influence.
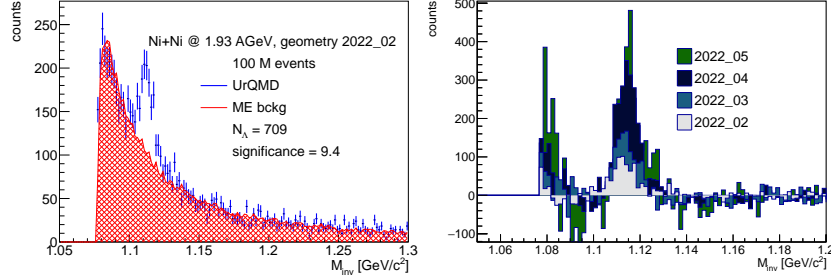


**Figure 2:** Results for Ni+Ni at 1.93 AGeV in geometry 2022_02 (left) and comparison for different geometries (right).

In Au+Au collisions at 1.24AGeV $\Lambda^0$ can not be identified without requirement of additional TRD hits matched to the tracks due to the increased track multiplicity as well as the strongly reduced production probability. In full mCBM geometry (2022_02), the signal is not detectable even when two TRD hits are used, see Fig. 3, most left panel. In setups with smaller material budget, such as 2022_05, the signal can be seen (Fig. 3 middle panel). Moreover, the obtained significance can be further improved when using machine-learning techniques instead of standard cuts, as shown in Fig. 3 right. Specifically boosted decision trees were used with a mixed-event generated background. ML was tested in all geometries however in geometries with higher material budget than 2022_04 the significance is not sufficient to guarantee good statistic of reconstructed $\Lambda^0$ at mCBM run 2022.
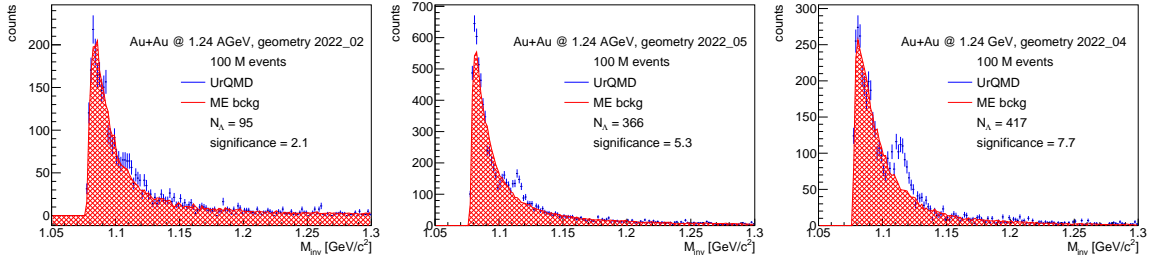


**Figure 3:** Results for Au+Au collisions at 1.24 AGeV with tracks requiring matching of two TRD hits for three different mCBM geometries with standard cuts and after using machine-learning optimization (right).

## 3. Conclusions

Simulations of $\Lambda^0$ hyperon reconstruction were performed for multiple setups of mCBM detector and collision systems. Significant effects of material budget and particle multiplicity were observed. Efficiency improvements are gained when using intermediate points from TRD detector and optimisation via machine-learning. We are hence expecting to observe a significant $\Lambda^0$ signal in the Ni+Ni and Au+Au runs taken in 2022.